Design, Development and Operation of Novel Ion Trap Geometries

PhD Thesis

by

José Rafael Castrejón Pita

Supervisor: Prof. R.C. Thompson

The Blackett Laboratory, Imperial College

Thesis submitted in partial fulfilment of the requirements for
the degree of Doctor in Philosophy of the University of London
and for the Diploma of Imperial College.

March 2007

I, José Rafael Castrejón Pita, confirm that the work presented in this thesis is my own. Where information has been derived from other sources, I confirm that this has been indicated in the thesis.

José Rafael Castrejón Pita

Abstract

This thesis presents novel designs of ion traps for different applications. The first part introduces the topic of ion traps to clarify the local context of this work. In the second part, the proposal of a novel design for a Penning ion trap is presented. It is shown that this trap, called the wire trap, has many advantages over traditional designs due to its open geometry and scalability[1]. In the third part of this work, the development of two scalable RF wire traps is presented. Both designs are based on the geometry of the wire Penning trap and they share the open geometry and the scalability. In the fourth part, the design, computer simulation, construction and testing of a wire trap prototype is presented. This section ends with an explanation of the future experiments that will be carried out with such a prototype. In the fifth section, another novel design for a planar Penning trap is presented and discussed in the text. This design, called the two plate trap, shares many advantages of the wire traps, including the scalability[2]. The sixth section of this work deals with the design of a cylindrical Penning trap for the storage of highly charged ions[3]. Finally, in the last section, a summary of the original contributions of this work is presented.

These studies were supported by CONACyT, SEP and the ORS Awards Scheme.

---

[1] published article: *Physical Review A*, **72** 013405 (2005).

[2] published article: *Journal of Modern Optics*, **in press** (2006).

[3] published article: *Nuclear Instrument and Methods in Physics Research B*, **235** 201 (2005).

Contents

List of Figures

List of Tables

1 Introduction

Ion traps are remarkable devices because they create conditions where charged particles can be stored in an isolated environment. They have been widely used since their discovery in the middle of the last century, [1]. As a consequence, high precision measurements in many fields of physics have been developed using ion traps as their main component. Typical applications of ion traps include studies on high accuracy clocks [2], quantum chaos [3], spectroscopy [4] and lifetime studies. These studies are possible because the high quality environment created by ion traps allows studies with even a single ion for long periods of time.

The basic principles of ion traps are very simple; the motion of a charged particle is confined by electric and magnetic fields. Ion traps cannot be constructed just with purely electrostatic fields because an electrostatic field with minima in three dimensions cannot be constructed; this is easily proved using Maxwell's equations. Therefore, the trapping conditions of ion traps result from a mix of electric and magnetic fields or by the combination of static and dynamic electric fields. Ion traps that use magnetostatic and electrostatic fields are commonly called Penning traps. On the other hand, ion traps that run with static and dynamic electric fields are usually called Paul or radio frequency (RF) traps. Traditionally, both traps have a three-electrode setup consisting of a ring electrode and two end-cap electrodes; the shape of these electrodes is shown on Fig 1.1.

This particular shape was chosen because it is able to produce precise quadratic potentials radially and axially. A good quadratic potential implies high-precision harmonic motion of ions and thus well defined frequencies. Penning and Paul traps use an electrostatic potential across the ring-endcap arrangement in order to confine ions axially, but they differ in the way the radial confinement is produced. The Penning trap utilizes a magnetic field along the z direction to produce the final confinement. On the other hand, in Paul traps a RF voltage is applied between the endcaps and the ring electrode [5]. This RF component, combined with the electrostatic potential, produces axial and radial trapping conditions in the Paul trap and consequently Paul

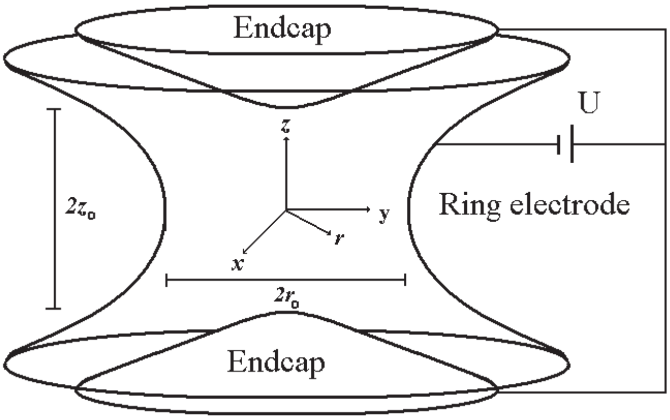

Figure 1.1: Three-electrode configuration in Penning and Paul traps

traps are also called RF traps. Penning and Paul traps are explained in detail in the next subsections.

1.1 Penning traps

Nowadays, all ion traps with an axial magnetic field are called Penning traps [5]. As mentioned before, in these traps, the magnetic field provides the radial confinement while an electrostatic field produces the axial trapping potential. Often, Penning traps have a configuration like the one shown in Fig. 1.1. In order to achieve trapping conditions, the ring is kept at a potential U_0 with respect to the endcap electrodes producing an electrostatic potential of the form:

$$\phi(r,z) = \frac{U_0}{{R_0}^2}(r^2 - 2z^2) \tag{1.1.1}$$

where $R_0^2 = r_0^2 + 2z_0^2$, r_0 is the inner radius of the ring electrode and $2z_0$ is the distance between endcaps. The potential U_0 must be negative to trap positively charged particles ($U_0 < 0$). For negative ions the polarity of the voltage is the opposite ($U_0 > 0$). Fig 1.2 shows the electrostatic potential described by Eq. 1.1.1 for normalized coefficients ($U_0 = -1$ volts and $R_0 = 1$ mm) and for U_0 negative. From the curvature of this function, it is possible to see that the potential in the plane ϕz is attractive, whereas in the plane

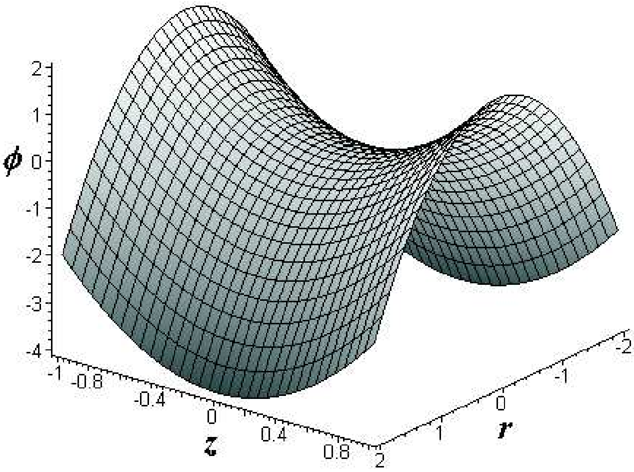

Figure 1.2: Three-dimensional electrostatic potential in a Penning trap.

ϕr it is repulsive. The axial magnetic field in these traps is added to balance the motion in the radial plane. As a result, the charged particles are then forced to move in orbits around the direction of the field compensating the electric force. In detail, the trajectories of ions inside a Penning trap can be calculated by considering the Lorentz force which describes the movement of a charged particle under the influence of magnetic and electric fields. This force is given by

$$\vec{F} = q(\vec{E} + \vec{v} \times \vec{B}) \tag{1.1.2}$$

where q is the charge of the particle, $\vec{v}$ is the velocity, $\vec{E}$ is the electric field and $\vec{B}$ is the magnetic field. In our case, the components of the electric field can be calculated from Eq. 1.1.1, as $E = -\nabla\phi$. These components are:

$$E_x = -\frac{\partial\phi(x,y,z)}{\partial x} = -\frac{2U_0}{R_0^2}x \tag{1.1.3}$$

$$E_y = -\frac{\partial\phi(x,y,z)}{\partial y} = -\frac{2U_0}{R_0^2}y \tag{1.1.4}$$

$$E_z = -\frac{\partial\phi(x,y,z)}{\partial z} = \frac{4U_0}{R_0^2}z \tag{1.1.5}$$

At this point it is important to notice that this electric field (or any other) must obey the Maxwell relationship $\nabla \cdot E = 0$. This fact will be useful in the following sections when calculating and verifying electric potentials for new configurations of ion traps.

Continuing with the expansion of the equation of motion, as the magnetic field is axially orientated, the components of the term $\vec{v}\times\vec{B}$ are:

$$\vec{v}\times\vec{B} \cdot \hat{x} = B\frac{\partial y}{\partial t} \tag{1.1.6}$$

$$\vec{v}\times\vec{B} \cdot \hat{y} = -B\frac{\partial x}{\partial t} \tag{1.1.7}$$

$$\vec{v}\times\vec{B} \cdot \hat{z} = 0 \tag{1.1.8}$$

As a result, combining these equations, the components of the Lorentz equation are:

$$\frac{\partial^2 x}{\partial t^2} = \frac{qB}{m}\frac{\partial y}{\partial t} - \frac{2qU_0}{mR_0^2}x \tag{1.1.9}$$

$$\frac{\partial^2 y}{\partial t^2} = -\frac{qB}{m}\frac{\partial x}{\partial t} - \frac{2qU_0}{mR_0^2}y \tag{1.1.10}$$

$$\frac{\partial^2 z}{\partial t^2} = \frac{4qU_0}{mR_0^2}z \tag{1.1.11}$$

where the axial motion is uncoupled and can be recognized as a harmonic oscillator when $U_0 < 0$ and $q > 0$. The frequency associated with this harmonic motion is called *the axial frequency* and is given by

$$\omega_z = \sqrt{\frac{4qU_0}{m{R_0}^2}} \tag{1.1.12}$$

In contrast to the axial case, the motion in the plane xy is not equally simple because it is dependent on both the electric and the magnetic field. A simplified form of these equations is obtained by neglecting the effect of the electric field. This leaves Eq. 1.1.2 as

$$\vec{F} \cdot \hat{r} = ma_c = qBv$$

where a_c is the centripetal acceleration. Fig 1.3 schematically shows this motion: a charged particle under the influence of a magnetic field perpendicular to its direction of motion. As the magnitude of this acceleration is given by $a = v^2/r$, it follows that

$$\frac{v}{r} = \frac{qB}{m}.$$

where the right part of the equation is the angular frequency of the particle defined as

$$\omega_c = \frac{qB}{m}$$

where ω_c is the called the *cyclotron frequency.*

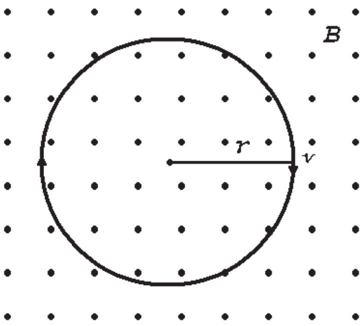

Figure 1.3: Circular motion (cyclotron motion) of a charged particle under the influence of a magnetic field. The dots indicate the magnetic field is directed out the page.

Combining this result with Eqns. 1.1.9, 1.1.10 and 2.1.9, the equations of motion for the x and the y directions can be rewritten as

$$\ddot{x} = \omega_c \dot{y} + \frac{\omega_z^2 x}{2} \tag{1.1.13}$$

$$\ddot{y} = -\omega_c \dot{x} + \frac{\omega_z^2 y}{2} \tag{1.1.14}$$

$$\ddot{z} = -\omega_z^2 z \tag{1.1.15}$$

With this new notation, it now easy to obtain the solution for the radial motion. For this purpose Eqns. 1.1.13 and 1.1.14 are then combined to obtain the following equation

$$\ddot{u} = -i\omega_c \dot{u} + \frac{1}{2}\omega_z^2 u \tag{1.1.16}$$

where $u = x + iy$. The well known solution for this differential equation is $u = e^{-i\omega t}$ which gives the two following characteristic frequencies. The first is

$$\omega_c' = \frac{\omega_c + \sqrt{\omega_c^2 - 2\omega_z^2}}{2} \tag{1.1.17}$$

which is called the *modified cyclotron frequency.* On the other hand, the second frequency is

$$\omega_m = \frac{\omega_c - \sqrt{\omega_c^2 - 2\omega_z^2}}{2} \tag{1.1.18}$$

and it is called the *magnetron frequency.* A very important fact that results from Eqns. 1.1.17 and 1.1.18 is the condition of the trap stability $\omega_c^2 > 2\omega_z^2$, which implies that not all the combinations of trap parameters produce a stable trap. The cyclotron frequency is always larger than the magnetron frequency and in normal operating conditions $\omega_c' \approx \omega_c \gg \omega_z \gg \omega_m$ [5]. The full motion in a Penning trap is given by the superposition of the components of these motions. An example of the motion inside a Penning trap is given in Fig. 1.4 for a singly ionized ion with a mass of 100 amu, see details in the caption.

Through these results, it is shown that the Penning trap can confine ions effectively. Many experiments have been carried out with Penning traps. As an example, at Imperial College, calcium, nitrogen and Magnesium ions are commonly trapped in a hyperbolic Penning trap [6], [7] and [8].

Although the Penning trap is widely used, it is not the only type of trap that has been successfully developed. The radiofrequency trap is another successful trap that has different properties and qualities.

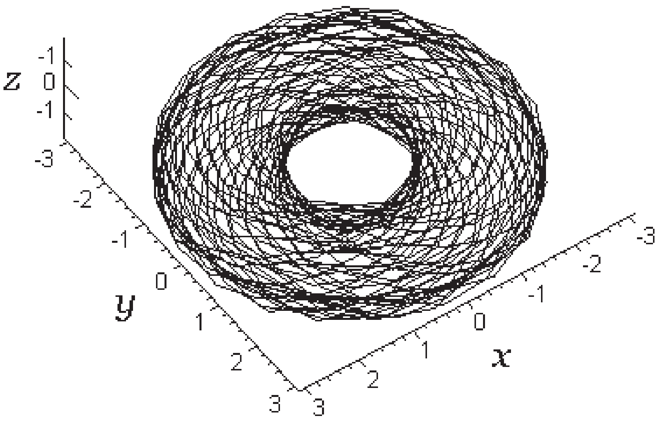

Figure 1.4: Simulation of the trajectory of a singly charged ion inside a Penning trap. Here, $U_0 = 8$ V, B= 5.87 T and m=100 amu and $\omega_+ = 898$ kHz, $\omega_- = 3.4$ kHz and $\omega_z = 78$ kHz, see [5]

1.2 Paul or radiofrequency traps

Paul or Radio Frequency (RF) traps utilize an AC electric potential combined with an electrostatic potential to confine charged particles. As the potential varies with time, ions feel a trapping and a repelling potential alternately. These traps are able to confine ions because on average, the electrodynamic potential generates a three dimensional pseudo-potential minimum. In the following sections the two most common designs for RF traps are presented: the hyperbolic and the linear RF traps.

1.2.1 Hyperbolic RF traps

Commonly, RF traps share with Penning traps the hyperbolic electrode geometry presented in Fig. 1.1. This is because this configuration is able to generate the precise spatial quadrupole potential described by Eq. 1.1.1. In fact, the electric potential in a hyperbolic RF trap has the same general form as in a Penning trap, the only difference is that an AC component has been incorporated into it, this is

$$\phi(r,z) = \frac{U_0 - V\cos\Omega t}{{R_0}^2}(r^2 - 2z^2) \tag{1.2.1}$$

where V is the amplitude and Ω the angular frequency of the AC signal. Following the same procedure as in the previous section, it is possible to theoretically determine the equation of motion of an ion through the use of the Lorentz force. As in this case there is no magnetic field, the Lorentz equation has only the term that corresponds to the electric field. Consequently, the equations of motion of the ion are

$$\ddot{r} = -\frac{2q}{mR_0^2}(U_0 - V\cos\Omega t)r \tag{1.2.2}$$

and

$$\ddot{z} = +\frac{4q}{mR_0^2}(U_0 - V\cos\Omega t)z \tag{1.2.3}$$

which can be recognized as Mathieu differential equations [5] which can be written in their canonical form[1] as

$$\frac{\partial^2 r}{\partial\zeta^2} + (a'_r - 2q'_r\cos 2\zeta)r = 0 \tag{1.2.4}$$

and

$$\frac{\partial^2 z}{\partial\zeta^2} + (a'_z - 2q'_z\cos 2\zeta)z = 0 \tag{1.2.5}$$

where $a'_z = -2a'_r = -\frac{16qU_0}{mR_0^2\Omega^2}$, $q'_z = -2q'_r = \frac{8qV}{mR_0^2\Omega^2}$ and $\zeta = \frac{\Omega t}{2}$.

Depending on the values q' and a', Mathieu equations have stable or unstable solutions, [5]. Stable solutions correspond to bounded functions and consequently they describe confined ion trajectories (a trapped ion). Recursion algorithms are often used to calculate the stability diagram of Mathieu equations in terms of the values q' and a'. As an example of this, Fig. 1.5 presents the stability diagram for the axial motion; these results were obtained with a Sträng's algorithm [9].

In an RF ion trap, the three dimensional confinement is achieved when simultaneously the axial and the radial parameters produce stable motions. An example of a three dimensional stability diagram is presented in Fig. 1.6,

---

[1] In the canonical form, Mathieu equations are usually presented with variables a and q. However, in this work, to avoid confusion with the charge q, Mathieu equations are presented with dashed letters (a' and q').

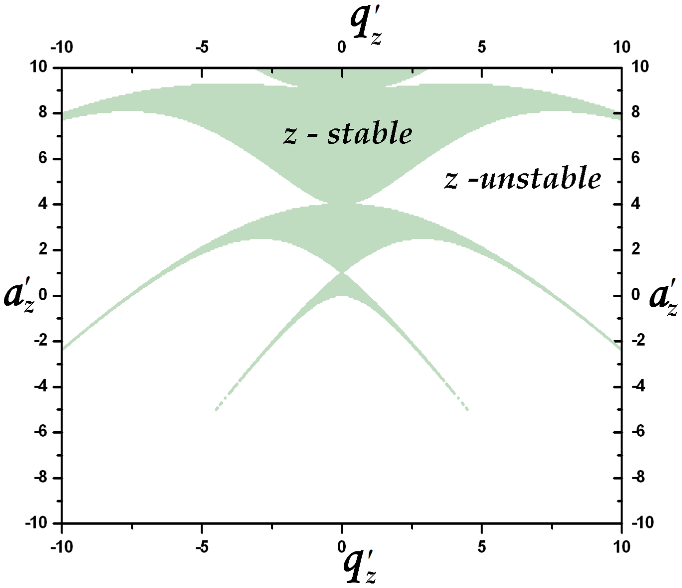

Figure 1.5: Stability diagram for the canonical Mathieu equation (axial motion). The stable region is presented in colour, the un-stable in white.

in this figure, the stability diagrams of the axial and the radial case have been superimposed.

In fact, as the stability regions depend on the parameters a'_z, q'_z, a'_r and q'_r, and these on the mass of the ion, RF traps can be mass-selective because only one ion species will produce a stable motion. This phenomenon is often very useful when running an ion trap as undesired species are not trapped.

Although the ion motion inside a RF ion trap is described by the stable solutions of Eqns. 1.2.4 and 1.2.5, a simple approximation can be made in order to extract some information about the ion motion inside the trap [10]. Axially, the force due to the dynamic electric potential is given by

$$F = m\frac{\partial^2 z}{\partial t^2} = \frac{V \cos \Omega t}{R_0^2} z. \tag{1.2.6}$$

If it is assumed that the motion in the axial direction follows the applied potential and that the original position z_0 is displaced an amount δ, then the position at any time can be expressed as

$$z = z_0 - \delta \cos \Omega t$$

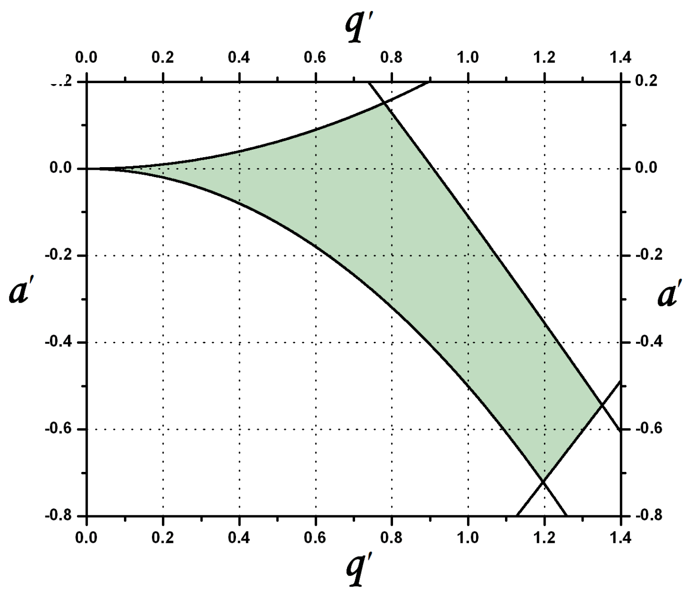

Figure 1.6: Three dimensional stability diagram for canonical Mathieu equations. When applied to RF traps, the diagram depends on the mass of the ion, its charge, and the applied voltages.

which implies that $\ddot{z} = \Omega^2 \delta \cos \Omega t$. Substituting this value into Eq. 1.2.6 and supposing small oscillations ($z \approx z_0$), it is possible to obtain the magnitude of the displacement

$$\delta = \frac{4qz_0V}{m\Omega^2 R_0^2}.$$

Then, calculating the average force over one period of the radio frequency ($2\pi/\Omega$), the expression for the force becomes

$$m\frac{\partial^2 z_0}{\partial t^2} = \frac{8q^2V^2z_0}{m\Omega^2 R_0^2}$$

which again has the form of simple harmonic oscillation with a natural frequency of

$$\omega_z = \frac{2\sqrt{2}qV}{m\Omega R_0^2}$$

This is called the secular frequency and it is smaller than the radio frequency.

Many experiments have been carried out with Paul traps. For example, unprecedented spectroscopic measurements on different ions have been performed using this type of ion trap. In particular, experiments with a single Ba^+ ion have been done since the early days of ion traps [5]. In addition to this, the geometry of RF traps can be modified to present a linear scalable design. This design is the so-called RF linear trap, which is explained in the following subsection.

1.2.2 Linear RF traps

Linear RF traps are able to store strings of ions in a linear array. This is possible because the linear trap provides confinement along one of the axes (the z axis in this case, Fig. 1.7) where ions can be trapped at different positions along it.

In a linear RF trap, the radial potential of the usual hyperbolic trap is replaced with a two-dimensional potential given by

$$\phi(x, y) = \frac{U_0 - V \cos \Omega t}{{R_0}^2}(x^2 - y^2) \tag{1.2.7}$$

The electrode structure required to produce this potential is shown in Fig. 1.7, see [11] and [5]. Two opposite rods are connected to a RF potential(V) meanwhile the other pair of rods is connected to an opposite potential (-V).

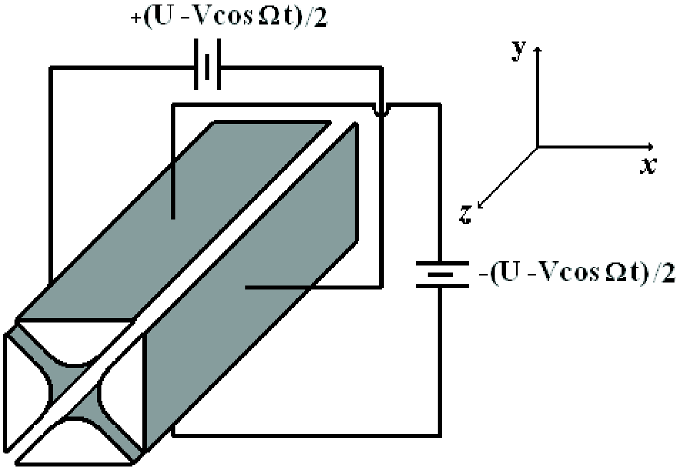

Figure 1.7: Electrode structure of the linear Paul trap

If the equation of motion is worked out as before, at the end three uncoupled equations can be obtained. These equations are

$$\ddot{x} = -\frac{2q}{mR_0^2}(U_0 - V\cos\Omega t)x \tag{1.2.8}$$

$$\ddot{y} = +\frac{2q}{mR_0^2}(U_0 - V\cos\Omega t)y \tag{1.2.9}$$

$$\ddot{z} = 0 \tag{1.2.10}$$

where the first two equations, Eqns. 1.2.8 and 1.2.9, are Mathieu equations and the last one is a simple linear ordinary differential equation [12]. It is important to notice that the structure shown in Fig. 1.7 is not a three dimensional trap, as the motion in the z direction is not confined. The solution of the equation of motion for the axial direction is direct and it shows that the charged particle follows a constant velocity along z. To solve the motions in the x and y axis the treatment is the same as before. Using the same substitution used for the hyperbolic RF trap, it is possible to obtain the following relationships

$$\frac{d^2x}{d\zeta^2} + (a' - 2q'\cos 2\zeta)x = 0$$

and

$$\frac{d^2y}{d\zeta^2} - (a' - 2q'\cos 2\zeta)y = 0$$

where, again, $a' = \frac{8qU_0}{mR_0^2\Omega^2}$, $q' = \frac{4qV}{mR_0^2\Omega^2}$ and $\zeta = \frac{\Omega t}{2}$. As before, bounded ion motions are given by stable solutions of both Mathieu equations; the stability diagram is shown in Fig 1.8.

The three dimensional confinement is achieved by the addition of two extra electrodes at both ends of the four-electrode array. These electrodes are usually connected to DC potentials to produce an axial harmonic oscillation of the ions along the z-axis. When ions are confined in traps with such electrodes, a string of ions can be created along the axial direction (along the electrodes). This creates a scheme where studies of particle interactions

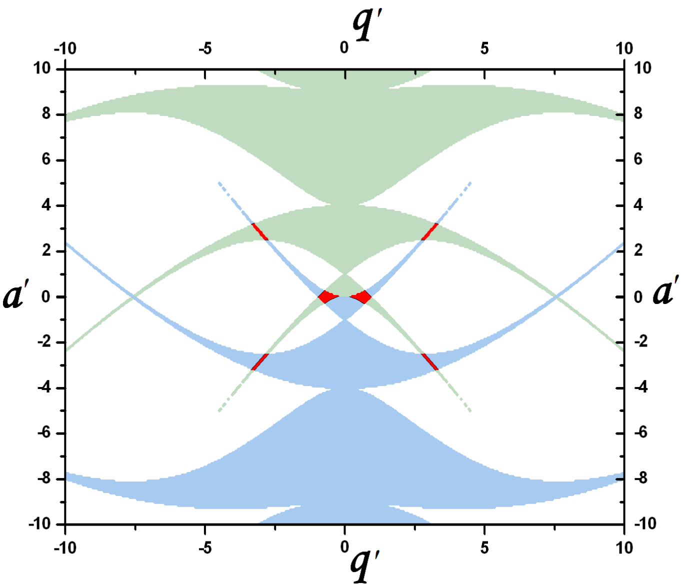

Figure 1.8: Stability diagram for linear traps. The stability region for the x motion is shown in blue and the stability region for the y motion is shown in green. The region where both motions are stable (trapping regions) is shown in red.

are possible. More important, this setup created the first scalable design of traps, in the sense that a multiple array of ions were trapped simultaneously in a trap. As a consequence, these traps have been constantly in the field of quantum computation; this topic is further explained in Section 1.5.4. Nowadays linear RF traps are used in studies of electric interaction with different ions, such as Ca^+ or Mg^+; see [13] for a detailed description. Usually in such experiments, ions are stored in traps made of four cylindrical rods with spacings of a few millimeters. Hyperbolic electrodes are often replaced by cylindrical rods in order to improve the optical accessibility to the trapped ions and also to facilitate the machining and construction of the trap [14]. These characteristics, the optical access and a simple design, play an important role in fields like spectroscopy and quantum computation, these two properties are explained in detail in the following section.

1.3 Other designs of ion traps

The recent application of ions traps in fields like spectroscopy and quantum computation have required changes to the traditional trap geometries. Hyperbolic and linear ion traps are widely used in different fields of science, but these designs have limitations. Hyperbolic traps restrict the optical access to the trapped ions and, as a consequence, its geometry is often modified for spectroscopy studies. These modifications include the drilling of holes into the endcaps and the ring electrode to send and collect light during the experiments. The price to pay for the extra amount of light collected, is a loss in the harmonicity of the trapping potential as it depends on the size of the holes. Bigger holes increase the solid angle for light collection but also imply an imperfect quadrupole potential and a non-harmonic ion motion. Another problem with the traditional design is that it is not scalable, a requirement demanded by quantum computation. Linear traps with cylindrical electrodes have to some extent overcome both problems but these traps are only scalable in one dimension. As a response to these limitations, other trap designs have been developed to present a higher scalability together with an open geometry and other capabilities. Some of these designs are presented in the following subsections.

1.3.1 Cylindrical traps

One of the most important limitations of hyperbolic ion traps is the fact that the optical access to the trapped ions is highly restricted by the trap electrodes. Moreover, hyperbolic electrodes are difficult to construct and their alignment is laborious and time consuming, [15]. Cylindrical traps were developed, to overcome these limitations, by Gerald Gabrielse at Harvard in 1984 [16]. The electrodes of the cylindrical trap can be connected to DC potentials to produce a Penning trap or to RF drivers to create the trapping conditions of a Paul trap, [16] [17]. In a cylindrical trap, both endcaps and the ring electrode are replaced by axially aligned cylindrical electrodes. This configuration can be modified by the addition of extra sets of cylindrical electrodes (called compensation electrodes) to eliminate lower-order non-harmonic terms in the potential, [15]. A schematic view of a cylindrical trap with an extra pair of compensation electrodes is shown in Fig. 1.9. These traps work because an axial electric potential minimum is generated at the centre of the ring electrode. As a result, this configuration can create trapping conditions either by the addition of a magnetic field or by connecting the electrodes to RF drivers.

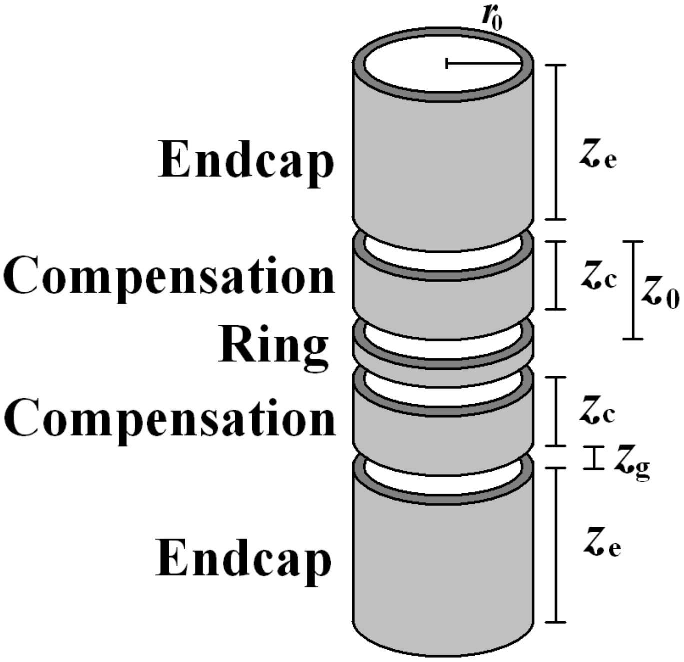

Figure 1.9: Schematic view of a cylindrical trap. This configuration includes two compensation electrodes to harmonize the electric potential at the centre of the trap.

The geometry of cylindrical traps solved two important limitations of hyperbolic traps: these traps are easily machinable and aligned, and their design permits the optical access to the trapped ions without further modifications. In addition, the potential of cylindrical traps can be analytically solved but the resulting potential is not purely quadratic, having anharmonicities represented as non-quadratic terms in the potential. However, as the expression for the potential is analytic, the dimensions and the voltages applied to the electrodes can be chosen to cancel out some anharmonic terms.

The electric potential generated by a Penning trap, as any other potential with azimuthal symmetry, can be expressed as an expansion of Legendre polynomials as

$$V = \frac{1}{2}V_0\sum_{n=0}^{\infty}C_k\left(\frac{r}{d}\right)^k\mathbf{P}_k(\cos\theta) \tag{1.3.1}$$

where d is the trap parameter $d^2 = \frac{1}{2}(z_0^2 + \frac{1}{2}r_0^2)$, V_0 is the magnitude of the electric potential applied to the endcap electrodes with respect to the ring, r_0 the inner radius of the trap, z_0 the distance from the centre of the trap to the endcap, and r and θ are the radial and angular coordinates. Furthermore, in a perfect hyperbolic trap, all the non-quadratic terms are zero. In contrast, in the case of cylindrical traps, all the even polynomial terms contribute to the total potential; the odd terms are zero as the electric potential must be finite in the centre [15]. As mentioned before, cylindrical traps can be formed with any number of cylindrical electrodes. Consequently, each extra cylindrical electrode contributes to the total potential. In the case of a trap with an extra set of electrodes (as the one in Fig. 1.9), the total electric potential has two contributions: one from the compensation electrodes and one from the endcaps. As a consequence, V can be written as the superposition of both potentials as

$$V = V_0\phi_0 + V_c\phi_c \tag{1.3.2}$$

where the V_0 is the magnitude of the electric potential applied to the endcap electrodes with respect to the ring and V_c is the magnitude of the electric potential applied to the compensation electrodes with respect to the ring. As both potentials preserve the azimuthal symmetry, they are written as

$$\phi_0 = \frac{1}{2}\sum_{n=0}^{\infty}C_k^{(0)}\left(\frac{r}{d}\right)^k\mathbf{P}_k(\cos\theta) \tag{1.3.3}$$

and

$$\phi_c = \frac{1}{2}\sum_{n=0}^{\infty}D_k\left(\frac{r}{d}\right)^k\mathbf{P}_k(\cos\theta) \tag{1.3.4}$$

Additionally, Eqns. 1.3.3, 1.3.4 and 1.3.2 can be combined to obtain the relationship

$$C_k = C_k^{(0)} + D_k\frac{V_c}{V_0} \tag{1.3.5}$$

As a result, any desired term (C_k) can be cancel out by adjusting the potential applied to the compensation electrodes (V_c). For example, to cancel out the first anharmonic term ($C_4 = 0$), the potential of the compensation electrodes has to follow the relationship

$$C_4 = 0 \qquad \Rightarrow \qquad \frac{V_c}{V_0} = -\frac{C_4^{(0)}}{D_4} \tag{1.3.6}$$

In the case of cylindrical traps, the terms ($C_k^{(0)}$ and D_k) can be obtained by simplifying Eqns. 1.3.3 and 1.3.4. These potentials can be expressed as zero order Bessel expansions due to the cylindrical symmetry and the symmetry under reflections across the z plane of cylindrical traps [15]. The potentials are written as

$$\phi_0 = \frac{1}{2}\sum_{n=0}^{\infty} A_n^{(0)} J_0(ik_n r)\cos(k_n z) \tag{1.3.7}$$

and

$$\phi_c = \frac{1}{2}\sum_{n=0}^{\infty} A_n^{(c)} J_0(ik_n r)\cos(k_n z) \tag{1.3.8}$$

where

$$k_n = \frac{(n+\frac{1}{2})\pi}{z_0 + z_e}, \tag{1.3.9}$$

z_e is the length of the endcaps, z_c is the length of the compensation electrodes and these equations have the boundary conditions presented in Fig. 1.10.

The coefficients of Eqns. 1.3.3 and 1.3.4, and 1.3.7 and 1.3.8, are related by the expressions

$$C_k^{(0)} = \frac{(-1)^{k/2}}{k!}\frac{\pi^{k-1}}{2^{k-3}}\left(\frac{d}{z_0 + z_e}\right)^k \sum_{n=0}^{\infty}(2n+1)^{k-1}\frac{A_n^{(0)}}{J_0(ik_n r_0)} \tag{1.3.10}$$

where

$$A_n^{(0)} = \frac{1}{2}\left\{(-1)^n - \sin(k_n z_0) - \sin[k_n(z_0 - z_c)]\right\} \tag{1.3.11}$$

and for coefficients D_k

$$D_k = \frac{(-1)^{k/2}}{k!}\frac{\pi^{k-1}}{2^{k-3}}\left(\frac{d}{z_0 + z_e}\right)^k \sum_{n=0}^{\infty}(2n+1)^{k-1}\frac{A_n^{(c)}}{J_0(ik_n r_0)} \tag{1.3.12}$$

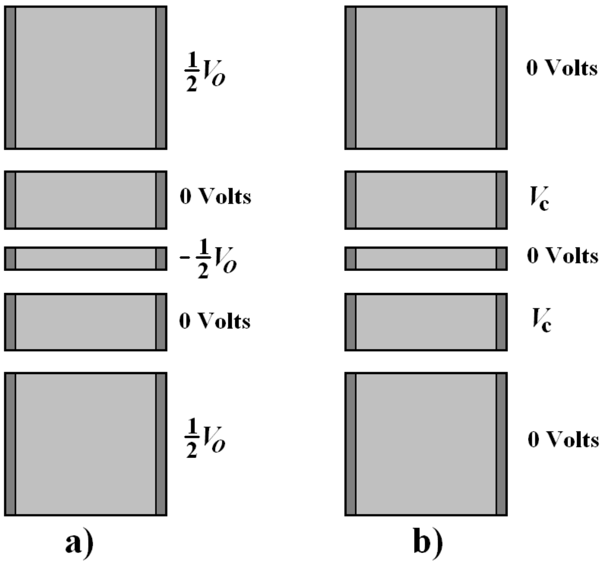

Figure 1.10: Boundary conditions for ϕ_0 (a) and ϕ_c (b).

where

$$A_n^{(c)} = \sin(k_n z_0) - \sin[k_n(z_0 - z_c)] \tag{1.3.13}$$

By using the latter equations, any specific expansion coefficient can be calculated and consequently tuned to zero to cancel out a specific anharmonic term. Although the latter expressions are infinite sums, these coefficients can be obtained by simple mathematical programming codes (a Maple code is presented in the Appendix, Ref. 8.1). An example of these results is shown in Table 1, [15].

Table 1: Expansion coefficients, Gabrielse design of 1989.

Expansion coefficients for a cylindrical trap with $r_0 = 0.6$ cm, $z_0 = 0.585$ cm, $z_c = 0.488$ cm and $z_e = 2.531$ cm		
$C_2^{(0)} = +0.544$	$D_2 = \ 0.000$	$C_2 = +0.544$
$C_4^{(0)} = -0.211$	$D_4 = -0.556$	$C_4 = \ 0.000$
$C_6^{(0)} = +0.163$	$D_6 = +0.430$	$C_6 = \ 0.000$
To cancel out quartic anharmonicities: $V_c = -0.3806\ V_0$		

Cylindrical traps have been successfully used in experiments where optical access to the trapping volume is required, [18]. In addition, they are a good alternative design to hyperbolic traps and their geometry is well suited to the geometry of super conductor magnets. Cylindrical traps have been often used since their proposal 20 years ago. During this time they have represented the main alternative to hyperbolic traps, but this is now changing as new alternatives have been proposed and operated in the last couple of years. In the following sections, novel designs for ion traps are presented.

1.3.2 The planar Penning trap

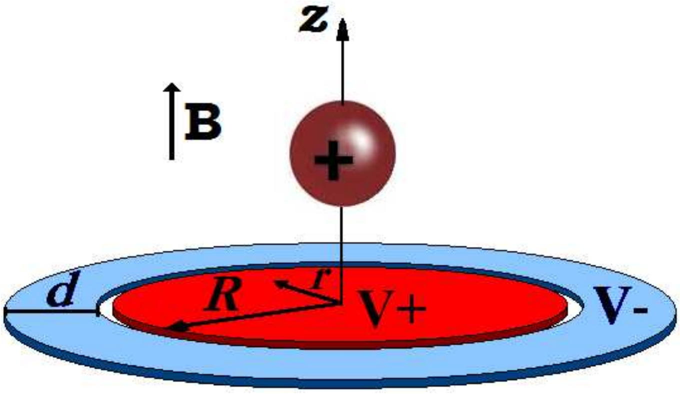

Figure 1.11: Schematic view of the planar Penning trap.

The planar trap is a new concept for a Penning trap [19]. This design was developed at the University of Mainz in Germany. From the point of view of the application to quantum computation, this new concept has many advantages over the conventional hyperbolic designs of traps. One of these advantages is the fact that it presents an open geometry and consequently trapped ions are easily accessible. A second advantage is that the trap itself is very easy to construct as it consists of a planar disk electrode surrounded by one or more planar rings. The number and the dimensions of the surrounding electrodes can be varied to adjust the depth or the quality of the trapping electrostatic potential. A third advantage, maybe the most important, is that the trap design is scalable as a large number of traps can be made on a single planar substrate. The geometry of the planar trap is shown in Fig. 1.11.

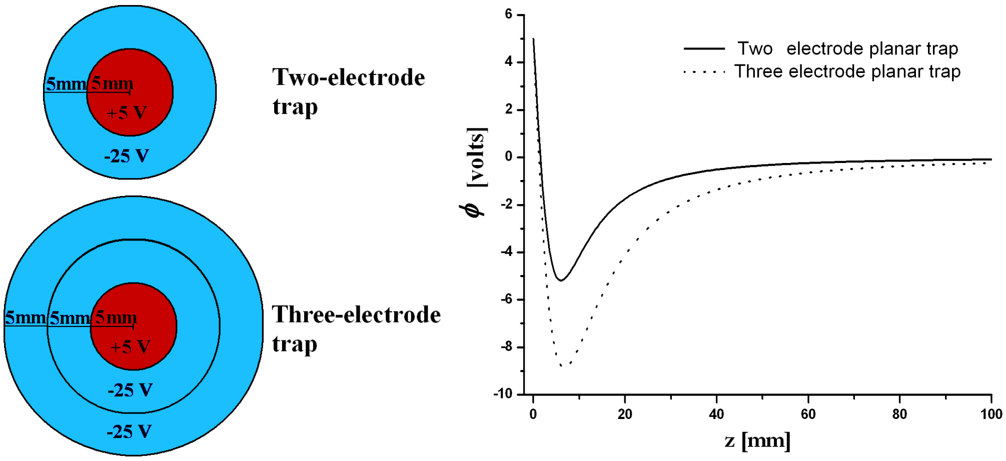

Figure 1.12: Axial electrostatic potential for a two-electrode and a three-electrode planar traps. Trapping conditions were chosen to trap positive charged ions. In both cases: $d_1 = 5$ mm, $R_1 = 5$ mm, $V_1 = +5$ V, $d_2 = 5$ mm, $R_2 = 10$ mm, $V_2 = -25$ V and additionally for the three electrode case $d_3 = 5$ mm, $R_3 = 15$ mm and $V_3 = -25$ V.

This trap is essentially a Penning trap because the final radial confinement is produced by a magnetic field perpendicular to the electrodes. When the electrodes are connected to their respective voltage, a trapping region above the plane of the electrodes can be produced. In this region the forces acting on a charged particle generated by the the electrodes cancel out; the particle feels an attractive force coming from the external ring which is compensated by a repulsive force coming from the central disk. The final three dimensional confinement is achieved by means of a magnetic field perpendicular to the electrodes. The trapping conditions (sign, depth and the quality of the potential, and the position of the trapping region) depend on the amplitude and sign of the voltages applied to the electrodes. Although the axial electric potential is not a pure quadrupole, it can be expressed analytically as

$$\phi(z) = \sum_{i=0}^{n} \phi_i(z) \tag{1.3.14}$$

where ϕ_i represents the contribution from each individual electrode and has the form

$$\phi_i(z) = V_i \left(\frac{1}{\sqrt{1 + \frac{(R_i - d_i)^2}{z^2}}} - \frac{1}{\sqrt{1 + \frac{R_i^2}{z^2}}} \right) \tag{1.3.15}$$

and

$$R_{i+1} = R_i + d_{i+1} \tag{1.3.16}$$

where R_i is the diameter, d_i the thickness and V_i the voltage of the electrode i (in this notation the central disk has a thickness and a diameter equal to $R_1 = d_1$, $R_0 = 0$) [19]. Two examples of the axial electrostatic potential for different conditions are shown in Fig. 1.12. Recently, a prototype of a planar trap was constructed at the University of Mainz. This trap was designed to trap electrons and its setup includes an electronic detection scheme [20]. The prototype was successfully tested, and there are plans for making a scalable setup. In addition, thinking about the construction of such a trap, some problems emerge when the connections to the electrodes are taken into account as they have to be connected from underneath making the scalable construction somehow difficult. A single trap of three electrodes would need three connections, a set of 4 would need 12 and set of n traps would need $3n$. Consequently, a large number of these traps would require an even larger number of connectors. However, the technology to control these connections is already available [19].

Planar traps in principle provide an open configuration that allows the construction of a two dimensional array of traps, overcoming two of the main limitations of traditional designs of ion traps. However, this design is not the only one to achieve these goals as at least other two proposals have been recently put forward. One of these alternative novel proposals is called the *chip trap* and is presented in the next section.

1.3.3 Chip RF trap

Linear RF and planar traps are some scalable examples among an increasing list of novel ion trap designs. In particular, it is common to find RF linear traps with a non-hyperbolic geometrical profile. In these cases the

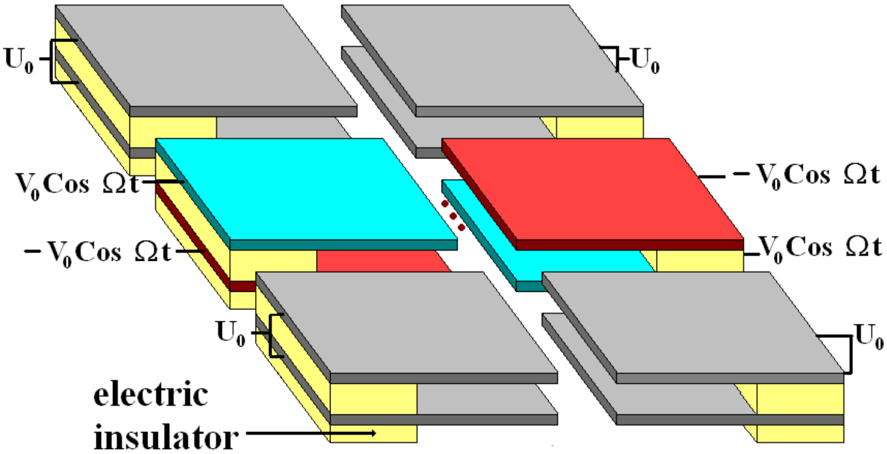

Figure 1.13: Schematic view of the RF Chip trap. Central electrodes are connected to the RF signal whereas the external wires are connected to DC potentials to generate the ion confinement.

hyperbolic-shaped electrodes have been replaced by sets of cylindrical or rectangular rods. A recently successful variation of these traps is the chip trap [21]. Although this trap is basically a linear RF trap, its design has been modified in such a way that the novel configuration leads to a scalable system where individual manipulation of ions is permitted. This novel design for a RF trap consists of rectangular electrodes divided into different segments. The design takes its name from the fact that the trap is built using techniques that are often used in semiconductors. The trap is created from three alternating layers of conductor material (AlGaAs) and two non-conductor layers of substrate (GaAs). Conductive and non-conductive layers are then etched to form electrodes, connectors and the trapping volume. A schematic view of this trap is presented in Fig. 1.13.

The chip trap consists of three sets of four rectangular electrodes. To produce trapping conditions, the central set of electrodes is connected to the RF drivers and the other two sets to DC potentials. A scalable design is straightforwardly created by adding more electrodes at the end of each trap. As the trap contains individual electrodes, the operation of each trap is independent. The expression for the potential in this trap cannot be written analytically, but the trap parameters were studied using computer simulations and ultimately the characterization of the trap was done empirically [22]. A prototype of this trap was very recently built and tested with $^{111}\mathrm{Cd}^+$ ions in the University of Michigan, USA [21].

Although the optical access in this trap is restricted by the substrate, the chip trap has many advantages over traditional designs as it can be miniaturized and is scalable; these are two important properties for quantum computation applications. In addition, the trap allows an independent manipulation of different ions in an array of traps.

In a later section (Section 2.2), a design that shares some of the advantages of the traps described above is presented and explained. This trap configuration is called the *wire-trap* and is one of the original contributions of this thesis. In the next section, some techniques used to perform experiments in ion traps are explained.

At this point, the basic principles of ion traps have been presented. Ion traps are more than a scientific or a mathematical curiosity: they are used in many fields of Physics. For example, ion traps are used to determine physical constants such as ion masses, transition frequencies and ion lifetimes. Furthermore, as these types of systems present a clean and an isolated environment, they provide excellent conditions for high resolution spectroscopy studies and provide a good setup for the construction of frequency standards. As the precision of these studies is limited by the velocity of ions, due to the Doppler effect, some techniques have been developed to decrease the velocity of the ions inside ion traps. In the following section these techniques are explained.

1.4 Cooling of trapped ions

Spectroscopic studies can be performed in ion traps with excellent resolution. This is because ion traps provide isolated environments where ions are confined and can be slowed down. As the frequency associated with a quantum transition is modified by Doppler effects, the best spectroscopic results are achieved when ions are cooled. In fact, spectroscopic measurements of narrow transitions in cooled trapped ions are currently being proposed as frequency standards due to their resolution [1]. In the following sections some mechanisms to cool ions inside traps are presented.

1.4.1 Laser cooling

The initial kinetic energy of trapped ions depends on the way they were created. If ions were created by, for example, atomic evaporation and electron bombardment in a trap with a trap bias of a few volts, their initial kinetic energy is in the region of a few electronvolts. Assuming thermal equilibrium, the temperature (T) of any particle, e.g. a trapped ion, can be estimated by $k_B T \sim K$, where k_B is the Boltzmann constant and K is the kinetic energy. From this relationship, given the mentioned initial kinetic energy, the temperature of the ions reaches more than thousands of Kelvin. In practice, trapped ions must be slowed down to perform high resolution experiments. In addition, slow ions can be confined easier and for longer times because their amplitude of oscillation is small. One common method to cool ions is laser cooling. This technique is often used to cooled down the ions in spectroscopy measurements to produce results at a very high resolution. The first laser cooling experiments in Penning traps were carried by Wineland and in RF traps by Dehmelt, both in 1978 [23] and [24].

The laser cooling technique works because of the transference of momentum between light (a laser beam) and neutral atoms or ions. In this process, an atomic transition is excited by a photon and depending on the direction of the ion with respect to the photon, this effect can slow down or speed up the ion. If the ion is moving towards the photon, the ion will be effectively slowed down. However, if they are moving in the same direction, the effect is the contrary. The ion stays in the same state until the photon is released. If the photon is re-emitted by stimulated emission, the emission will maintain the same direction as the laser beam and consequently no change in will be observed. On the other hand, if the photon re-emission occurs through spontaneous emission, the photon will be emitted in a random direction and on average (after the absorption/emission process is done many times) the motional state of the ion is changed. The average force due to the spontaneous emission is also known as *scattering force.*

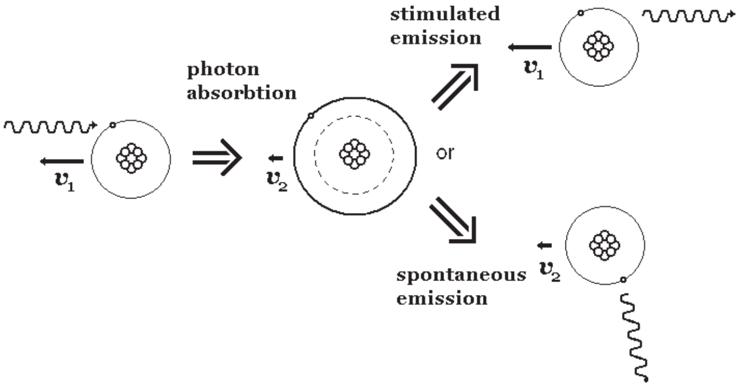

Figure 1.14: Schematic view of the laser cooling process. The horizontal velocity is effectively reduced only if spontaneous emission occurs.

A way to only slow down the ions is by Doppler cooling. The absorption of photons only takes place when a transition is excited by the right light frequency. If a laser is tuned to the frequency to excite an atom moving towards the laser beam, it will be at the wrong frequency to excite an ion moving in the opposite direction because the transition levels are modified by Doppler effects. This is useful because a “red detuned” laser (detuned to lower frequencies) just affects particles moving towards the light. As a consequence, a red detuned laser only slows down. Laser Doppler cooling is a dynamic process as a change on the velocity changes the effective transition frequency, and a change of the laser frequency must be made to continue the cooling process as the amount of the Doppler shift depends on the speed. Each photon that is absorbed and emitted removes a small quantity of energy, equivalent to the energy due to the detuning of the laser. This energy is $\hbar\delta$, where $\hbar$ is the Planck constant divided by 2π and δ is the detuning from resonance. The minimal temperature reached by the laser cooling is achieved when the scattering force compensates the dissipation [1]. Practically the optimum detuning is in the middle of the linewidth ($\delta \approx \gamma/2$), see [6]. At the minimal temperature point

$$K = k_B T = \frac{1}{2}\hbar\gamma$$

This gives the equation for the limiting temperature given by

$$T_{min} = \frac{\hbar\gamma}{2k_B}$$

which is called the Doppler limit. For ions like Mg^+ or Ca^+, γ is typically around 10^8 Hz, which allows temperatures of the order of 1 mK, see [1] and [6].

Laser cooling technique is not compatible with all the atomic species. This technique is only suitable for a few elements with the right transition structure and with a fast transition rate for fast cooling. A suitable structure for laser cooling can contain metastable states, but extra lasers must be used to pump these transitions until the system is sent back to the cooling cycle. In practice, this condition is very hard to achieve because the transition of each metastable level must be in the region where lasers are available. An example of an atomic structure that is commonly used in laser cooling is the structure of $^{40}Ca^+$ in Fig. 1.15. This ion has a strongly allowed dipole transition ($S_{1/2} \rightarrow P_{1/2}$) in the blue part of the visible spectrum. However, the excited state ($P_{1/2}$) can decay into an intermediate state, the $D_{3/2}$, as Fig. 1.15 shows. If the $D_{3/2}$ is populated then the laser cooling effect is switched off. To solve the problem an extra laser at 866 nm must be used to depopulate the state. In this particular experiment, both wavelengths (397 nm and 866 nm) can be obtained using diode lasers. The main cooling effect is given by the transition $S_{1/2} \rightarrow P_{1/2}$ because its rate ($\approx$ 20 MHz) is around 20 times larger than the rate of the transition $P_{1/2} \rightarrow D_{3/2}$ ($\approx$ 2 MHz).

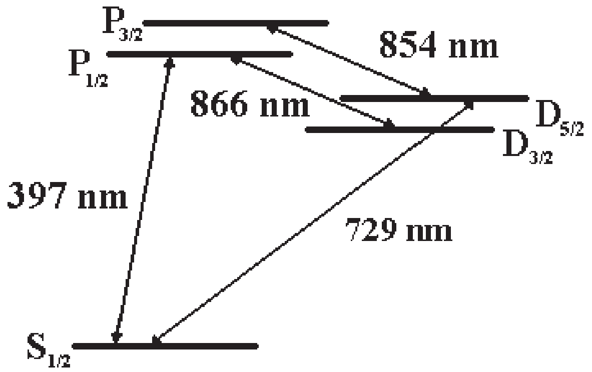

Figure 1.15: Example of energy levels, this case corresponds to ^{40}Ca^{+}, without the presence of a magnetic field (RF traps).

1.4.2 Sympathetic cooling

A cooling process that can be applied when two ion species are present in a trap is *sympathetic cooling* [5]. It works through the application of laser Doppler cooling to one of the ion species loaded into the trap. This technique is useful when the ion to cool does not present the correct energy structure necessary for the laser cooling. The cooling species is cooled by the usual technique and then, by momentum transfer (collisions), the laser cooled ions sympathetically cool the other ion species to their temperature. With this process, the main limitation of the laser cooling technique is overcome. As it was shown, laser cooling can be applied just to elements with appropriate transition energies, but applying the sympathetic cooling an indirect momentum transference can be made. In general, there are no limitations on the application of sympathetic cooling, which implies that any ion can be cooled by this technique. Other good characteristics of this type of cooling is that the internal states of the ion are not excited, which allows clean spectroscopy measurements of the trapped ion. One successful experiment involving sympathetic cooling is the cooling of ^{198}Hg^{+} through the laser cooling of ^{9}Be^{+} in a Penning trap [25]. In this experiment, laser cooling was applied to the ^{9}Be^{+} exciting the $2s^2S_{1/2} \rightarrow 2p^2P_{3/2}$ transition (313 nm laser beam). After the cooling, the ^{9}Be^{+} species was cooled down to 0.2 K whereas the ion ^{198}Hg^{+} was sympathetically cooled to a temperature of 1.8 K. The two ion species never reach the same temperature because of their centrifugal separation. Once both ion species are trapped in a Penning trap, they move in different orbits with different frequencies due to their difference in mass [26]. This effect produces a weak interaction between the ions and consequently they do not achieve thermal equilibrium.

1.4.3 Resistive cooling

One other cooling process applicable to ion traps is *resistive cooling* [27]. This technique works by coupling an external resistive electronic circuit to the trap electrodes. In this case the cooling process is generated by the dissipation of energy through a resistive element (R). In the trap, each single charged particle (q) generates an image charge q' on each electrode (endcaps). This image charge has the opposite sign to q and depends on its position in the way

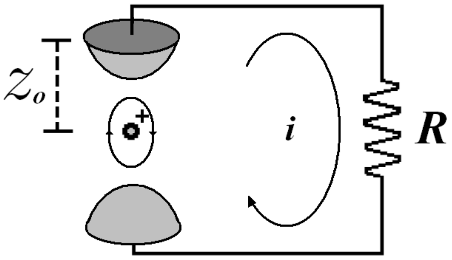

Figure 1.16: Schematic diagram of the resistive cooling

$$q' = -\frac{z_0 \pm z}{2z_0} q$$

where the ± indicates the electrode situated at $+z_0$ or $-z_0$ respectively. As was demonstrated before, inside the trap, ions are oscillating axially with frequency ω_z. Then, as any charged particle in movement can be seen as an electric current, the ion inside the trap produces a current over the external circuit. The value of this current is given by

$$\frac{dq'}{dt} = i = -\frac{d}{dt}(\frac{z_0 \pm z}{2z_0} q) = \mp \frac{q}{2z_0} \left\langle \frac{dz}{dt} \right\rangle$$

As the circuit is a closed loop, the energy will be dissipated at the rate

i^2R, this is

$$-\frac{dE}{dt} = i^2R = \frac{q^2}{4{z_0}^2}\left(\left\langle\frac{dz}{dt}\right\rangle\right)^2 \tag{1.4.1}$$

where $\langle\frac{dz}{dt}\rangle$ is the mean value of the axial velocity. As the ion motion inside the trap is harmonic, the axial velocity $(\frac{dz}{dt})$ can be written as

$$\frac{dz}{dt} = v_z \cos\omega_z t$$

therefore, $E = \langle m(\frac{dz}{dt})^2\rangle = \frac{1}{2}mv_z^2$. Incorporating this result to Eq. 1.4.1, the dissipation of energy is

$$-\frac{dE}{dt} = \frac{q^2R}{2m{z_0}^2}E$$

In addition, Eqn. 1.4.3 is a linear differential equation, [12]. To estimate the minimum temperature achieved by this method, Eq. 1.4.3 has to be integrated over the cooling time, this is

$$\int_{t_0}^{t_f}\frac{dE}{E} = -\int_{t_0}^{t_f}\frac{q^2R}{4m{z_0}^2}dt$$

where the dissipated energy is calculated from t_0 (the initial time) until t_f (final time). The solution to this integral is

$$\ln\frac{E(t_f)}{E(t_0)} = -\frac{q^2R}{4m{z_0}^2}(t_f - t_0)$$

Applying the approximation $E \approx k_BT$, the last equation can be expressed as

$$k_BT(t_f) = k_BT(t_0)\mathrm{e}^{-\frac{q^2R}{4m{z_0}^2}(t_f-t_0)}$$

or, in the simplified expression

$$T(t_f) = T(t_0)\mathrm{e}^{-\frac{q^2R}{4m{z_0}^2}(t_f-t_0)}$$

where the term $\frac{q^2R}{4m{z_0}^2}$ is called the natural time constant of the cooling process [5], $T(t_0)$ is initial temperature and $T(t_f)$ is the final temperature.

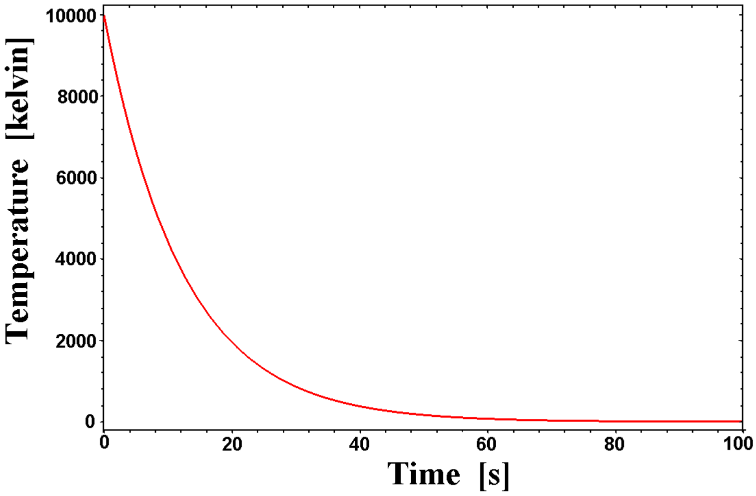

Figure 1.17: Typical temporal evolution of the resistive cooling

A typical curve of resistive cooling is presented on Fig. 1.17. This cooling curve is evaluated with typical experimental values [5] for a Mg^+ ion with $m = 4 \times 10^{-26}$ kg, $T(t_0) = 10$ kK, $q = 1.6 \times 10^{-19}$ C, with a dissipative circuit of $R = 1$ MΩ, and for a trap with $z_0 = 1.4$ mm. From this curve, it is possible to determine that a single ion can be drastically cooled in a few minutes. In addition, the resistive cooling is in principle applicable to any ion and to any quantity of them.

1.4.4 Buffer gas cooling

Another widely used cooling technique is buffer gas cooling. This is a fast cooling method which is commonly used because, like the sympathetic technique, it is independent of the type of the trapped ions to be cooled. It works by the transference of momentum between some inert gas like Helium or Argon and the trapped ions. Inert and light gasses are preferred to avoid recombination processes and a fast cooling rate. When the thermal equilibrium is achieved, the final temperature of the ions is equal to the temperature of the buffer gas. An effective cooling is achieved when the buffer gas is kept at a lower temperature. In practice, the buffer gas is in temperature equilibrium with the trap container, usually kept at cryogenic temperatures. When the thermal equilibrium is achieved, the velocity of the ions can be estimated using the relationship $E \approx Tk_B$. When atoms of Helium are used, in cryogenic environments, temperatures of 4 K can be achieved.

At this point, the general properties and capabilities of ion traps have been presented. These attributes have made ion traps a very powerful tool when performing experiments at high precision. There is a large number of applications of ion traps in science and technology; most of them related with the measurement of atomic properties. Some applications of ion traps, maybe the most common ones, are explained in the following section.

1.5 Applications of ion traps

Ion traps are capable of producing well isolated systems in which studies at high resolution can be performed. These studies range from measurements of mass and magnetic moments to quantum computation processes. Moreover, in the near future there are many proposed experiments on ion traps which will increase the precision of measurements of atomic and nuclear quantities, see [28], [29] and [30]. This section deals with experiments that can be currently carried out and also with one experiment that is under development and construction.

1.5.1 Mass measurements and electronic detection

As mentioned before, the motion of ions inside a Penning trap can be described as the combination of three oscillations. The frequencies related to these oscillations are called the *modified cyclotron* (ω_c'), *axial* (ω_z) and *magnetron frequency* (ω_m). For a derivation of these expressions see Section 1.1. Usually these frequencies are not harmonic frequencies of one another which implies that they are easily distinguished. These frequencies are defined by

$$\omega_c' = \frac{\omega_c + \sqrt{\omega_c^2 - 2\omega_z^2}}{2}$$

$$\omega_z = \sqrt{\frac{4qU_0}{m{R_0}^2}}$$

$$\omega_m = \frac{\omega_c - \sqrt{\omega_c^2 - 2\omega_z^2}}{2}$$

where m is the mass of the ion, q is the charge of the ion, U_0 is the magnitude of electrostatic potential, $R_0^2 = r_0^2 + 2z_0^2$ and ω_c is called the “true” cyclotron frequency. The cyclotron motion is the motion of a charged particle in a constant magnetic field, and its frequency is given by

$$\omega_c = \frac{qB}{m}$$

where B is the magnitude of the magnetic field. However, as the radial motion in the Penning trap is not due just to the magnetic field, the cyclotron frequency (ω_c) is modified by the presence of the electric field.

The important fact is that the three frequencies (ω_c', ω_z and ω_m) depend on atomic quantities as well as on external parameters (i.e. mass, charge, magnetic field, ...). Consequently, by the measurement of any of these frequencies and by the control of the external parameters, estimations of atomic properties can be performed. The confined charged particle inside the trap can be detected in different ways, for example through the detection of fluorescence from laser excitation of the ions or by the electronic detection of the motion at the axial frequency. The second case can be described as the inverse of the resistive cooling. In resistive cooling, the axial motion of the ion is coupled into an external circuit with electronic resistance R through the endcaps. This resistance component damps the oscillatory motion of the ion and it dissipates the kinetic energy of the ion cooling it. On the other hand, electronic detection is typically also made through the coupling of an external circuit to the endcaps; see [31] and [32] for references. Instead of modifying the motion of the trapped ions, this circuit monitors it. There are basically two types of electronic detection schemes: resonant and non-resonant. The non-resonant electronic detection scheme consists only of a detection device coupled into the endcaps, as shown in Fig. 1.18. With this setup, the elec-

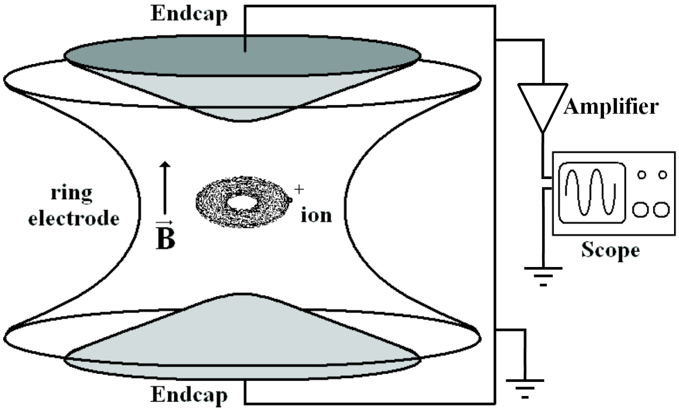

Figure 1.18: Schematic diagram of a non-resonant electronic detection scheme coupled into an ion trap.

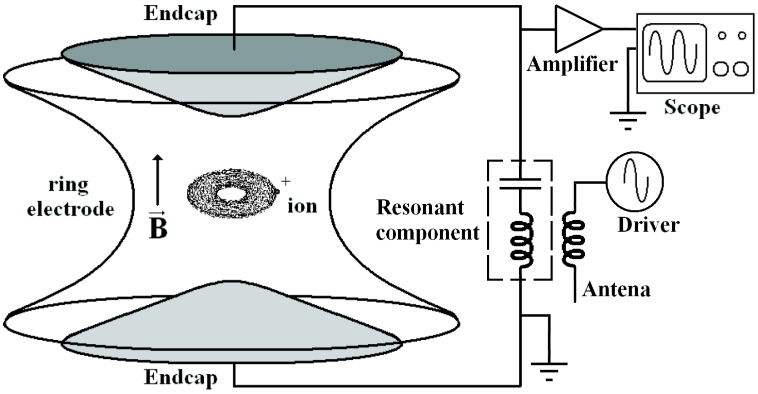

Figure 1.19: Schematic diagram of a resonant electronic detection scheme coupled into an ion trap.

tric signal generated by the moving charges and induced in in the endcaps is amplified and recorded by an external acquisition system. Finally, a Fourier transform of the data shows the frequency associated with the axial motion of the ions and from this frequency the mass of the ion species can be obtained. This type of detection is regularly used in non-harmonic traps with very low-noise environments (i.e. under cryogenic environments). For other traps, preferably harmonic traps, a resonant electronic detection setup is recommended. The only difference between a non-resonant and a resonant electronic detection scheme is that the latter incorporates a LC component in the setup. This change generates better results as the scheme is only susceptible to one frequency, making it less sensitive to environmental noise. In the resonant setup, a weak oscillating voltage is applied to the endcaps. For detection, the oscillation frequency of the trapped ions is changed until it matches the resonant frequency of the LC circuit; the frequency of the ions is usually changed by varying the trap bias. When both frequencies are the same, a drop in the amplitude of the oscillating drive is detected. At this point, the frequency of the drive is in resonance with the axial frequency of the ions and energy is transferred from the circuit to the ion. In other words, the energy is efficiently absorbed by the ion from the drive and then, a drop in the magnitude of the voltage will be observed. In practice, the amplitude of the applied voltage must be small, because in resonance the ion absorbs

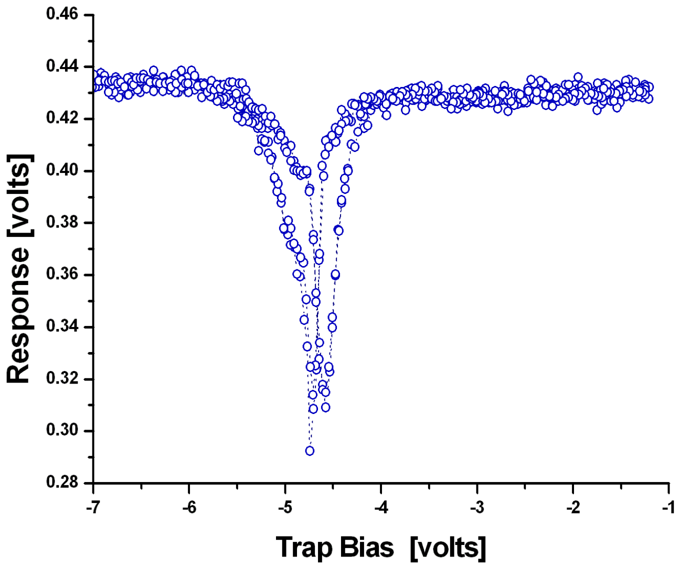

Figure 1.20: Resonant response of calcium ions inside a harmonic trap at Imperial College. The driver amplitude is 10.0 mV with a frequency of 145.5 kHz (which matches the resonant frequency of the LC circuit), endcaps are grounded and the trap bias is continuously scanned from -7.0 to -1.0 V.

energy efficiently, implying that it is perturbed also efficiently (heated). As a result, the resonant electronic detection is an intrusive technique as the ions are lost once they are detected. Consequently, this detection technique requires a continuous loading of ions into the trap. This is a disadvantage of the resonant setup; the non-resonant scheme is passive (it does not affect the motion of the ions). Resonant detection provides best results with highly-harmonic traps, where well-characterized motional frequencies are produced. In practice, this is difficult to achieve as most traps are not perfectly machined or are not designed to be harmonic. As a consequence, these traps do not produce a harmonic motion, and consequently the oscillation frequency of the ions is not a unique value but spread out over a wider spectrum.

A schematic diagram of the electronic detection scheme is shown in Fig. 1.19. In experimental conditions, the values of the LC components are chosen to produce an adequate resonant frequency. For example, Fig. 1.20 presents the response of a resonant electronic detection scheme for a hyperbolic Penning trap with $R_0 = 7$ mm when used to trap $^{40}\mathrm{Ca}^{+}$. The resonant frequency of the electronic setup is at 145.5 kHz, and is resonant with trapped ions in a trap bias of -4.5 V. During the detection, the trap bias is scanned between the range -7 to -1 V. The resonance effect is observed every time the scanning trap bias passes the resonant point. The hysteresis effects shown by the data in Fig. 1.20 are due to the direction of the scanning and the dynamics of the drive emptying the trap. These processes are complex because many phenomena are happening simultaneously. When the trap bias is being scanned from negative values towards zero, the trap is fully loaded as a large trapping potential depth allows the trapping of more ions. As the potential depth is being decreased, the trap losses ions. On the other hand, when the scan is being performed from lower potential depths towards large values, the amount of trapped ions is being increased, from a low number up to a maximum (at some point the trap becomes unstable). In addition to the latter effect, the ions does not respond instantaneously to the driver, an effect that also depends on the amount of trapped ions. Furthermore, it is well known that the motional frequencies (i.e. the axial frequency) can be shifted according to the number of ions [33]. Collectively, all these phenomena are reflected in the signal as hysteresis. For mass spectroscopy studies, the scanning range is usually large to cover the resonances of different ion species at different trap biases. Using the technique explained before, the masses of more than 150 isotopes have been successfully measured in Penning traps [34] with accuracies of $\delta m/m \approx 1 \times 10^{-7}$.

Although the measurement of ionic masses in Penning traps has been a useful application of ion traps, there are many other applications for which these traps are also being used. One frontline application of Penning traps is in the field of quantum optics, as outlined in the following examples.

1.5.2 Quantum jumps

As was stated before, the most impressive characteristic of ion traps is the possibility of carrying out experiments with a single ion. However, the preparation of a single ion in a trap can be difficult. To achieve this, the trap can be operated at the edge of the stability region while ions are loaded into the trap. Doing this, just a few ions will be trapped and, as the trap is almost unstable, the extra ions will be eventually lost. Alternatively, ions can also be created and loaded into the trap in a very small numbers using a well-characterized oven. In such experiments [8], single Mg atoms are created by heating magnesium deposited inside an oven. The oven consists of a small tantalum tube coiled by a tungsten wire. When an electrical current is passed through the wire, it heats the oven and the atoms escape through a small hole in the wall of the tube. Finally, the ionization is produced by electron bombardment; the electrons came from a hot filament near to the oven. After a detailed characterization, the oven is able to produce reliably very small numbers of atoms, [8]. Once a single ion is trapped and cooled, it can be used in experiments for long periods and in these cases, highly accurate measurements can be made. In this section, an optical method to determine the number of ions trapped is presented.

When the ions are trapped, in order to minimize the Doppler effect, they must be cooled. Laser cooling is a technique that provides a way to cool the trapped ions but also a way to detect them because the light scattered by spontaneous emission can be monitored. However, laser cooling is only applicable to a relatively small selection of atomic ion species. For efficient laser cooling and optical detection, a fast spontaneous emission frequency is required. For the transitions in Ca^+, shown in Fig. 1.21, the linewidths of the 397 nm, 854 nm and 729 nm transitions are 1.4×10^8 Hz, 9.9×10^6 Hz and 1.3 Hz respectively. Consequently, the 397 nm transition is used for laser cooling and fluorescence detection; the 866 nm transition has to be also addressed to pump the system back into the cooling cycle. In addition, if the ion gets into the $D_{5/2}$ state by off-resonant light, it must be re-pumped into the cycle $S_{1/2} \longleftrightarrow P_{3/2}$ in order to detect fluorescence again; this is done with a 854 nm laser. Once fluorescence is detected, the frequency of the laser can be tuned until one obtains efficient laser cooling. As an ultimate result, the detection of fluorescence can demonstrate the presence of individual ions through the observation of the so-called quantum jumps.

A quantum jump is a process in which an ion (or an atom) changes its energy level. These jumps are produced due to the absorption or emission

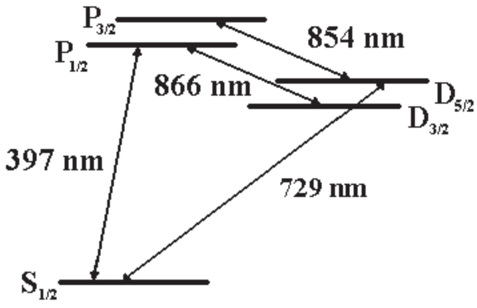

Figure 1.21: Example of energy levels, this case corresponds to Ca^+ without Zeeman splitting. Energy levels not to scale.

of photons. When a large quantity of ions is trapped, the fluorescence due to a change in the state of only one ion can not be observed because of the simultaneous emission of other ions. However, when the number of trapped ions is small, the direct observation of quantum jumps to a long-lived level is possible. In Fig. 1.22 a set of quantum jumps produced by two trapped calcium ions is presented. In Fig. 1.22 it is easy to identify the quantum jumps from two ions, as two well differentiated amplitudes can be distinguished. The largest amplitude corresponds to the case when the two ions are fluorescing, while the middle amplitude corresponds to the fluorescence of one ion. When the fluorescence falls to zero, both ions are in $D_{3/2}$ state. The

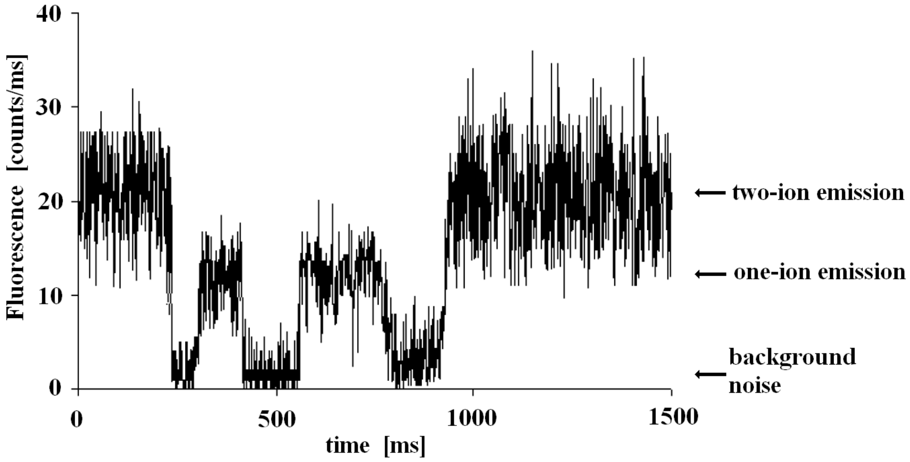

Figure 1.22: Fluorescence of 397 nm from two ions of Ca^+ in a RF trap, quantum jumps can be observed, experiment at Imperial College.

experimental observation of quantum jumps was a breakthrough in physics as it is tangible evidence of a quantum mechanical process. Ion traps are able to go further and test theories like Quantum Electrodynamics (QED). In such cases the experimental accuracy obtained can be even greater than that of the theoretical predictions. The next example is an application of ion traps that will provide unprecedented measurement of physical systems.

1.5.3 Spectroscopy of trapped ions, the HITRAP project

As has been mentioned, Penning traps allow the storage of ions for long periods of time and in such conditions that measurements at high resolution can be carried out. Some of these experiments allow critical tests of modern theories. Experiments proposed to generate, slow down and trap Highly Charged Ions (HCI[4]) in Penning traps fall in this category, [28] and [29]. In particular, hydrogen-like ions are the most interesting case as they present a simple system to study as electron-electron interactions, electronic screening effects, electronic spin-spin interactions, and angular momentum-spin interactions are non-existent in them. Due to these properties, calculations carried out for hydrogen like ions are simpler because few approximations need to be done. On the other hand, the hyperfine transition levels of highly charged ions are situated in the visible spectrum, which allows experiments in the range where lasers are available. As HCI are nowadays being produced at particle accelerators, a collaboration between different institutions in the European community has been proposed to perform a range of experiments including the spectroscopy study described above. The HITRAP project involves the design, construction and implementation of an ion trap for decelerating, capturing, and cooling highly charged ions [28]. The final experiment will be located in Darmstadt, Germany, where highly charged ions are produced at the GSI complex. Upon completion of this project, different high-sensitivity measurements of the ions will be possible as the project is a collaboration between groups specialized in different areas.

---

[4] The acronym HCI (Highly Charged Ions) should not be confused with HCl (HCl Hydrogen chloride or chlorhydric acid).

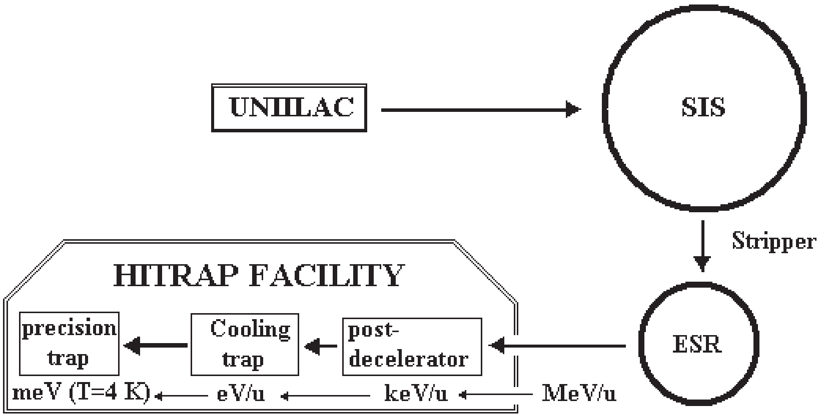

Figure 1.23: Schematic diagram of the HITRAP project [28].

One of the aims of the HITRAP project is to achieve the confinement of HCI in an ion trap. To fulfill this aspect, Imperial College has taken the responsibility to design, construct, test and operate a Penning trap for such purposes. Fig. 1.23 shows schematically the setup for HITRAP. The highly charged ions, like U^{91+}, are regularly produced at GSI; this complex includes an accelerator consisting of a Heavy Ion Synchrotron (SIS in the German abbreviations) and the Experimental Storage Ring (ESR). In this complex, two mechanisms are responsible for removing the electrons from neutral atoms. The first mechanism is by collision with solid targets of copper, see [28]. In this mechanism, called ionization by impact, singly ionized atoms are accelerated by the use of magnetic and electric fields inside the SIS. When the velocity of ions are similar to the velocity of the bound electrons, ions are deviated to hit a solid target (usually made of copper). The result of the collision is a multiply charged ion. The second mechanism used to remove the remaining electrons to create the highly charged state (or even the totally ionized state), is called ionization by electron bombardment. In this process, the previous multiply-charged ions are bombarded by electrons with at least three times the maximum binding energy of the remaining electrons; this condition guarantees no recombination. After this, HCI are left with energies of around 7 MeV. Under the HITRAP setup, these highly charged ions

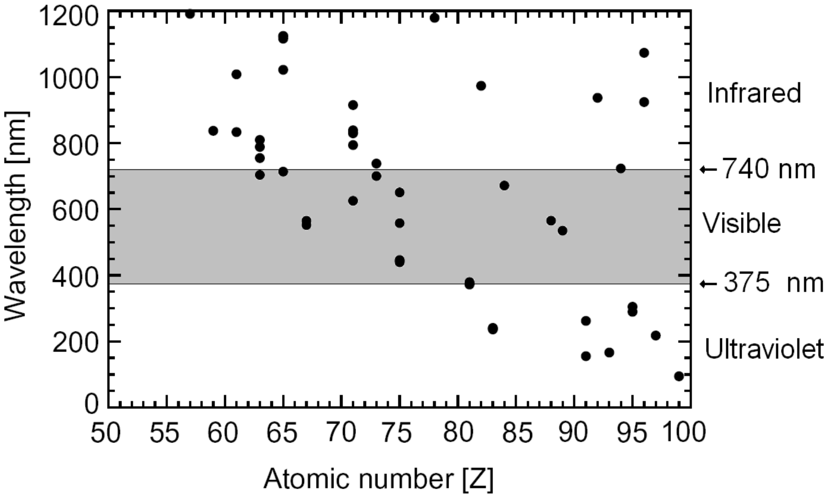

Figure 1.24: Wavelengths of the 1s ground state hyperfine splitting in the visible spectrum for atomic number Z [30].

will be cooled down to the level of a few electronvolts in the post-decelerator. This process is carried out in a Radio Frequency Quadrupole (RFQ) trap, where ions are cooled in a chain of electrostatic wall potentials. After the ions are cooled by this technique down the level of a few electronvolts, they will be transferred to the cooler trap. There, the ions will be cooled by resistive cooling (explained in section 1.4.3) down to temperatures of 4 K (meV) and made available in a low energy beam. As a HITRAP participant, the Imperial College team will perform spectroscopic studies on these ions in an separate Penning trap. It is expected that the HITRAP project will be ready at the end of 2007. At the moment, the RFQ trap, the cooler trap and the spectroscopy trap are under design and/or construction.

Once the HCI are cooled down to the few kelvin regime, many interesting experiments can be carried out. The Imperial College HITRAP proposal offers to perform spectroscopic studies of the hyperfine splitting (HFS) of the 1s ground state of hydrogen-like highly charged ions. In HCI, electronic transitions are generally in the far UV or X-ray regions of the electromagnetic spectrum. However, since the 1s ground state HFS scales with the atomic number Z as Z^3, the ground state HFS of some HCI is situated in, or close to, the visible spectrum where lasers are actually available, see Fig. 1.24, and thus spectroscopy studies of these lines can be carried out [30]. Measurements of these transition wavelengths will provide information about the spatial distribution of the nuclear magnetisation, a phenomenon that is not completely understood. Specifically, experiments with hydrogen-like lead (Pb^{+81}), hydrogen-like bismuth (Bi^{+82}) and lithium-like bismuth (Bi^{+80}) are proposed to be performed in the HITRAP facility. These experiments are until now, impossible to perform as no other source of HCI is available to produce ions at rest [28]. The design of the Imperial College HITRAP ion trap has to satisfy many requirements. The trap has to be able to: produce highly harmonic trapping potentials, support cryogenic environments, contain only Ultra-High Vacuum components, provide optical access and allow the collection of fluorescence from the trapped ions and finally, fit in the project specifications. The design of this trap is presented in Section 6.

1.5.4 Quantum Computation

One of the most promising applications of ion traps is in the field of quantum computation. The ultimate aim of this field is the creation of a computational device where the data storage and their operations are performed by means of quantum properties. In this scheme, data units can be described by any two-state quantum mechanical system; one state represents 0 ($|0\rangle$) and the other represents 1 ($|1\rangle$). By analogy with a classical computer, these data units are commonly named qubits. As a qubit is defined as a quantum system, its state must be represented as a quantum superposition of its internal states. The state of a qubit is written as

$$\phi = \alpha|0\rangle + \beta|1\rangle \tag{1.5.1}$$

where α and β are the amplitudes for finding the qubit in the state $|0\rangle$ or $|1\rangle$ respectively. Naturally, $|\alpha|^2 + |\beta|^2 = 1$ as the total probability is always 1; α and β are complex numbers. This quantum representation of the system shows an important difference with respect to the classical analogy. The state of a classical bit can only take two discrete values, 1 or 0. In contrast, the state of a qubit must be represented as the superposition of both states and, as α and β are continuous variables, the number of superposition states is infinite, [35]. A way to represent the state of a qubit in a more geometrical way is by re-writing α, β and the condition $|\alpha|^2 + |\beta|^2 = 1$ in terms of trigonometrical relationships of three real numbers, θ, φ and γ, as

$$\phi = e^{i\gamma}\left(\cos\frac{\theta}{2}|0\rangle + e^{i\varphi}\sin\frac{\theta}{2}|1\rangle\right) \tag{1.5.2}$$

where γ corresponds to a global phase without observable effects ([35]). This notation defines the state of a qubit as a point on a spherical surface in a three dimensional space. Using this notation, the *Bloch sphere* is a useful graphical representation of a qubit; an example of the sphere is shown in Fig. 1.25. As the number of points in the surface of the Bloch sphere is infinite, so is the number of superposition states. The idea of quantum computation was born from the fact that any operation performed on a qubit will be carried out on all the possible superposition states. As expected, when the operation is finished and then the results read, all the superposition states collapse into one state or the other making the operation no different from a classical process. However, the main idea in quantum computation, is to continue working with the superposition states by quantum operations or

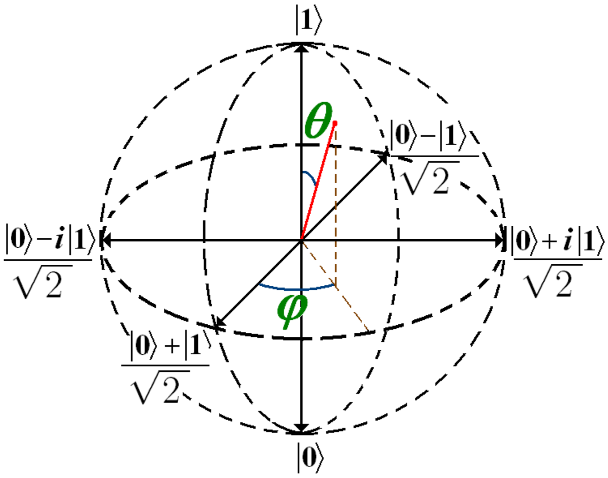

Figure 1.25: Bloch's representation of a qubit state. In this diagram it is easy to understand that there are an infinite number of points (superposition states, red dot) in the sphere surface.

algorithms until, from all the possible answers, only the desired one is likely to be obtained.

Computers work by the use of logic gates and, in principle, quantum computers will not be an exception to this rule. There are many types of logic gates, but it can be proved that any logic gate can be created from a combination of simple gates (one input, one output) and control gates (two or more inputs, two or more outputs). Consequently, any quantum computer scheme has to be able to produce a realization of these gates [35]. One of the simplest gates, that can be reproduced in a quantum system, is the NOT gate. This gate only inverts the logic value of the input. For example, if the input of a NOT gate is $|0\rangle$, then the output is $|1\rangle$ and viceversa. Practically, this gate can be realized in any two-level quantum system. A trapped ion with a narrow transition offers a good setup for this gate. The lowest level of the ion can be named as $|0\rangle$ and the upper one as $|1\rangle$. If the $|0\rangle$ state is populated, a single excitation (a photon) of the transition $|0\rangle \longrightarrow |1\rangle$ will transfer the ion to the $|1\rangle$ state, a second photon will provoke the stimulated emission of the first photon and then the system will go back to the $|0\rangle$ state. Effectively, single photons in this system act as a NOT gate transferring one state to the other and, if desired, back.

Unfortunately, the creation of a mechanism to simulate a control gate is not as simple as the one used in the NOT gate. Many proposals have been presented for a control gate, the most successful being the Cirac and Zoller scheme for a c-NOT (c for control) [36]. Basically, in the a c-NOT logic gate has a control input, a target input, a control output and a target output. The control output, after the logic operation, preserves the logical value of the control input. In contrast, the logical value of the target output depends on the values of the control and the target inputs. If the control input is true, the target output takes the value of the target input. On the other hand, if the control input is false, the value of the target output takes the inverse value of the operational input.

In the Cirac and Zoller scheme, the c-NOT gate is a three-step process in a two-ion/two-qubit system, [36]. To initialize, the two-ion system must be cooled down to the motional ground state. In the first step a π pulse[5] of frequency $\omega_0 - \omega_m$ is sent to the control qubit. In the second step, a 2π pulse is sent to the target qubit to excite the transition $|g_1\rangle \longrightarrow |\mathrm{aux}_0\rangle$. Finally, in the last step, another π pulse of frequency $\omega_0 - \omega_m$ is sent to control qubit. These steps have the effect of a control gate because only the control qubit is restored to its original state [36]. In Fig. 1.26 a diagram of these three steps process is presented; in the figure the subindex refers to the motional state. This graphic is only true when the control qubit is originally in its internal excited state ($|e_0\rangle$) and the target qubit in its internal ground internal . In the first step, the π pulse of frequency $\omega_0 - \omega_m$ is sent to the control qubit having the effect

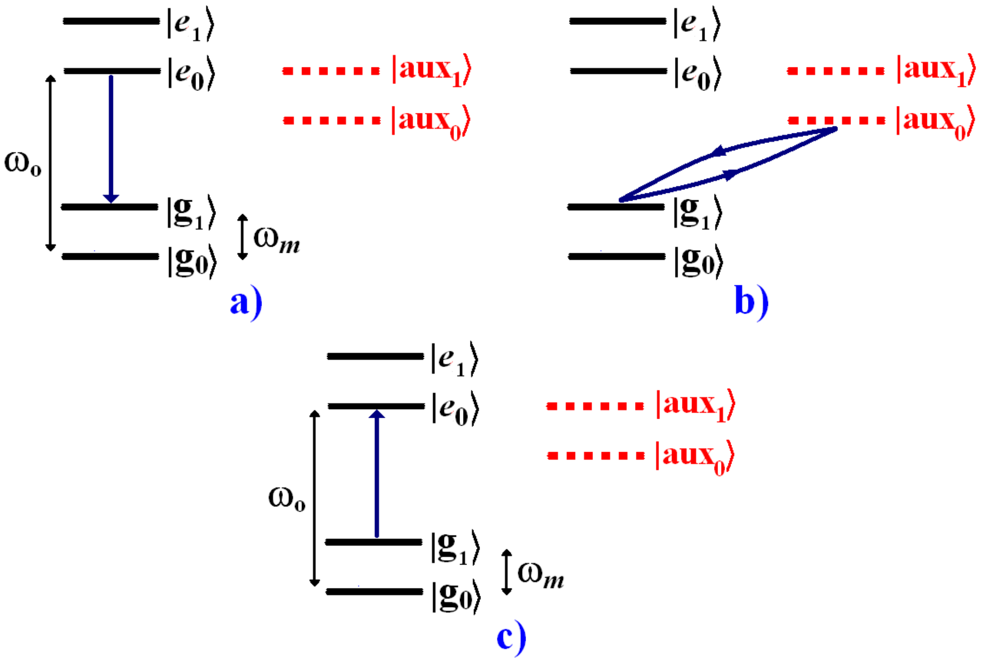

Figure 1.26: c-NOT gate. This scheme consists of two qbits in a three step process. Ions are in different vibrational states that are energetically separated by a phonon with an energy $2\pi\omega_m c$ (were c is the speed of light). The total result of the three-step process is that for certain initial conditions, the system is able to gain a phase.

$$|e_0\rangle \longrightarrow -i|g_1\rangle \tag{1.5.3}$$

---

[5] The length of a π pulse is Ω/π where Ω is the Rabi frequency for the transition.

where a (-i) phase was introduced. In the second step, a 2π pulse sends the target qubit to an auxiliary level and back producing a phase of -1, this is

$$-i|g_1\rangle \longrightarrow i|g_1\rangle \tag{1.5.4}$$

and finally, in the third step, a π pulse with the negative phase of the first pulse sends the control qubit back to its original motional state.

$$i|g_1\rangle \longrightarrow |e_0\rangle \tag{1.5.5}$$

If the control qubit is in the ground state during the first step of the process, nothing happens as the system cannot go further down the ground state (this the reason why the system must be in the motional ground state). The gate contains this specific steps so the qubits sometimes do not change their states because the pulses are not at the right frequency to excite them. The overall effect of these three pulses is to introduce a -1 phase factor only when the control qubit is initially in the state $|e_0\rangle$ and the target qubit in $|g_0\rangle$.

Computational processes, classical or quantum, require not only systems able to produce logical gates. Five requirements are compulsory; this set of conditions are usually refereed as the *Vicenzo's criteria* [35]. Any system that is proposed to perform computational processes is required to fulfill these criteria. Any system used to perform computational processes has to contain

1)Universal set of gates.

2)Long coherence times.

3)A mechanism to initialise bits (or qubits).

4)A way to measure the state of bits (or qubits).

5)A scalable design.

Ion traps are good candidates to produce quantum computational processes because they are one of the proposals that fulfill all the criteria. Ion traps can produce logical operations through the use of quantum gates, as was firstly proposed by Cirac and Zoller [36]. In addition, ion traps are able to produce systems where trapped particles can be stored for practically an indefinite amount of time at low temperatures and at ultra high vacuum where interactions with the environment are neglected. Thus both, the quantum and motional states can be created and maintained. Long coherence times (the time in which the internal and the motional states are well-defined) of up to minutes have been measured in ion traps [37]. In environments produced by ion traps, the state of a qubit can be reinitialised by electromagnetic radiation interactions. Finally, as a qubit represents a unit of information, a computational process requires a scalable design where an array of qubits can be independently addressed. For this requirement, one and two dimensional multi-trap arrays (linear RF and planar traps) have been constructed or are under development. These designs are called scalable because their geometries allow the construction of a number of traps in an array that can be used to produce an array of qubits.

From all the points discussed above, the scalability of ion traps is a field that has not evolved as fast or widely as one would expect. Currently, only a few configurations for ion trap configurations are able to produce an arbitrary number of traps in an array of electrodes: the linear RF trap and the planar trap (the chip trap is a modified RF linear trap). Historically, the linear RF trap was the first geometry to provide a scalable design. As a result, this trap has been extensively used in applications for quantum computation; the first implementation of the Cirac and Zoller logic gate was performed in these traps [38]. Although the linear RF trap is one-dimensional scalable, this capability is only useful for small numbers of ions. Recently, some proposals have also been presented where an array of cylindrical Penning traps are proposed as a quantum processor [39]. Penning traps have some important advantages over RF traps in quantum computation applications. The major source of decoherence in radiofrequency traps is due to magnetic field fluctuations. In RF traps with a scheme to correct the magnetic field fluctuations, coherence times up to 10 seconds have been achieved [40]. On the other hand, in Penning trap with similar schemes, coherence times up to 10 minutes have been achieved [37]. Another advantage of Penning traps is that they use constant electric and magnetic fields so the RF heating does not exist in these traps. With the arrival of the novel designs of ion traps, scalable Penning traps are now available for applications in quantum computation. The planar trap [19] is a good step forward but scalable designs of this trap have not been tested yet and some technical problems could arise during its construction due to the difficulty in connecting the electrodes among other things. To overcome these difficulties, in the following sections, alternative designs for ion traps are presented.

This section, was presented to give to the reader a brief perspective of the utility and use of ion traps. In the following sections, new designs of ion traps are presented together with the capabilities and advantages that they bring. These designs are an attempt to produce conditions where many ions can be individually addressed and are easily accessible. It is believed that these conditions will open a new range of applications for ion traps, ranging from quantum computation processes up to the transport of charged particles. Most of the following designs are original and they represent the main contribution of this work. Particular attention is given to the “wire-trap” as it is the design that is considered to be the most complete. The wire-trap is a design that was proposed, computer simulated and eventually tested at the Imperial College. The other novel designs are in some way based on the wire-trap.

2 Proposal of novel Penning planar traps

Ion traps have evolved in response to scientific needs and, as a consequence, they are widely used in different fields of science. Each new application of ion traps has brought changes either to the geometry of the ion traps or in their functions. RF traps allow the confinement of particles without the means of a magnetic field. Cylindrical traps provide easy optical access to the trapped ions and linear traps offer a scheme where a string of ions can be created (one-dimensional scalability). Planar traps were proposed as a response to the higher scalability needs of quantum computation and, as an alternative design, wire traps were developed based on an array of wires with an emphasis on the optical access and an easy construction. The geometries of two planar designs are presented in Fig. 2.1; Fig 2.1a shows the planar-rings trap and Fig. 2.1b shows the geometry of the planar guide. The planar trap has been explained in a previous section (Section 1.3.2); the planar guide and the wire trap are described below.

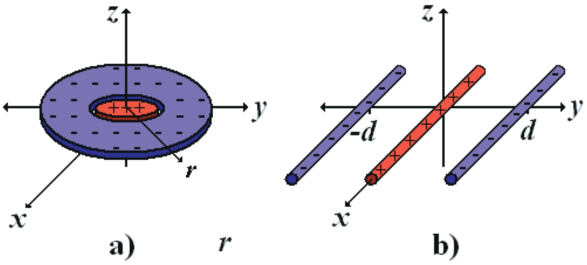

Figure 2.1: Two planar geometries for ion traps.

The planar guide, and its counterpart the wire trap, are novel designs of ion traps. The planar guide is able to confine the motion of ions along an array or wire electrodes. The wire trap has many advantages over traditional designs as it is able to create trapping conditions in three different spatial regions, is scalable in three-dimensions and is easy to construct as an array. Both designs, the guide and the trap, have an analytic trapping potential and so approximate values for motional frequencies can be found. From the manufacturing point of view these traps also have good properties, as an array of traps can be formed simply using long straight wires and the open geometry of this design means that the structure can be miniaturized using well-known techniques. Consequently, these traps are considered as excellent candidates for applications in quantum computation, mass and optical spectroscopy.

2.1 The planar guide

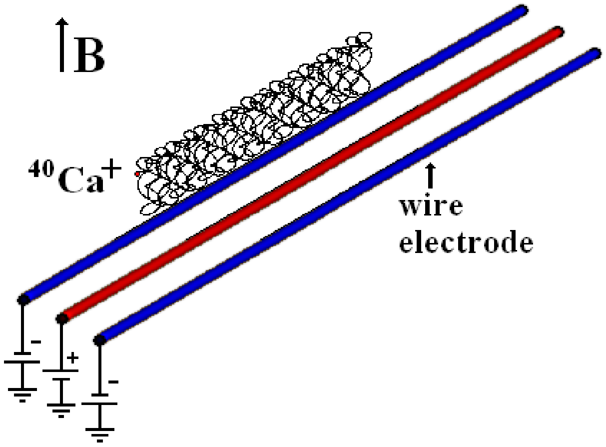

Figure 2.2: Schematic view of the planar guide. The simulated trajectory corresponds to a ^{40}Ca$^+$ ion with 0.1 eV. The central electrode is connected to +5 V and the external ones to -5 V, a magnetic field of 0.3 Tesla is pointing perpendicular to the direction of the wires.

In this section a novel design for an ion guide [41] is presented. The trap is simply made of three thin wire-electrodes or lines of charges. For trapping positive ions, the central wire would hold a positive charge (or be held at a positive voltage) and the external wires would hold a negative charge (or be held at a negative voltage). Under these conditions, trapping regions are created above and below the wires. In such zones the force coming from the central wire is compensated by the force coming from the outer parallel wires, Fig. 2.1 (b). Although this configuration is only able to trap ions along a line above the central wire, a closed loop or the addition of another perpendicular set of wires is enough to confine ions in all directions (see Section 2.2). The advantages of this trap over traditional designs are: it is scalable in a straightforward way, the expression for the electric potential can be analytically solved, and it is easy to implement in the laboratory.

In principle, any electrostatic potential can be obtained by solving Poisson's equation. In practice, charge distributions are usually too complicated and their associated Poisson equations cannot be solved analytically. However, for a few cases, the electrostatic field can be solved analytically through Gauss's law which can be expressed as

$$\nabla\cdot\vec{E} = \frac{q}{\epsilon_0}$$

where $\vec{E}$ is the electrostatic field, q is the enclosed charge and ϵ_0 is the permittivity of free space. The latter equation can be also written in its integral form as

$$\int \vec{E}\cdot dS = \frac{q}{\epsilon_0} \tag{2.1.1}$$

where S is a surface which surrounds the charge. For example, Eq. 2.1.1 can be easily used to find the electrostatic potential of an infinite line of charges. Using a cylindrical surface surrounding a line of charges parallel to x (Fig. 2.3), the solution of this problem is

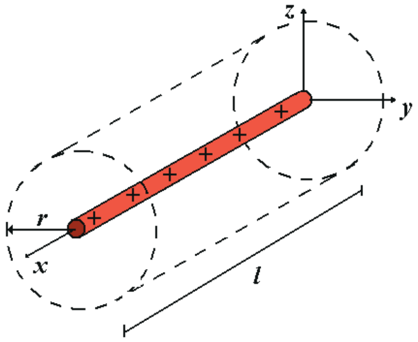

Figure 2.3: Geometry of the line of charges.

$$E = \frac{\sigma}{2\pi\epsilon_0 r} \tag{2.1.2}$$

where σ is the linear charge density [42]. Using Eq. 2.1.2, the electric potential can be easily calculated by direct integration and it is

$$\phi(r,z) = \frac{\sigma}{4\pi\epsilon_0}\ln\frac{R^2}{r^2}$$

Or, expressed in Cartesian coordinates

$$\phi(y,z) = \frac{\sigma}{4\pi\epsilon_0}\ln\frac{R^2}{(y-d)^2+(z-z_0)^2} \tag{2.1.3}$$

which is the well known potential for an isolated line charge at $(y = d, z = z_0)$, where R is an arbitrary distance at which the potential is set to zero, $R \gg d$ [42]. Following this result, by means of the superposition principle, the potential for a set of three equally-spaced charged lines placed along x, at $z = 0$, with line charges $-\sigma$ at $y = -d$, σ at $y = 0$ and $-\sigma$ at $y = +d$ (see Fig. 2.1 b), is

$$\phi = -\frac{\sigma}{4\pi\epsilon_0}\left(\ln\frac{R^2}{(y+d)^2+z^2} - \ln\frac{R^2}{y^2+z^2} + \ln\frac{R^2}{(y-d)^2+z^2}\right) \tag{2.1.4}$$

This arrangement generates a trapping potential along z for positively charged ions; if $\sigma < 0$ the trapping potential would be suitable for negatively charged ions. The form of the axial normalized potential, for $d = 0.1$ mm and $R = 1$ mm, is presented in Fig. 2.4.

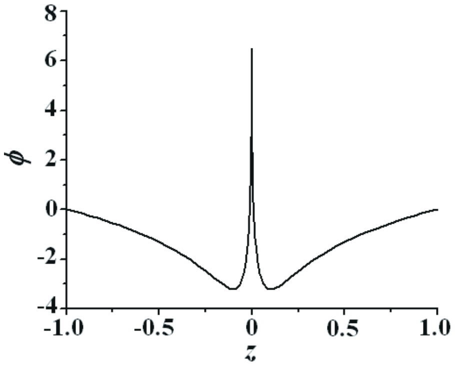

Figure 2.4: Electrostatic potential along the z axis, at $y = 0$ mm, $d = 0.1$ mm and $R = 1$ mm

The fact that two real minima are found, $(y_{min} = 0, z_{min} = \pm d)$, implies that charged particles can be trapped above and below the lines of charge at a distance d from the central wire. Although the expression for the potential is not accurately quadratic, as for a hyperbolic Penning trap, such a potential can be approximated by a Taylor expansion to second order around the stationary points $\xi(y = 0, z = z_{min})$, i.e.

$$\phi(y, z) = \phi(\xi) + \left.\frac{\partial^2 \phi}{\partial y^2}\right|_{\xi} y^2 + \left.\frac{\partial^2 \phi}{\partial z^2}\right|_{\xi} (z \mp d)^2$$

where

$$\left.\frac{\partial^2 \phi}{\partial x^2}\right|_{\xi} = 0$$

$$\left.\frac{\partial^2 \phi}{\partial y^2}\right|_{\xi} = \frac{\sigma}{2\pi\epsilon_0}\left(-\frac{8d^2}{(d^2+z^2)^2} + \frac{4}{d^2+z^2} - \frac{2}{z^2}\right)$$

$$\left.\frac{\partial^2 \phi}{\partial z^2}\right|_{\xi} = \frac{\sigma}{2\pi\epsilon_0}\left(-\frac{8z^2}{(d^2+z^2)^2} + \frac{4}{d^2+z^2} + \frac{2}{z^2}\right)$$

Consequently, the second order Taylor expansion around the stationary points becomes

$$\phi(y, z) \approx \frac{\sigma}{2\pi\epsilon_0}\left(\ln\frac{2d}{R} - \frac{y^2}{d^2} + \frac{(z \mp d)^2}{d^2}\right) \tag{2.1.5}$$

Using this potential, the components of the electromagnetic field are

$$E_x = -\frac{\partial \phi(y, z)}{\partial x} = 0 \tag{2.1.6}$$

$$E_y = -\frac{\partial \phi(y, z)}{\partial y} = \frac{\sigma}{\pi\epsilon_0 d^2} y \tag{2.1.7}$$

$$E_z = -\frac{\partial \phi(y, z)}{\partial z} = -\frac{\sigma}{\pi\epsilon_0 d^2}(z \mp d) \tag{2.1.8}$$

which are the formulae needed to obtain the equation of motion for a charged particle around the potential minimum along z. If a magnetic field (B) along z is added (as in the Penning trap), the equation of motion is found from the Lorentz force equation.

$$\vec{F} = q(\vec{E} + \vec{v}\times\vec{B}) = m\vec{a} \tag{2.1.9}$$

where $\vec{F}$ is the Lorentz force, q the charge of the particle, $\vec{v}$ the velocity, $\vec{E}$ is the electric field, $\vec{B}$ is the magnetic field, m is the mass of the particle and $\vec{a}$ is the acceleration. This equation of motion describes the movement of a charged particle under the influence of magnetic and electric fields. Under the conditions described above, this equation can be easily solved for the component along z because this motion is independent of the magnetic field: a similar deduction can be found in [5] for the Penning trap. Consequently, in the axial direction, the Lorentz force is

$$F_z = qE_z$$

which leaves the equation of motion in z as

$$\frac{d^2z'}{dt^2} = -\frac{q\sigma}{\pi m\epsilon_0 d^2}z' \tag{2.1.10}$$

where $z' = z \mp d$. The axial frequency associated with this harmonic motion is $\omega_z = \sqrt{q\sigma/\pi m\epsilon_0 d^2}$.

On the other hand, the movement in the xy plane is more complicated because the equations of motion for these dimensions are coupled. They are given by

$$\ddot{x} = \omega_c\dot{y} \tag{2.1.11}$$

$$\ddot{y} = -\omega_c\dot{x} + \omega_z^2 y \tag{2.1.12}$$

where the cyclotron frequency is defined by $\omega_c = qB/m$. For the arrangement described above, the equations of motion are not symmetric as they are in the Penning trap, but they still have an analytical solution. The solution for this system is given by the expressions

$$x(t) = c_1 + v_x^o t + c_2 \sin\omega_1 t + c_3 \cos\omega_1 t$$

$$y(t) = v_x^o\frac{\omega_c}{\omega_z^2} + \frac{\omega_1}{\omega_c}\left(c_2 \cos\omega_1 t - c_3 \sin\omega_1 t\right)$$

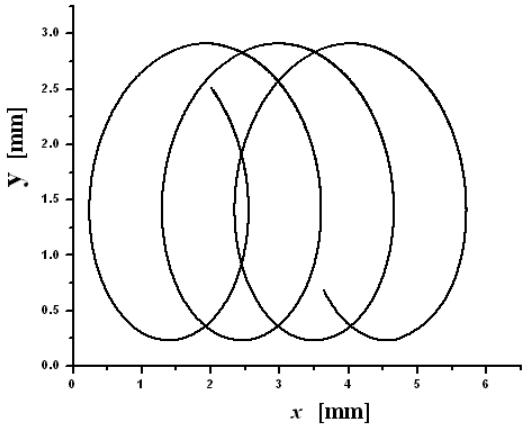

Figure 2.5: Motion of an $^{24}\mathrm{Mg}^{+}$ ion over the planar guide.

where $\omega_1 = \sqrt{\omega_c^2 - \omega_z^2}$ and consequently the oscillating solutions require the condition $\omega_c > \omega_z$. These equations represent an elliptical motion plus a linear drift along x (v_x^o). An example of this motion is presented in Fig. 2.5 for $^{24}\mathrm{Mg}^{+}$ under typical trapping conditions: $\omega_c = 630$ kHz and $\omega_z \approx 283$ kHz, $c_1 = 1$ mm, $c_2 = 1$ mm, $c_3 = 1$ mm, and $v_x^o = 100$ mm/s; [7].

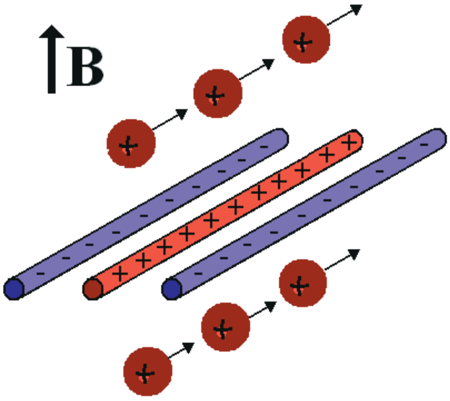

Figure 2.6: Schematic view of the direction of the ion drift velocity (v_x^o).

From these results it is easy to see that the potential produced by the three straight lines is not able to trap in three dimensions; the electrostatic potential traps axially and the magnetic field confines in one other dimension; the free dimension is the one along the charged lines. Consequently, we propose this setup as an ion guide because, under trapping conditions, ions would follow the "path" of the lines, see Fig. 2.6 for a schematic view.

A more general expression for the electrostatic potential created by the geometry of the planar guide, Eq. 2.1.4, can be found when the lines have different charge densities. Doing this, the position of the potential minimum along z can be modified. If different charge densities are taken in account, then the new potential can be written as

$$\phi = -\frac{1}{4\pi\epsilon_0}\left(\sigma_- \ln\frac{R^2}{(y+d)^2+z^2} - \sigma_+ \ln\frac{R^2}{y^2+z^2} + \sigma_- \ln\frac{R^2}{(y-d)^2+z^2}\right)$$

where $-\sigma_-$ is the linear charge density of the outer lines and σ_+ is the charge density of the central line. Then, the expression for the position of the potential minima is

$$z_{min} = \pm\sqrt{\frac{\gamma}{2-\gamma}}d \qquad (2.1.13)$$

where γ is the ratio of charge densities between the lines ($\gamma = \sigma_+/\sigma_-$). The variation of the position is presented graphically in Fig. 2.7. The position of the minimum can be adjusted with this method until the total charge is zero ($\gamma = 2$); after this point charged particles cannot be trapped (this potential corresponds to a linear charge quadrupole).

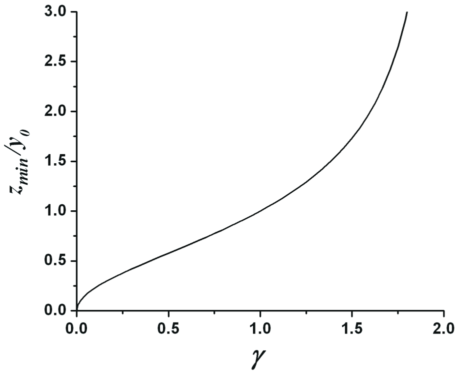

Figure 2.7: Relationship between the relative position of the minima along z and the ratio of the relative charge in the wires.

So far, the motion of the trapped ions has been solved assuming lines of charges. This would however be very hard to realize in practice. Fortunately, thin conductors connected to some potential are a good approximation to a line of charges and are easy to implement in the laboratory. A procedure to

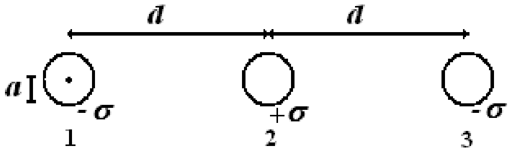

Figure 2.8: Schematic geometrical profile of the ion guide.

find the equivalence between linear charge densities and voltages, when the lines have the same magnitude of charge density, is through the following equations. From Fig. 2.8, the voltage at the surface of the outer wires can be approximated as

$$V_- = -\frac{\sigma}{2\pi\epsilon_0}\left(\ln\frac{R}{a} - \ln\frac{R}{d} + \ln\frac{R}{2d}\right) = -\frac{\sigma}{2\pi\epsilon_0}\ln\frac{R}{2a} \tag{2.1.14}$$

where a is the radius of the wire, as long as $a \ll d$. On the other hand, the voltage at the surface of the middle wire is

$$V_+ = -\frac{\sigma}{2\pi\epsilon_0}\left(\ln\frac{R}{d} - \ln\frac{R}{a} + \ln\frac{R}{d}\right) = -\frac{\sigma}{2\pi\epsilon_0}\ln\frac{Ra}{d^2} \tag{2.1.15}$$

Using these equations the following relationship is obtained

$$\frac{V_-}{V_+} = \frac{\ln(R/2a)}{\ln(Ra/d^2)} \tag{2.1.16}$$

Therefore, if these voltages are applied to the three wires, the potential generated is equivalent to that created by the three lines of charges. To illustrate this, the equipotential lines generated by a charge density ($|\sigma| = 1.16\times10^{-10}$ C/m) along the lines and the simulated equipotential lines generated by finite wires connected to the equivalent voltages ($V_+ = 2.00$ V and $V_- = -9.28$ V) are shown in Fig. 2.9 for $R = 50$ mm, $a = 1$ mm and $d = 10$ mm.

The immediate application of the ion guide presented here is in the transport of charged particles, however, an ion trap can also be made using this configuration. If the guiding wires are given a slight curvature, a closed track would then be able to produce the extra confinement required to trap the ions. If the radius of curvature (r_c) of the lines is much greater than d, the equations presented above would be a good approximation. The angular ve-

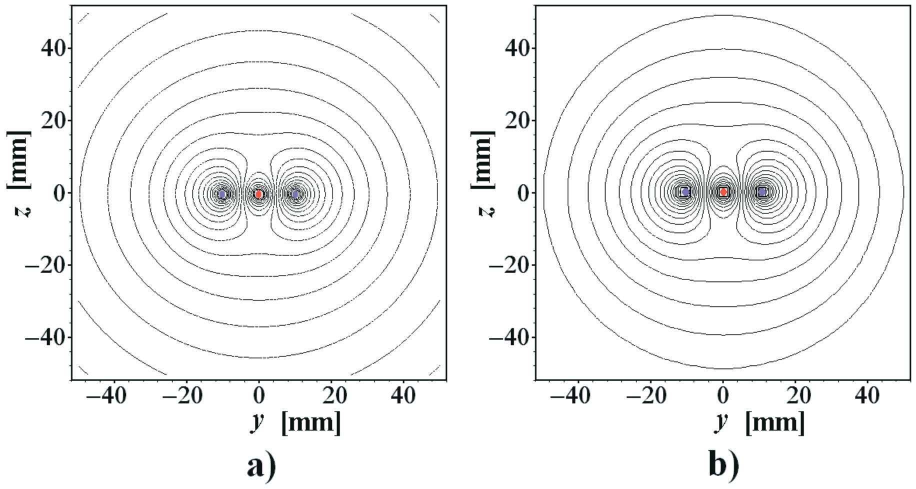

a)

b)

Figure 2.9: Equipotential lines for a) three lines of charge and b) three conductors at fixed voltages (simulation using SIMION). The potential lines are evaluated at the same voltages in both cases. In the case of b), the equipotential lines are limited by the position of the ground at $R = 50$ mm.

locity around the centre of the ring would come from the initial tangential velocity of the ion and is related to the linear drift term presented above as v_x^o.

Using wires connected to fixed voltages and with a grounded plate at some large distance, simulations were carried out confirming trapped ion trajectories. In Fig. 2.10 a simulated flight of an ion with $m = 60$ amu, $d = 10$ mm, $a = 1$ mm, $r_c = 70$ mm, $B = 0.50$ T, initial kinetic energy of 1 eV, $V_- = -9.28$ V and $V_+ = 2.00$ V (equivalent to $|\sigma| = 1.16 \times 10^{-10}$ C/m) is presented. These values were chosen to show a clear motion in the simulated trap.

The planar guide provides a novel way to confine ions in a two dimensional space, or alternatively in a path defined by the configuration of the wires. However, some applications of ion traps require the position of the ion to be well defined and all the directions of motion to be controllable. In order to overcome this aspect, a three-dimensional design based on the planar guide geometry is presented on the next section.

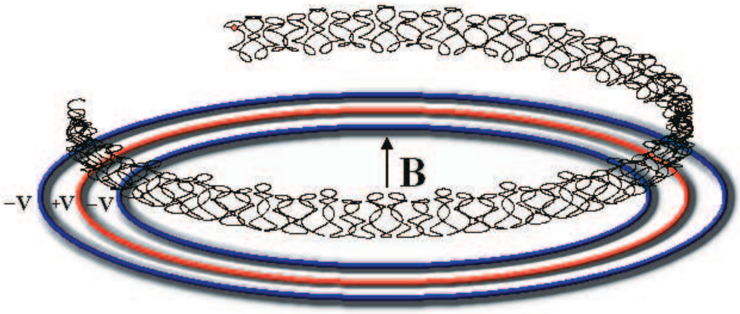

Figure 2.10: Simulation of the motion of an ion above the ion guide, $B = 0.5$ T, $V_{-} = -9.28$ V and $V_{+} = 2.00$ V. Simulation using SIMION.

2.2 The wire trap

The natural step to generate a three-dimensional trapping potential from the architecture of the guide trap, is to try to symmetrize Eq. 2.1.4. This is done, by adding to the existing two dimensional potential (in the plane yz) the potential generated in a perpendicular plane (xz) by another set of charged lines parallel to the y axis. The geometry presented in Fig. 2.11 produces such an effect.

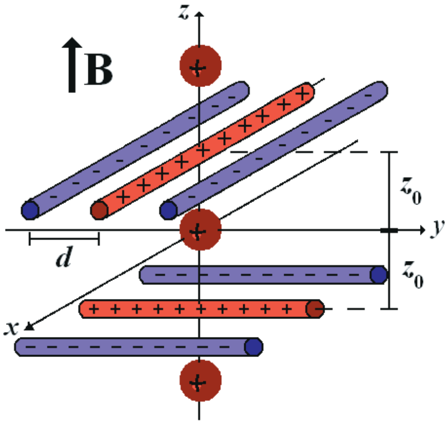

Figure 2.11: Schematic view of the wire trap, the scale is not preserved.

The potential generated by this geometry can be obtained by the superposition of two perpendicular planar guide potentials. Consequently, the full three-dimensional potential is

$$\begin{aligned}&\phi(x,y,z) = \\ &-\frac{\sigma}{4\pi\epsilon_0}\left(\ln\frac{R^2}{(x+d)^2+(z+z_0)^2}-\ln\frac{R^2}{x^2+(z+z_0)^2}+\ln\frac{R^2}{(x-d)^2+(z+z_0)^2}\right)\\ &-\frac{\sigma}{4\pi\epsilon_0}\left(\ln\frac{R^2}{(y+d)^2+(z-z_0)^2}-\ln\frac{R^2}{y^2+(z-z_0)^2}+\ln\frac{R^2}{(y-d)^2+(z-z_0)^2}\right)\end{aligned}$$

which represents the potential due to two perpendicular sets of three charged lines, separated by $2z_0$. The separation between charged lines in a single set is d. Now, following the same procedure used before it is possible to find the stationary points along the z direction. These points are $z_{min} = 0$ and

$$z_{min} = \pm\sqrt{z_0^2 \pm \sqrt{4z_0^2d^2 + d^4}} \tag{2.2.1}$$

On the other hand, if the lines have different relative charge, the positions of the minima are given by

$$z_{min} = \pm\frac{\sqrt{d_0^2(\gamma-1) + z_0^2(2-\gamma) \pm \sqrt{4\gamma(2-\gamma)z_0^2d^2 + d^4}}}{2-\gamma}, \tag{2.2.2}$$

where γ is the charge ratio between the lines. The main point is that in both cases (same charge or not), up to five stationary points can be found. The first stationary point is above the wires, the second one is below the wires, and, depending on the geometrical conditions, one or three points are situated symmetrically between the wires, see Figs. 2.12a) and 2.12b). Therefore, in principle, this trap would be able to trap ions above, below and between the lines.

The number of trapping points between the wires is conditioned by the number of real values of Eq. 2.2.1. For three stationary points, two potential minima and one potential maximum, the condition is

$$(z_0/d)^4 \geq 1 + 4(z_0/d)^2 \tag{2.2.3}$$

which implies that $(z_0/d)^2 > 2 + \sqrt{5}$ for the potential minima and $z = 0$ for the potential maximum. So, there is always a stationary point at $z = 0$ but, depending of the values of z_0 and d, other two real points can be created. In fact, the values of d and z_0 change the concavity of the stationary point at $z = 0$. This can be easily seen from the sign of the second derivative of the potential evaluated at $z = 0$. If this value is positive, the potential around this point would be concave and it would be able to trap positive ions (Fig. 2.12a). In contrast, if the value is negative, the potential between the wires would be convex and it would be able to trap negative ions (Fig. 2.12b). The condition to store positive ions at this point is then

$$\left.\frac{\partial^2\phi}{\partial z^2}\right|_{0,0,0} = \frac{\sigma}{4\pi\epsilon_0}\left(-16\frac{z_0^2}{(d^2+z_0^2)^2} + \frac{8}{d^2+z_0^2} + \frac{4}{z_0^2}\right) > 0 \qquad (2.2.4)$$

which implies that $(z_0/d)^2 < 2 + \sqrt{5}$. In other words, depending on the geometry, Eqns. 2.2.3 and 2.2.4, the potential has either one or two trapping regions for positive ions between the sets of lines. Continuing with the solution for the motion of the trapped ions and following the same procedure as before, the potential around the minimum $\xi = (x = 0, y = 0, z = z_{min})$ is approximately

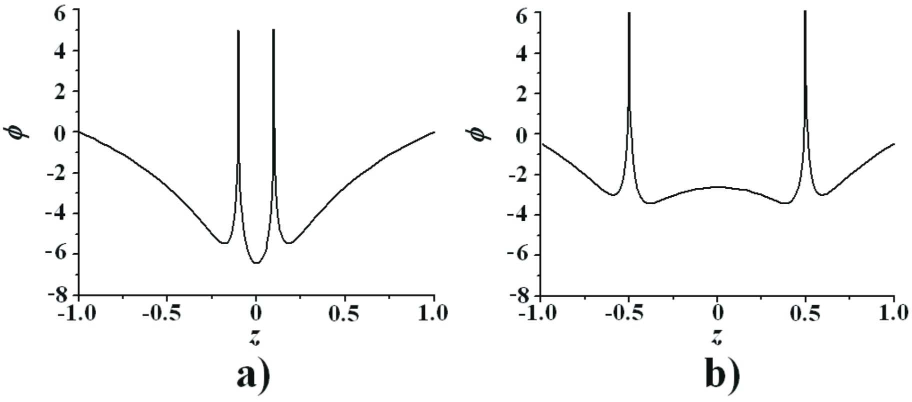

Figure 2.12: Potential along the z-direction. a) $z_0/d = 1$ and b) $z_0/d = 5$.

$$\phi(x,y,z) = \phi(\xi) + \left.\frac{\partial^2\phi}{\partial x^2}\right|_{\xi} x^2 + \left.\frac{\partial^2\phi}{\partial y^2}\right|_{\xi} y^2 + \left.\frac{\partial^2\phi}{\partial z^2}\right|_{\xi} (z - z_{min})^2$$

where

$$\left.\frac{\partial^2\phi}{\partial x^2}\right|_\xi = \frac{\sigma}{2\pi\epsilon_0}\left(\frac{2}{d^2+(z_{min}+z_0)^2} - \frac{1}{(z_{min}+z_0)^2} - \frac{4d^2}{(d^2+(z_{min}+z_0)^2)^2}\right)$$

$$\left.\frac{\partial^2\phi}{\partial y^2}\right|_\xi = \frac{\sigma}{2\pi\epsilon_0}\left(\frac{2}{d^2+(z_{min}-z_0)^2} - \frac{1}{(z_{min}-z_0)^2} - \frac{4d^2}{(d^2+(z_{min}-z_0)^2)^2}\right)$$

$$\begin{aligned}\left.\frac{\partial^2\phi}{\partial z^2}\right|_\xi &= \frac{\sigma}{2\pi\epsilon_0}\left(\frac{2}{d^2+(z_{min}+z_0)^2} + \frac{1}{(z_{min}+z_0)^2} - \frac{4(z_{min}+z_0)^2}{(d^2+(z_{min}+z_0)^2)^2}\right)\\ &+\frac{\sigma}{2\pi\epsilon_0}\left(\frac{2}{d^2+(z_{min}-z_0)^2} + \frac{1}{(z_{min}-z_0)^2} - \frac{4(z_{min}-z_0)^2}{(d^2+(z_{min}-z_0)^2)^2}\right)\end{aligned}$$

where the following relation is preserved (as expected from Maxwell's equations)

$$\left.\frac{\partial^2\phi}{\partial x^2}\right|_\xi + \left.\frac{\partial^2\phi}{\partial y^2}\right|_\xi + \left.\frac{\partial^2\phi}{\partial z^2}\right|_\xi = 0 \tag{2.2.5}$$

Then, the final equations of motion for trapped ions, assuming the existence of a magnetic field parallel to the z axis, are

$$\ddot{x} = \omega_c\dot{y} + \omega_x^2 x \tag{2.2.6}$$

$$\ddot{y} = -\omega_c\dot{x} + \omega_y^2 y \tag{2.2.7}$$

$$\ddot{z}' = -\omega_z^2 z' \tag{2.2.8}$$

where $\omega_x^2 = -\frac{2q}{m}\frac{\partial^2\phi}{\partial x^2}\Big|_\xi$, $\omega_y^2 = -\frac{2q}{m}\frac{\partial^2\phi}{\partial y^2}\Big|_\xi$, $\omega_z^2 = \frac{2q}{m}\frac{\partial^2\phi}{\partial z^2}\Big|_\xi$ and $z' = z - z_{min}$. Again, the equation for the axial motion is uncoupled and easily recognized as the harmonic oscillator equation.

In the case of the motion around ($z_{min} = 0$), Eqns. 2.2.6 and 2.2.7 can be simplified because

$$\omega_x^2 = \omega_y^2 = \frac{\omega_z^2}{2} = \frac{q\sigma}{m\pi\epsilon_0}\left(\frac{2}{d^2+z_0^2} + \frac{1}{z_0^2} - \frac{4z_0^2}{(d^2+z_0^2)^2}\right) \tag{2.2.9}$$

Using these relations, the equations of motion are

$$\ddot{x} = \omega_c \dot{y} + \frac{\omega_z^2}{2} x \tag{2.2.10}$$

$$\ddot{y} = -\omega_c \dot{x} + \frac{\omega_z^2}{2} y \tag{2.2.11}$$

$$\ddot{z} = -\omega_z^2 z \tag{2.2.12}$$

where the motion in the xy plane is symmetric and its solution is the same as in the Penning trap [5] and consequently stable ion motion parameters are when $\omega_c^2 > 2\omega_z^2$.

However, as mentioned before, ions can also be trapped in the other minima where $\omega_x \neq \omega_y$. There, their movement in the xy plane can be understood as an elliptical motion, [43]. A solution to Eqns. 2.2.6 and 2.2.7 can be proposed as

$$x = x_0 \mathrm{e}^{-i\omega_{xy} t}$$

$$y = y_0 \mathrm{e}^{-i(\omega_{xy} t + \pi/2)}$$

where ω_{xy} is the frequency associated with the plane xy. Substituting these expressions in the equation of motion, the following relationships are obtained

$$(\omega_{xy}^2 + \omega_x^2) x_0 - \ i\omega_{xy}\omega_c y_0 \mathrm{e}^{-i\pi/2} = 0$$

$$i\omega_{xy}\omega_c x_0 + (\omega_{xy}^2 + \omega_y^2) y_0 \mathrm{e}^{-i\pi/2} = 0$$

which have solutions

$$\omega_{xy}^2 = \frac{(\omega_c^2 - \omega_x^2 - \omega_y^2) \pm \sqrt{(\omega_c^2 - \omega_x^2 - \omega_y^2)^2 - 4(\omega_x^2 \omega_y^2)}}{2} \tag{2.2.13}$$

and

$$\frac{y_0^2}{x_0^2} = \frac{\omega_{xy}^2 + \omega_x^2}{\omega_{xy}^2 + \omega_y^2} \tag{2.2.14}$$

Finally, the full radial motion in the trap would consist of the linear superposition of the two solutions for ω_{xy}.

Although the latter equations are applied to lines of charges, the expres-

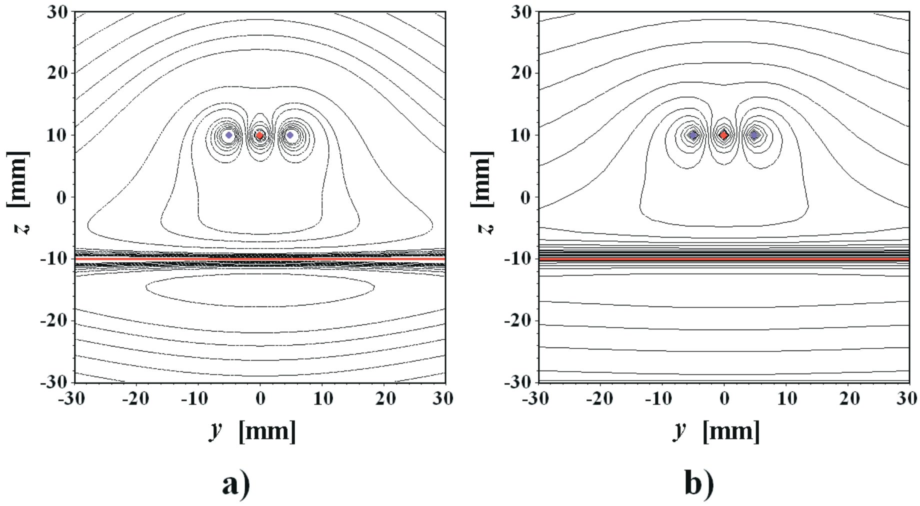

Figure 2.13: Equipotential lines at $x = 0$ mm for a) two perpendicular sets of linear charges (these calculations were performed using Maple) and b) two perpendicular sets of three conductors at fixed voltages (simulations using SIMION).

sions presented in Eqns. 2.1.15 and 2.1.14 can be used to approximate the equivalent voltages (when $z_0 << R$). In Fig. 2.13 equipotential lines are presented for a trap with the following characteristics: $|\sigma| = 1.2 \times 10^{-10}$ C/m (equivalent to $V_+ = 0.50$ V and $V_- = -8.26$), $R = 40$ mm, $a = 0.5$ mm, $d = 5$ mm and $z_0 = 10$ mm. The main differences in such graphs are because the simulations are limited in size, which restricts the size of R.

To demonstrate that the wire is able to trap charged particles, simulations were carried out using $^{40}\text{Ca}^+$ with the geometry $z_0 = 5$ mm, $a = 1$ mm, $d = 8$ mm, $R \approx 50$mm, $B = 0.60$ T and initial kinetic energy of 1 eV (typical experimental values [7]). Wires connected to $V_- = -13.04$ V and $V_+ = 1.00$ V were used (equivalent to $|\sigma| = 2.25 \times 10^{-10}$ C/m). The motion of such an ion in the upper trapping zone is shown in Fig. 2.14. Here $\omega_{xy}^+ = 856.95$ kHz and $\frac{y_0}{x_0}^+ = 0.88$, $\omega_{xy}^- = 9.83$ kHz and $\frac{y_0}{x_0}^- = 0.05$ for the two motions.

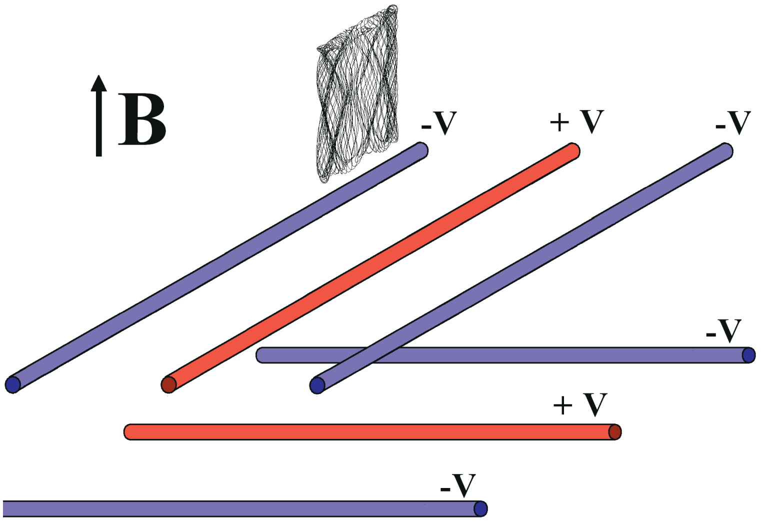

Figure 2.14: Simulation of the motion of a $^{40}\mathrm{Ca}^{+}$ ion on the top of a wire trap. Electrodes are connected to voltages: $V_{-} = -13.04$ volts and $V_{+} = 1.00$ volts.

2.3 The two-wire trap

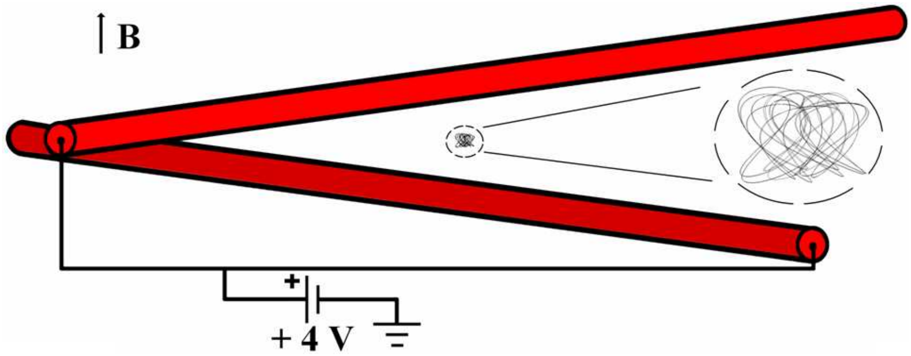

Figure 2.15: Simulation of the motion of a $^{40}\mathrm{Ca}^{+}$ ion in a two-wire trap. Ion kinetic energy $= 1 \times 10^{-2}$ eV, $a = 0.5$ mm, $z_0 = 2$ mm and $B = 1.3$ T. Simulated with SIMION.

In fact, it is easy to demonstrate that a wire trap can also be designed with just two wires [44]. Using the same notation as in Eq. 2.1.4, the electrostatic potential of two crossing wires separated by $2z_0$ is

$$\phi = \frac{\sigma}{4\pi\epsilon_0}\left(\ln\frac{R^2}{y^2+(z-z_0)^2} + \ln\frac{R^2}{x^2+(z+z_0)^2}\right) \tag{2.3.1}$$

or, using a similar analysis to that in the previous section, the potential can be written in terms of voltages as

$$\phi = \frac{V_+}{\ln(R^2/az_0)}\left(\ln\frac{R^2}{y^2+(z-z_0)^2} + \ln\frac{R^2}{x^2+(z+z_0)^2}\right) \tag{2.3.2}$$

where V_+ is the electric potential of the wires are connected with respect to a ground at R. The axial potential in Eq. 2.3.2 presents a minimum at $z = 0$ where positive charged particles can be confined, see Fig. 2.16. To trap negatives ions the voltage at the wires has to be negative.

Following the same procedure as in previous sections, the potential around the minimum $\xi = (x = 0, y = 0, z = z_{min})$ can be approximated by

$$\phi(x,y,z) = \phi(\xi) + \frac{\partial^2\phi}{\partial x^2}\bigg|_{\xi} x^2 + \frac{\partial^2\phi}{\partial y^2}\bigg|_{\xi} y^2 + \frac{\partial^2\phi}{\partial z^2}\bigg|_{\xi} (z-z_{min})^2$$

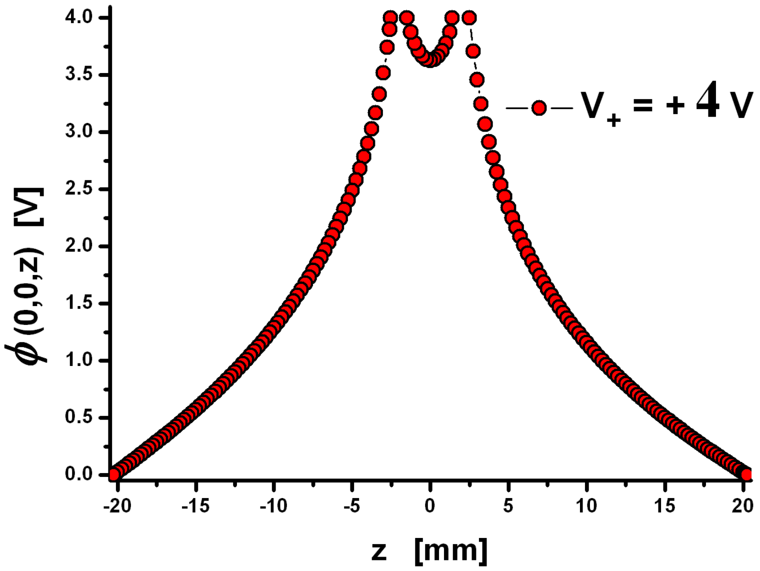

Figure 2.16: Potential along the z direction, $V_+ = 4$ volts, $a = 0.5$mm, $z_0 = 2$ mm and $R = 20$ mm.

where, in this case,

$$\left.\frac{\partial^2\phi}{\partial x^2}\right|_{z_{min}} = -\frac{2V_+}{\ln(R^2/az_0)}\left(\frac{1}{(z_{min}+z_0)^2}\right)$$

$$\left.\frac{\partial^2\phi}{\partial y^2}\right|_{z_{min}} = -\frac{2V_+}{\ln(R^2/az_0)}\left(\frac{1}{(z_{min}-z_0)^2}\right)$$

$$\left.\frac{\partial^2\phi}{\partial z^2}\right|_{z_{min}} = \frac{2V_+}{\ln(R^2/az_0)}\left(\frac{1}{(z_{min}+z_0)^2}+\frac{1}{(z_{min}-z_0)^2}\right)$$

Consequently, the approximated potential for the two-wire trap is given by

$$\phi = \frac{2V_+}{\ln(R^2/az_0)}\left(2\ln\frac{R}{z_0} - \frac{1}{z_0^2}x^2 - \frac{1}{z_0^2}y^2 + \frac{2}{z_0^2}z^2\right). \qquad (2.3.3)$$

The two-wire trap has been designed as a Penning trap, as a result, a magnetic field has to be incorporated to the equation of motion. Consequently, according to the Lorentz force equation, the motion of the ions will be determined by the electrostatic potential, Eq. 2.3.3, and a constant axial magnetic field (B). The result is a set of three equations of motion that govern the three directions of motion of the ions. These equations, as in hyperbolic Penning traps, are

$$\ddot{x} = \omega_c \dot{y} + \frac{\omega_z^2}{2} x$$

$$\ddot{y} = -\omega_c \dot{x} + \frac{\omega_z^2}{2} y$$

$$\ddot{z} = -\omega_z^2 z$$

which are the familiar equations of motion of an ion inside a Penning trap, where m is the mass of the ion, $\omega_z^2 = 8qV_+/mz_0^2 \ln(R^2/az_0)$ and $\omega_c = qB/m$.

The two-wire and the six-wire traps differ on their properties. Although the two-wire trap has a very simplistic design and an even better optical access than the six-wire design, it does not have all the properties that make the six-wire design more suitable for quantum computation applications. Firstly, the two-wire trap does not produce trapping regions above and below the trap geometry, so it is not as versatile as the six-wire counterpart. Secondly, neither the harmonicity nor the shape of the potential can be modified in the two-wire trap as there is only one independent parameter (the voltage in both electrodes). Thirdly, the six-wire design allows the control of the position of the trapping zones above and below the wires; the two-wire trap does not even produce such trapping points. The latter property is an important requirement in applications where trap-trap interactions have to be controlled; this is explained in Section 4.5. In contrast, the geometry of the two-wire trap is easier to construct and scale. Although the two-wire trap does not have all the properties of the six-wire design, its design provides an excellent setup for spectroscopic studies. In Fig. 2.15 a simulation of a trapped Ca^+ is presented when the electrodes of a two-wire trap are connected to +4 V, see details in the figure caption.

2.4 Scalability

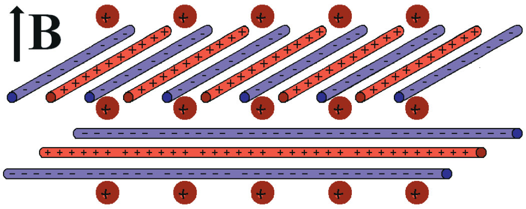

Figure 2.17: Schematic view of the planar multiple trap. In practice, the potential at the different trapping points are not all the same since this depends on how close a trap is to the edge of the whole structure.

One of the great advantages of the wire trap is its high scalability, see Fig. 2.17. The equation to solve for a large square array of wires, when n^2 wires are used to produce m^2 traps (where n is the number of wires in a plane and and $n = 2m + 1$), is

$$\begin{aligned}
&\phi(x, y, z) = \\
&+\frac{\sigma}{4\pi\epsilon_0}\sum_{i=1}^{n}(-1)^i\left(\ln\frac{R^2}{(x+id)^2+(z+z_0)^2}+\ln\frac{R^2}{(x-id)^2+(z+z_0)^2}\right)+ \\
&+\frac{\sigma}{4\pi\epsilon_0}\sum_{i=1}^{n}(-1)^i\left(\ln\frac{R^2}{(y+id)^2+(z-z_0)^2}+\ln\frac{R^2}{(y-id)^2+(z-z_0)^2}\right)+ \\
&+\frac{\sigma}{4\pi\epsilon_0}\ln\frac{R^2}{x^2+(z+z_0)^2}+\frac{\sigma}{4\pi\epsilon_0}\ln\frac{R^2}{y^2+(z-z_0)^2}
\end{aligned}$$

Following the same procedure as before, the following relationships are found for the potential minima

$$x_{min} \approx \pm 2m_x d \tag{2.4.1}$$

$$y_{min} \approx \pm 2m_y d \tag{2.4.2}$$

where m_x and m_y are finite integers and $-n \leq m_x, m_y \leq n$. The relationship to find all the minima in z is too complicated to be shown here, instead of this, the relationship at $m = 0$ (at the centre) is presented below.

$$\left.\frac{\partial\phi}{\partial z}\right|_{0,0,0} =$$

$$\sum_{i=1}^{n}(-1)^{i+1}\left(\frac{z_{min}+z_0}{(id)^2+(z_{min}+z_0)^2}+\frac{z_{min}-z_0}{(id)^2+(z_{min}-z_0)^2}\right)-\frac{z_{min}}{z_{min}^2-z_0^2}=0$$

where the minimum at $z_{min} = 0$ is obvious. This equation is an alternating series which converges because of the Leibniz criterion, $a_i > a_{i+1}$ and $\underset{i\to\infty}{lim}(a_i) = 0$ (where a_i is the factor inside the sum $(\sum(-1)^{i+1}a_i)$. The convergence of this series indicates that eventually the minimum in z is mainly influenced by the nearest wires. As before, voltages can be found for each line charge to give the same potential distribution as the analytical calculations.

There are other modifications that can be made to the proposals in this thesis, for example, the addition of extra wires to decrease the higher order term $O(x^4, y^4, z^4, ...)$ in the Taylor expansion (improving the quadratic behaviour of the potential). Another interesting case is when the two sets of wires do not have the same relative values of voltages, when it can be shown that even in the external trapping zones a circular motion can be found (like in the Penning trap). Finally, another scalable design where the interaction between the traps can be neglected is shown in Fig. 2.18.

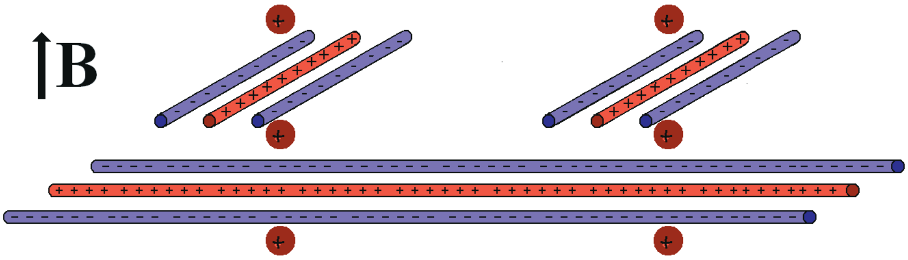

Figure 2.18: Alternative scalable geometry.

3 Novel RF Ion Trap designs

As mentioned in the Introduction, (Section 1), ions traps can be classified in two main groups: Penning and Paul traps. They differ in the way in which the ion confinement is produced. Briefly, Penning traps work with a combination of static electric and magnetic fields. In contrast, Radio Frequency (RF) traps utilize a driving AC electric potential applied to the electrodes. In practice, both designs of traps only require the ability to produce a potential minimum in one of the directions of motion and a symmetric potential in the other two. Electrode configurations that fulfill these two requirements, can create conditions for trapping . In the following sections, based on this statement, it is proved that the planar guide and the wire trap geometries can also be operated as RF traps. The design based on the planar guide retains the nature of linear Paul traps but with a simpler and an even more open geometry. The second design, based on the wire-trap, yields a scalable full three-dimensional confinement with an open geometry. Both designs consist of electrodes made of conducting wires and they can consequently be miniaturized. In addition, a novel configuration that encompasses both designs is also proposed; this architecture is scalable and allows the motion of ions between different traps.

3.1 The Three-wire Linear RF trap

Commonly, RF and Penning traps share a hyperbolic electrode structure [5]. This geometry has a clear advantage over other designs: it is able to produce a highly harmonic quadrupole electric potential. As a consequence, the motions of trapped ions have well-determined frequencies. In contrast, for other designs, like wire, planar and cylindrical traps, [41] [19] [15], it is necessary to approximate their potential to harmonic oscillators or to numerically solve their equations of motion to determine the ion frequencies. However, these designs have properties that balance their lack of an analytical potential by presenting an open or a scalable geometry. Of all the different ion trap geometries available, linear RF traps have received special attention due to their ability to store simultaneously a chain of ions in a linear array. Usually, a linear RF trap consists of four cylindrical electrodes arranged in a square profile (Fig. 1.7). In the trap, two opposite rods are connected to a RF potential while the other pair of rods are connected to the opposite potential or to earth. When the surfaces of the rods are hyperbolic and parallel to the y axis, the two-dimensional potential produced by this setup is

$$\phi(x,z) = -\frac{U - V\cos\Omega t}{2{R_0}^2}(x^2 - z^2) \qquad (3.1.1)$$

where U and V are the DC and AC potential amplitudes respectively, Ω is the angular frequency of the RF signal and R_0 is a parameter that describes the size of the trap [5]. The potential presented in Eq. 3.1.1 leads to a Mathieu equation, the stable solutions of which define the ion motion. Based on the same principles, this section presents the development of an alternative geometry to linear traps.

Linear RF traps present one of the most open geometries of all the types of ion traps as they consist of only four cylindrical electrodes. In contrast, the novel proposal presented below consists of three cylindrical rods placed in the same plane producing an even more open geometry. This proposal is based on the planar guide, its design is schematically shown in Fig. 3.1.

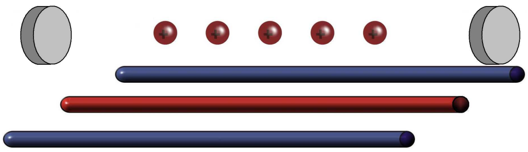

Figure 3.1: Schematic view of the three-wire linear RF trap.

The electric potential generated by the geometry presented in Fig. 3.1, when the three equally-spaced charged lines are placed along x, in $z = 0$, with charge densities $-\sigma$, $+\sigma$ and $-\sigma$, centered at $y = 0$ and each separated by a distance d is determined by

$$\phi = -\frac{\sigma}{4\pi\epsilon_0}\left(\ln\frac{R^2}{(x+d)^2+z^2} - \ln\frac{R^2}{x^2+z^2} + \ln\frac{R^2}{(x-d)^2+z^2}\right)$$

where the charge density can be substituted by voltages by the approximate relationships (developed in Section 2.1)

$$V_- = -\frac{\sigma}{2\pi\epsilon_0}\left(\ln\frac{R}{a} - \ln\frac{R}{d} + \ln\frac{R}{2d}\right) = -\frac{\sigma}{2\pi\epsilon_0}\ln\frac{R}{2a} \tag{3.1.2}$$

and

$$V_+ = -\frac{\sigma}{2\pi\epsilon_0}\left(\ln\frac{R}{d} - \ln\frac{R}{a} + \ln\frac{R}{d}\right) = -\frac{\sigma}{2\pi\epsilon_0}\ln\frac{Ra}{d^2} \tag{3.1.3}$$

where a is the radius of the wire, as long as $a \ll d$. Combining Eqns. 3.1.2 and 3.1.3, the potential difference ($\triangle V$) is

$$\begin{aligned}\triangle V = V_+ - V_- &= -\frac{\sigma}{2\pi\epsilon_0}\left(\ln\frac{Ra}{d^2} - \ln\frac{R}{2a}\right) = \\ &= \frac{\sigma}{2\pi\epsilon_0}\ln\left(\frac{d^2}{2a^2}\right)\end{aligned} \tag{3.1.4}$$

which provides the relationship between the charge densities and the potential difference in the wires. Following this calculation, the electric potential of the wire RF geometry, in cartesian coordinates, can be expressed as

$$\phi(x,z) = -\frac{\triangle V}{2\ln(d^2/2a^2)}\left(\ln\frac{R^2}{(x+d)^2+z^2} - \ln\frac{R^2}{x^2+z^2} + \ln\frac{R^2}{(x-d)^2+z^2}\right)$$

where d is the distance between wires, a the radius of the wires, R is an arbitrary distance to the electrical ground and $\triangle V$ the potential difference between the wires [44] [41]. As mentioned in Section 1.3.2, the electric potential close to the trapping volume can be approximated to a quadrupole potential by a second order Taylor expansion around the trapping points. Following this statement, the potential close to the trapping region, $z = \pm d$, becomes

$$\phi(x,z) = \frac{\triangle V}{\ln(d^2/2a^2)}\left(\ln\frac{2d}{R} - \frac{x^2}{d^2} + \frac{(z\pm d)^2}{d^2}\right). \tag{3.1.5}$$

Furthermore, if the potential difference applied to the electrodes has a DC as well as an AC component, then Eq. 3.1.5 takes the form:

$$\phi(x,z) = \frac{U - V\cos\Omega t}{\ln(d^2/2a^2)}\left(\ln\frac{2d}{R} - \frac{x^2}{d^2} + \frac{(z\pm d)^2}{d^2}\right). \tag{3.1.6}$$

The equations of motion for a charged particle under the potential described in Eq. 3.1.6 lead to three uncoupled expressions:

$$\frac{\partial^2 x}{\partial t^2} = \frac{2q}{md^2 \ln(d/\sqrt{2}a)}(U - V\cos\Omega t)x \tag{3.1.7}$$

$$\frac{\partial^2 y}{\partial t^2} = 0 \tag{3.1.8}$$

$$\frac{\partial^2 z'}{\partial t^2} = -\frac{2q}{md^2 \ln(d/\sqrt{2}a)}(U - V\cos\Omega t)z' \tag{3.1.9}$$

where q and m are the charge and the mass of the particle and $z' = z \pm d$. As no force is acting along y, a charged particle would have a constant velocity in this direction. On the other hand, the motion in the xz plane will be given by stable solutions of Eqns. 3.1.7 and 3.1.9, both being Mathieu equations. These equations can be written in their canonical form as

$$\frac{\partial^2 x}{\partial \zeta^2} - (a' - 2q'\cos 2\zeta)x = 0 \tag{3.1.10}$$

and

$$\frac{\partial^2 z'}{\partial \zeta^2} + (a' - 2q'\cos 2\zeta)z' = 0 \tag{3.1.11}$$

where

$$a' = \frac{8qU}{md^2 \ln(d/\sqrt{2}a)\Omega^2} \tag{3.1.12}$$

$$q' = -\frac{4qV}{md^2 \ln(d/\sqrt{2}a)\Omega^2} \tag{3.1.13}$$

and $\zeta = \frac{\Omega t}{2}$. In this general form, these equations have characteristic regions where the final motion is stable (spatially bounded). Finally, the two-dimensional stability diagram is produced when both x and y stability diagrams are superimposed on each other. Then, the xz-motion is bounded when the motion along both axes are simultaneously stable [5]. There are many ways to find the stability region of the Mathieu equation, for example, in Fig. 3.2 stable points have been calculated for Eq. 3.1.10 using a Sträng's recursion algorithm [9] for a ^{40}Ca$^+$ ion in a trap where the wires are separated by 3 mm. The stability diagram for the canonical Mathieu equations, dependent on a' and q', was presented in Section 1.2.2.

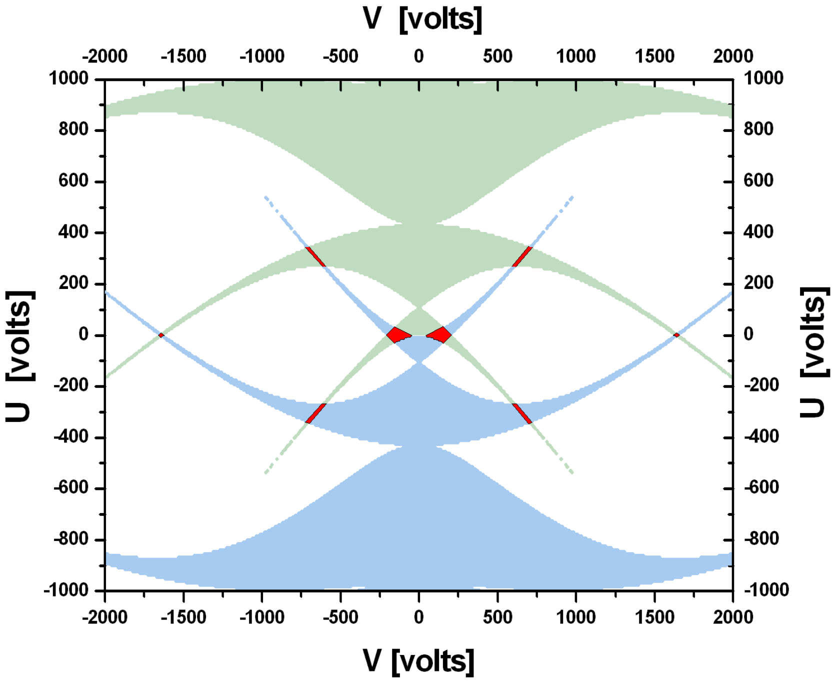

Figure 3.2: Stability regions for the x and z Mathieu equations. The x stable region is presented blue-shaded and the z stable region is shown green-shaded. The red-shaded regions represent conditions where both simultaneously x and z motions are stable for a $^{40}\mathrm{Ca}^+$ ion in a trap with $d = 3$ mm and RF drive of 2 MHz.

The general stability diagram depends on the values of the parameters a' and q', and so on the mass of the ion. This characteristic has been used as a mass selector in linear Paul traps and would be also applicable to this configuration.

As in linear Paul traps, the three-dimensional confinement in these traps would be achieved by the addition of electrodes at both ends of the linear array; these extra electrodes are schematically presented in grey in Fig. 3.1. By the addition of these electrodes, the confinement of ions would be produced all along the path of the electrodes and the inter-ion spacing would be determined by ion-potential and ion-ion interactions producing a string of ions in a three dimensional confinement as in the traditional linear RF trap, [13].

3.2 The six wire RF trap

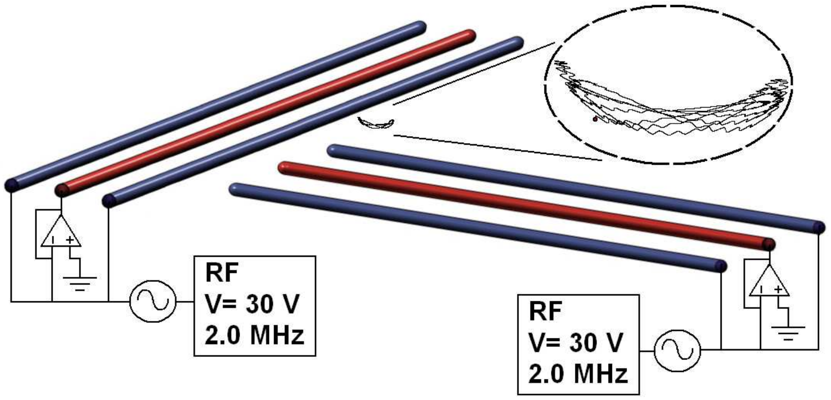

Figure 3.3: Wire trap design for an ion trap. The simulation of the motion of a $^{40}\mathrm{Ca}^{+}$ ion was perform using SIMION. Ion kinetic energy $=1 \times 10^{-2}$ eV, V=30 V, $\Omega/2\pi = 2$ MHz, U=0. The diameter of the wires (a) is = 1 mm, wires are separated (d) by 3 mm and the sets of wires are separated by 4 mm in the axial direction ($2z_0$).

Linear Paul traps have offered a good framework for quantum computing experiments because they can produce a string of ions. In contrast, a two-dimensional array of ion traps can be implemented using a configuration similar to the three-wire linear RF trap. This trap design is made using two perpendicular linear RF traps placed at different planes: this would be a RF version of the Penning wire-trap [41]. A schematic view of this trap is shown in Fig. 3.3.

This trap, a six-wire RF trap, provides a better scalability together with an open geometry. Depending on the dimensions chosen, this design is able to have three or four trapping points, one above, up to two in the middle and one below the wires (in Fig.3.3 the simulation shows a Ca^{+} ion trapped in the middle trapping point). For simplicity, in this work only the case of the central confinement is studied. As a result, an approximate quadratic RF potential in the middle point $x = 0$, $y = 0$, $z = 0$ can be expressed as

$$\phi(r,z) = \frac{U - V\cos\Omega t}{{R_0}^2}(\xi - r^2 + 2z^2) \tag{3.2.1}$$

where $\xi = -2R_0 \ln \frac{Rz_0}{d^2+z_0^2}$ and R_0 can be understood as an effective trap parameter defined as

$$\frac{1}{R_0^2} = \frac{1}{\ln d^2/2a^2}\left(\frac{2}{d^2+z_0^2} + \frac{1}{z_0^2} - \frac{4z_0^2}{(d^2+z_0^2)^2}\right) \tag{3.2.2}$$

where d is the separation between wires in a single set and $2z_0$ is the separation between sets. Following the same procedure as before, the equations of motion of the ion are

$$\ddot{r} - \frac{2q}{mR_0^2}(U - V\cos\Omega t)r = 0 \tag{3.2.3}$$

and

$$\ddot{z} + \frac{4q}{mR_0^2}(U - V\cos\Omega t)z = 0 \tag{3.2.4}$$

which can be recognized again as Mathieu differential equations. In their canonical form these equations are written as

$$\frac{\partial^2 r}{\partial\zeta^2} + (a'_r - 2q'_r\cos 2\zeta)r = 0 \tag{3.2.5}$$

and

$$\frac{\partial^2 z'}{\partial\zeta^2} + (a'_z - 2q'_z\cos 2\zeta)z' = 0 \tag{3.2.6}$$

where

$$a'_r = \frac{8qU}{mR_0^2\Omega^2} \qquad a'_z = -2a_r \tag{3.2.7}$$

$$q'_r = \frac{4qV}{mR_0^2\Omega^2} \qquad q'_z = -2q_r \tag{3.2.8}$$

and $\zeta = \frac{\Omega t}{2}$. Stable solutions for Eqn. 3.2.3 and 3.2.4 correspond to bounded trajectories where the ion is confined radially and axially. In Fig. 3.4 an example of the stability diagram is shown for a $^{40}\mathrm{Ca}^+$ trap with $a = 0.5$ mm $d = 3$ mm, $z_0 = 2$ mm and $\Omega = 2$ MHz.

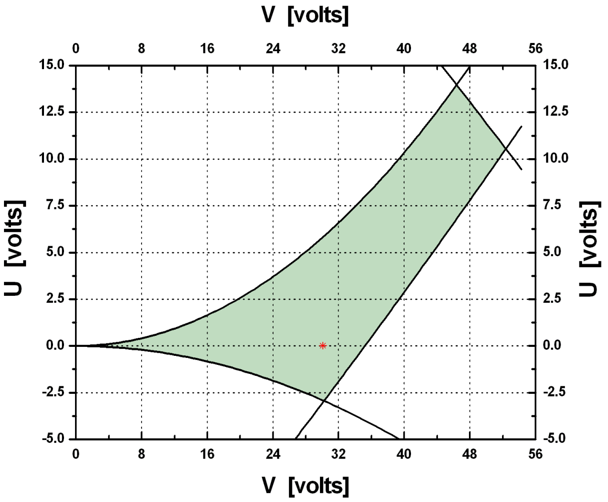

Figure 3.4: Stability diagram for a $^{40}\mathrm{Ca}^{+}$ three-wires linear RF trap, wires have 1 mm diameter, sets of wires are 4 mm apart, wires are 3 mm apart within a set, and the RF driver has a frequency of 2 MHz. The red star marks the values used in Fig. 3.3.

At this point, the theoretical development of some novel geometry designs for ion traps has been presented. Calculations and simulations were carried out to demonstrate that these geometries can be run as Penning traps and also as RF traps. In addition, the most important characteristics and properties of these designs have been explained and supported with simulations or/and calculations. However, one important element has been missing: the experimental realization of these traps. In the next section, the design, construction and testing of a wire trap prototype is presented together with some experimental results. This prototype provides a good starting point for many more experiments that could and will be carried out in the further development of some of the ideas presented in the previous sections.

4 The wire trap prototype

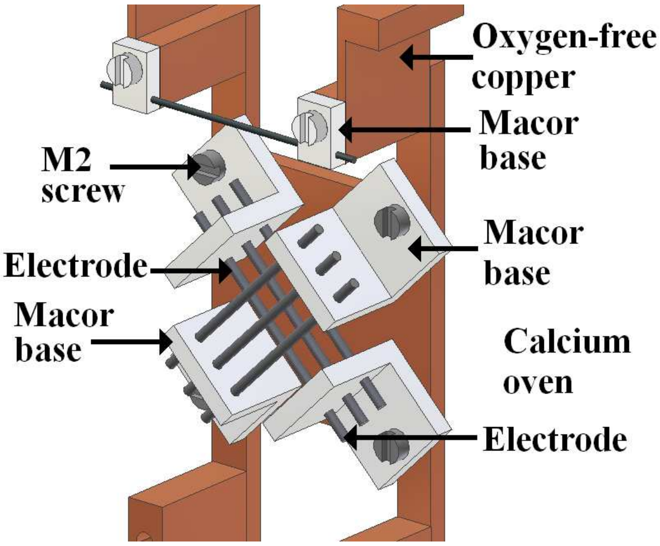

Figure 4.1: Schematic view of the prototype wire trap.

In order to experimentally demonstrate the viability of the wire trap, a prototype of this trap was designed, built and tested at Imperial College. The prototype was developed to run as a Penning trap with an electronic detection circuit connected to its electrodes. As the design of the wire trap allows good optical access to the trapped ions, this prototype was designed in such a way that it also allows the possibility of optical detection experiments. The design can be modified to permit the access of lasers and the recording of fluorescence from the trapped ions. A schematic view of the trap is shown in Fig. 4.1.

The prototype was intentionally designed to trap calcium and molecular nitrogen ions at the centre of a six-wire Penning trap. In addition, the prototype was designed to fit inside ultra-high-vacuum components and systems that were already available in the Ion Trapping group. Many factors were considered before the construction of the trap was carried out; the prototype was built based on two three-dimensional computer-prototypes that were created to assure a straightforward construction and operation. The first computer prototype was carried out in a three-dimensional design software to guarantee a good fit of all the components (Inventor 11.0). The second digital prototype was made in SIMION to simulate the motion of the ions taking in account the actual dimensions of the electrodes and the magnetic and electric fields that can be produced in the laboratory. When these two digital prototypes were successfully tested, the construction of the trap was then carried out. All the considerations made during the construction of the prototypes (digital and real) are explained in the next section. Some of the experimental results of the trap prototype can be found in [44].

4.1 Experimental setup

A three dimensional sketch of the wire trap prototype is shown in Fig. 4.2; this computational model was drawn in Inventor 11.0. Basically, the trap consists of the two sets of wire electrodes, a calcium oven, a filament and their mounts. As mentioned in the last section, before the design and construction of the trap prototype was carried out, some material was already available in the Ion Trapping Group at Imperial College. Two of these pieces of equipment played a fundamental role in the design of the trap, as they influenced directly the dimensions of the prototype. These elements were the electromagnet and the existing vacuum pumps. In combination, both elements forced the prototype trap to fit into standard DN40 CF vacuum components. The internal diameter of these components was critical for the design of the trap as it determines the separation of the electromagnet pole pieces and consequently the amplitude and quality of the magnetic field. DN40 CF ultra-high-vacuum (UHV) tubes with an internal diameter of 38 to 40 mm were chosen because at such distances well-characterized calibration curves are available for the electromagnet used (water cooled Oxford Instrument 4" Electromagnet Model SCT-200-15) [45]. During the testing of the trap prototype, and according to measurements made with a gaussmeter, and in agreement with the magnet calibration, magnetic fields of up to 1 tesla were generated with a 10 amps current flowing through the electromagnet coils.

Another important element that influenced the design of the prototype

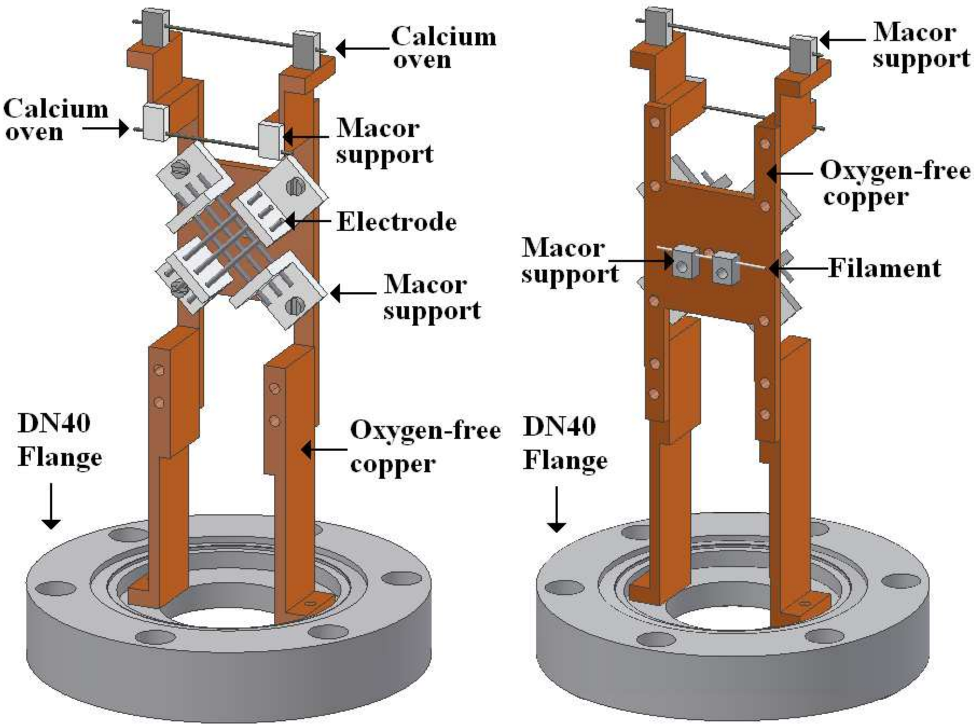

Figure 4.2: A three dimensional model of the wire trap prototype. Design created with Inventor (Autodesk).

was the electronic detection setup. This setup consists of a resonant circuit coupled to a signal amplifier and an AC/DC converter circuit. Basically, the resonant part of the circuit consists only of a 60-turns coil, making the setup almost non-tuneable as the impedance of the system was fixed once the trap was constructed and connected. The only way to slightly adjust the resonant frequency in this setup was by changing the length of the BNC cables after the UHV feedthrough or by adding a capacitor to the resonant circuit. Many different ways to achieve a tuneable resonant circuit exist (an easy way to achieve a tuneable resonant frequency is simply by coupling a variable capacitor to the coil), however it was decided to keep the detection setup unchanged as it is a very reliable design, (this setup has worked unchanged for 10 years [46]). Originally, this electronic detection setup was constructed and later refined to test a hyperbolic Penning trap. In the original setup, both endcaps of the hyperbolic trap were connected to the electronic detection circuit, whereas the ring was connected to a scanning voltage power supply; Fig. 4.3 shows a diagram of this setup. In contrast, in the wire trap prototype, the central wires played the role of the endcaps and the exterior wires replaced the ring electrode; Fig. 4.3 presents a diagram of these connections. As mentioned previously, the motion of the trapped ions inside a Penning trap can be described as a combination of three oscillatory motions. The frequencies of these motions depend on the electric potential difference between the ring and the endcaps, and the physical dimensions of the trap. As the electronic detection setup was constructed to test a hyperbolic trap (with $z_0 = 3.5$ mm and $r_0 = 5$ mm), similar dimensions for the wire trap prototype were chosen to produce oscillation frequencies in a similar range

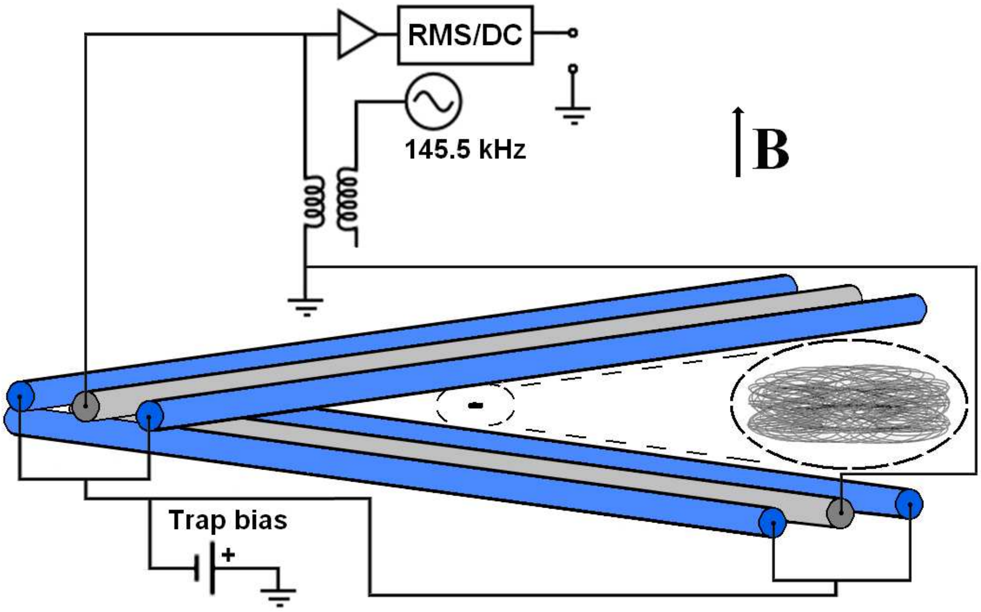

Figure 4.3: Schematic view of the experimental setup for the electronic detection scheme. The simulated trapped ion trajectory shown in the figure corresponds to Ca^+ at 1×10^{-2} eV in a trap with similar dimension to those of the prototype, the potential difference between central and external wires is $\triangle V = -1.3$ V (at this voltage, the axial frequency of ions corresponds to the resonant frequency of the detection circuit). The magnetic field of 1 T is oriented perpendicular to both set of wires. Simulation made in SIMION.

to the original design. In this way, it was expected that the trapped ions would be easily detected by the existing setup. This consideration was not trivial, as the dimensions of wire traps and hyperbolic traps are not straight forwardly comparable. Consequently, the final dimensions of the trap were decided through the use of computer simulations. These simulations were performed in SIMION in order to determine the trapping potential depth produced by different trap configurations. Several simulations were done until a complete system was created; the final simulation included the vacuum chamber, the metallic supports, all the electrodes and a magnetic field. In Fig. 4.4 a snapshot of the final SIMION project is presented. The simulation corresponds to a $^{40}\mathrm{Ca}^{+}$ ion with kinetic energy of 1×10^{-1} eV in a wire Penning trap with the physical dimensions of the prototype; in this simulation the central wires are connected to 0 V, exterior wires are connected to -2.5 V, the supporting base and the vacuum chamber are electrically grounded and the magnetic field of 1 T is perpendicular to the supporting base. Additionally, in Fig. 4.3, the same SIMION project was used to simulate the flight of a $^{+}\mathrm{Ca}^{40}$ ion but under different trapping conditions (central wires are grounded and external wires are connected to -1.3 V).

After all these considerations were taken in account, Inventor was used to create a three-dimensional model of the prototype. The program Inventor from Autodesk was chosen because it is capable of producing, manipulating and bringing together individual components. This property was very useful as different components could be designed and modified to achieve a better fit or better component connection. The basic layout of the prototype consists of the trap electrodes, two calcium ovens, a filament and the electrical connections from all these elements to the electrical feedthrough. In total, the prototype contains eight or ten connection lines: one for the upper central wire, one for the lower central wire, a common connection to the upper external wires, a common connection to the lower external wires, two connections to the filament, and two or four connections to one or two ovens respectively. Two sets of three stainless-steel cylindrical rods of 1 mm diameter and approximatively 35 mm long were used as electrodes, as shown in Figs. 4.2, 4.4 and 4.5. The length of the electrodes was determined by

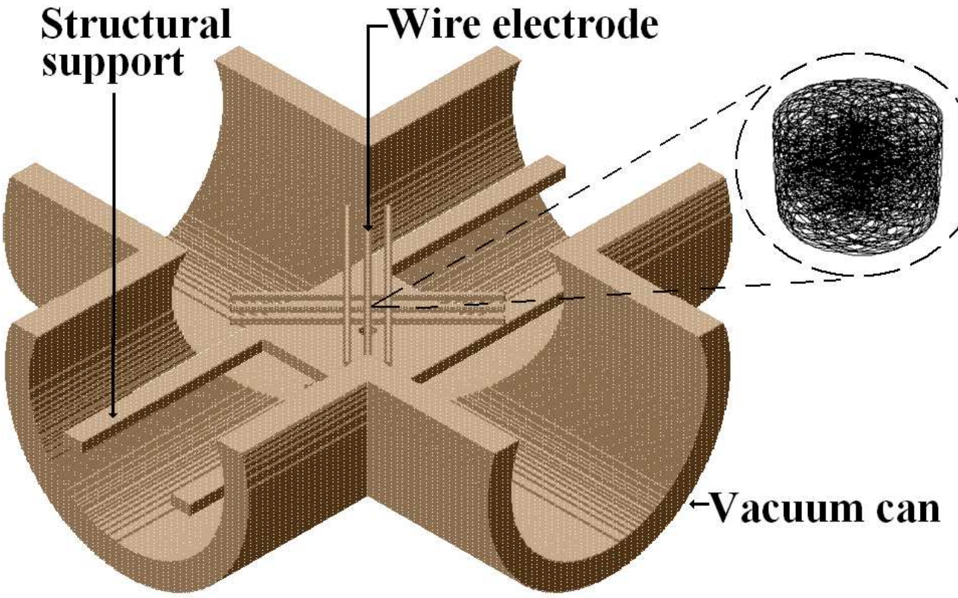

Figure 4.4: Simulation of the flight of a $^{+}\mathrm{Ca}^{40}$ ion in a wire Penning trap. This simulation corresponds in a perfect scale to the trap prototype that was later constructed. External wires are connected to -2.5 volts, and the central wires, the supporting plate and the four-way cross are electrically grounded (0 volts).

the size of the vacuum housing, and their diameter and separation were determined by the machining specifications of Macor. In fact, these rods were chosen because 1 mm holes are easily machinable in ceramic materials and because stainless-steel is UHV compatible. In order to maximize the length of the wires, or minimize the effect of finite electrodes, different configurations were produced in Inventor. Finally, L-shape mounts were designed and made of Macor to support and fix the electrodes in predetermined positions. The wire electrodes and their mounts are shown in detail in Fig. 4.5.

The design of L-shape mounts proved to be very practical, as they were easy to machine and align. In addition, the shape of the mounts saved some space because the electrode connections could be accommodated on the back of them. These mounts were built of Macor, which is a highly machinable ceramic compound that is ultra high vacuum compatible. The technical drawing for the mounts is presented in Fig. 8.2 in the Appendix.

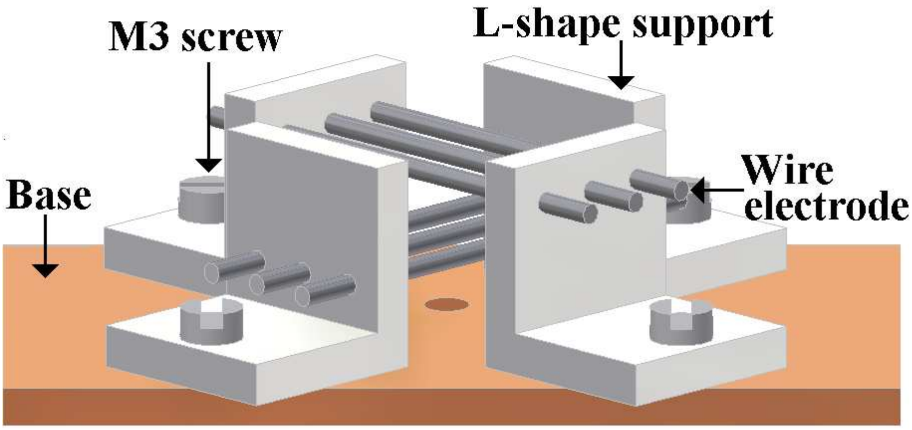

Figure 4.5: Supports made of Macor were chosen to hold the wire electrodes. The L-shape of the supports allows the optical access, saves space for the electrode connectors and is easily machinable.

Within a set, wire electrodes are separated by $d = 3$ mm and sets are $2z_0 = 4$ mm apart in the axial direction. The ceramic mounts were fixed onto an oxygen-free copper base which provides a general support for all the other components but also shields the six-wire configuration from the electric fields produced by a filament and its connectors placed underneath. The base has a thickness of 2 mm, and contains 10 M2 threaded holes to provide mounting points for other elements. In addition, a 2 mm hole at the centre of the base was drilled to permit the access of electrons from the filament placed behind it; the technical drawing is presented in Fig. 8.2. The electron gun (a coiled thoriated tungsten filament) was placed behind the base and fixed by $5 \times 3 \times 2$ mm Macor supports, Fig. 4.2.

The prototype was designed in such a way that the centre of the trap was placed at the three-dimensional centre of a four way cross vacuum chamber. In this configuration, one arm of the chamber was used to provide the electrical connections, in a second arm a viewport was placed to monitor the ovens and the filament, in the third arm a leak valve was fitted for the injection of nitrogen gas, and the last arm was used to connect the system to the vacuum pumps and the pressure gauges. A schematic view of the vacuum chamber configuration is presented in Fig. 4.6. The base plate was firmly fixed to the

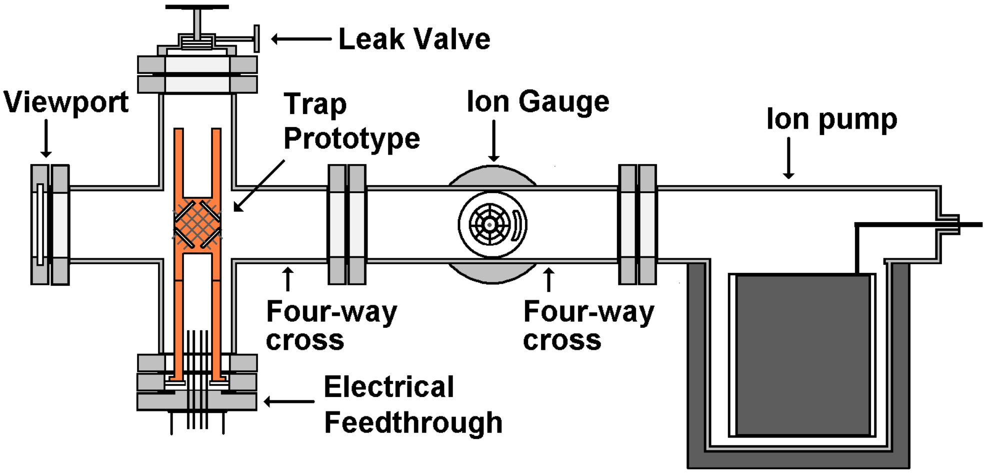

Figure 4.6: Schematic view of the vacuum chamber. The second four-way cross has a line perpendicular to the plane of the page, the rotary and sorption pumps (or a turbo-molecular pump) were connected here.

vacuum chamber through two pedestals made of oxygen-free copper. The length and depth of the pedestals were arranged to place the centre of the trap at the centre of the four way cross, the width of the pedestals was chosen to provide enough space for the connections to the feedthrough. Two M2 threaded holes were located at the top of the pedestals to support one calcium oven (atomic oven, not shown in figure). In addition, two smaller pedestals were designed and built to provide a base for two other atomic ovens on the top of the prototype. The dimensions of both pedestals are presented in Fig. 8.3 in the Appendix.

To support all the trap components, a special DN40 CF flange was designed and made of stainless steel, Fig. 8.4 in the Appendix. The profile of this flange contains a 7.5 mm track with four M3 threaded holes to fix the lower trap pedestals at the right position to locate the centre of the trap at the center of the flange and consequently at the center of the vacuum chamber. Additionally, the flange contains copper gasket supports at both ends to connect the system to the vacuum chamber and to the electrical feedtrough.

The complete view of the prototype, including the filament and the atomic ovens, is presented in Fig. 4.2. The filament and both ovens were supported by 5 × 3 × 2 mm Macor supports. The base plate and the pedestals were electrically connected to earth. In addition, some ceramic washers were used around the connectors to prevent electrical contact between the ovens, filaments and the vacuum chamber.

When the prototype design was complete, its construction was carried out by Mr. Brian R. Willey in the Blackett Laboratory workshop. The parts of the prototype were assembled in the Ion Trapping Laboratory at Imperial College. The operation of this prototype is explained in the following section.

4.2 Operation of the prototype and experimental results

As mentioned before, the prototype trap was designed to work with calcium and molecular nitrogen ions. In the prototype, calcium atoms were generated by atomic ovens and molecular nitrogen gas was injected into the vacuum chamber using a leak valve. Both atomic species are ionized by electron bombardment to produce Ca^+ or N_2^+. Generally, in an atomic oven, the required element (calcium in this case) is placed inside a metallic chamber that is connected to an electric current supply. To produce Ca atoms, a high electric current ($\approx$ 1.5 A) is sent to heat the chamber by electrical resistance. When the chamber is heated, the material inside the chamber is evaporated and the resulting vapour is ejected from the chamber in the desired direction. Atomic ovens are widely used to evaporate metals because they can be well-characterized to provide small numbers of atoms, are easy to make and easily to align, [7]. The injection of a gas into the trap is much simpler as the amount of atoms or molecules is simply controlled by the gas regulator and a leak valve. While the trap was operating, the nitrogen gas was injected through the leak valve up to a pressure of 1×10^{-7} mbar.

The atomic ovens of the prototype were made of a 1 mm diameter tantalum tube[1] spot-welded onto a 0.25 mm tantalum wire[2]. Granular calcium was placed inside the tantalum tube and then both ends of the tube were crimped closed. A hole ($\approx$ 0.2 mm diameter) on the side of the tube allows the exit of atoms when the oven is heated by an electrical current sent through the tantalum wire. The filament, which produces the electron bombardment, was made of a coiled thoriated tungsten wire[3] with a diameter of 0.25 mm. Thoriated tungsten filaments are often used in electron bombardment experiments as they produce electronic emissions many times that of pure tungsten filaments at similar temperatures [47]. In the trap, ovens and filaments were connected to the electrical feedthrough by Kapton wires [4] and stainless-steel barrel connectors with a 3 mm diameter. Typically, the

---

[1] Goodfellow 713-389-90

[2] Advent TA550515

[3] Goodfellow W-145400

[4] Kapton wire is a UHV compatible wire that is electrically insulated by a film of

calcium ovens were operated at 1.53 amps and the filament at 4.4 amps with a DC bias of -30 V.

During the assembly of the prototype, care was taken to ensure a good ultra high vacuum (UHV) compatibility. As previously indicated, the prototype trap components were made of only four UHV compatible materials: Macor, alumina, oxygen free copper and stainless-steel. Kapton wires and stainless-steel barrel connectors were used to electrically connect the components. Before the assembly of the prototype was carried out, all the ceramic components were cleaned in an ultrasonic bath with a solution of detergent and water for 4 minutes at 50 Celsius. Oxygen free copper components were cleaned with Copper-brite[5] for 1 minute, then washed with distilled water and finally cleaned in the ultrasonic bath with ethanol for 4 minutes at 40 Celsius. Stainless-steel components were cleaned in the ultrasonic bath with acetone for 4 minutes at environmental temperature (25 Celsius). Kapton wires, ovens and filaments were only superficially cleaned with ethanol.

After being cleaned, the trap was assembled and placed inside its vacuum chamber. Then, the setup was pumped out by a chain of pumps to 2.5 $\times 10^{-8}$ mbar. From atmospheric pressure, the trap was pumped out by a rotary pump (AEGTyp ADEB63K2R0) to 1×10^{-3} mbar. This process took approximatively 25 minutes. An sorption pump (Vacuum Generators) was then used to pump out the trap to $2-3 \times 10^{-5}$ mbar in approximatively 20 minutes. Finally, an ion pump (Meca 2000) pumped out the remaining background gas to a pressure of around 2.5×10^{-8} mbar in around 48 hours. Once the assembling and evacuation of the trap were complete, all the connections were individually tested. Electrical conductivity was measured between the connectors of the ovens, the filament and the vacuum chamber (electric ground). These simple tests confirmed which connections were operative. In fact, the vacuum chamber had to be opened three times because a short circuit was found between the filament and the vacuum chamber. It was found that when the filament was heated its ends were deformed in such

---

polyamide. Kapton wires with diameter of 1 mm can carry electrical currents up to 5 amperes.

[5] Copper-brite is the commercial name of a metal cleaner solution containing a mixture of acids: 75% HNO_3, 23% H_2SO_4 and 2% HCl.

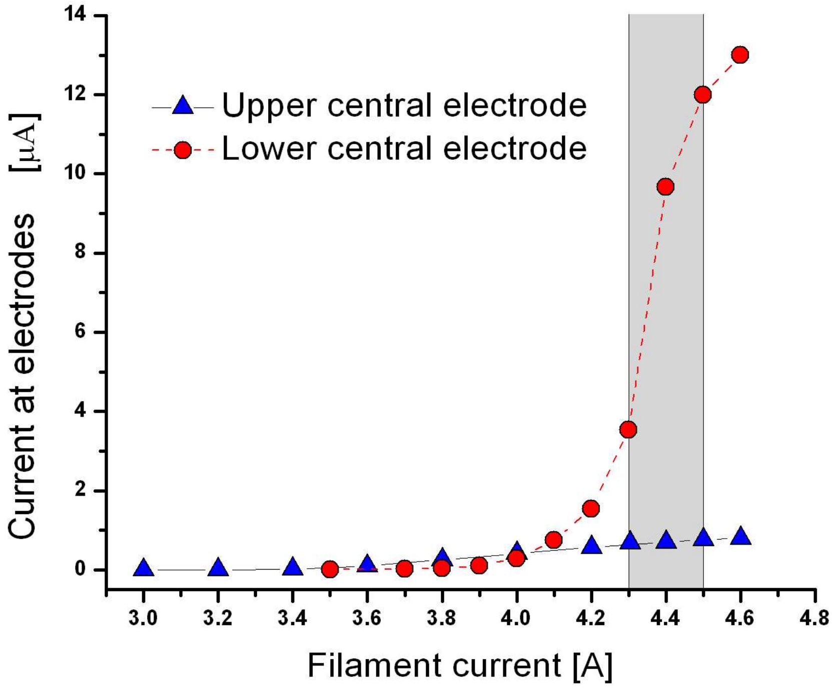

Figure 4.7: Filament electronic emission at different electrodes. Results with a magnetic field of 1 T. In shadow, the operational range of the filament during the electronic detection experiments. The separation between the filaments is of 4 mm.

a way they became in electric contact either with the vacuum chamber or with the trap base. This problem was permanently solved by surrounding the filament connectors with ceramic cylinders (Macor). On the other hand, the connections from the electrical feedthrough to the trap electrodes were tested by running the filament and detecting the electronic emission to the electrodes.

The emission of electrons was monitored by measuring the voltage across a 1 MΩ resistor connected between the chosen electrode and the electrically biased filament. The same procedure was carried out on all the electrodes as this provided an insight into the number of electrons that entered the trapping volume (the space between the central wires). During the operation of the trap, the filament was biased to -28 V to achieve the ionization of Ca atoms and to -30 V for N_2 molecules. The characterization curve for the filament electronic emission is presented in Fig. 4.7; these results correspond to a -30 V biased filament in the presence of a 1 T magnetic field perpendicular to the trap base. During the electronic detection experiments, the filament was typically run in the range of -4.3 to -4.5 A.

As previously explained, during the electronic detection experiments, the central wire electrodes were connected to the resonant circuit whereas the exterior wire electrodes were connected to a scanning DC power supply. A schematic diagram of these connections was presented in Fig. 4.3. The circuit formed by the central wires and the electronic detection setup had a resonant frequency of 145.5 kHz, a value that was very similar to the frequency found in the original setup consisting of the same detection circuits but with a hyperbolic trap (148.0 kHz). Furthermore, during the testing of the prototype trap, this hyperbolic trap was often used to check the smooth functioning of the electronic detection system (an example of a measurement performed with the electronic detection scheme in the hyperbolic trap was presented in Fig. 1.20, in Section 1.5.1). For the detection, a 10 mV_{p-p} drive was coupled to the central wires to excite the motion of the trapped ions whereas the external wires were scanned in the range from -4.0 to -0.0 volts; the circuit diagram is presented in Fig. 4.3. During this process, the motional frequency of the ions changed until it matched the resonant frequency of the detection circuit. At this point, the ions absorb energy from the drive and this is detected as a dip in the output signal at a particular value of the electronic detection circuit.

Some simulations were carried out to determine the axial frequency of the trapped ions in terms of the electric potential applied to the external wires (or trap bias as central wires are grounded). The SIMION project described in Section 4.1 (Fig. 4.4) was used to obtain the electric axial potential between the central wires at different trap biases. Two axial electric potentials, trap biases of -2 V and -8 V, are presented in Fig. 4.8. From these data, quadratic functions were fitted to obtain the harmonic trapping potential and finally the axial frequency for $^{40}Ca^+$ and N_2^+ (molecular mass of 20 amu). Quadratic term coefficients for trap biases ranging from -10 to 0 volts are shown in Fig. 4.9. After the quadratic coefficients were calculated, a simple analysis was performed to obtain the axial frequency in terms of the mass of the ion

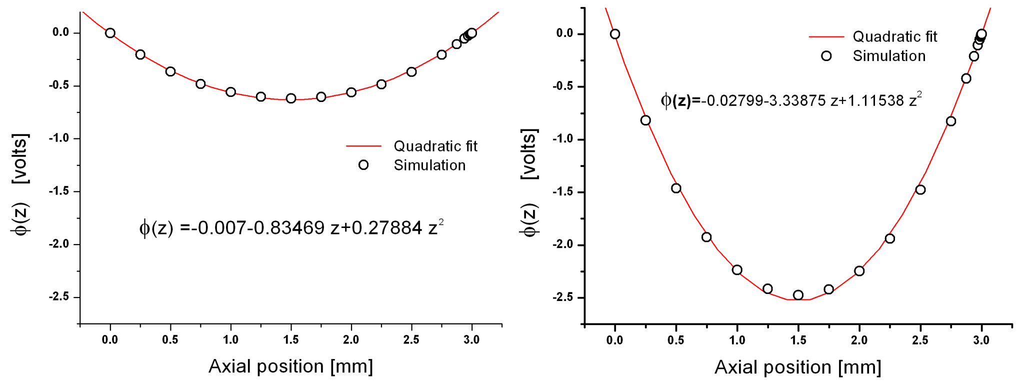

a) **b)**

Figure 4.8: Axial electric potential for two different trap biases. In both cases both central wires were electrically grounded, in a) exterior wire electrodes were connected to -2 V, and in b) exterior wire electrodes were connected to -8 V. Simulations using SIMION.

species. This is essentially a mass spectroscopy analysis. The quadratic coefficients (a) are directly related to the field as

$$E(z) = 2az \tag{4.2.1}$$

Consequently, a particle with charge q and mass m under the influence of this field, would feel a force F of the form

$$F = m\frac{\partial^2 z}{\partial t^2} = qE(z) = 2qaz \tag{4.2.2}$$

that leads to a harmonic oscillatory motion

$$\frac{\partial^2 z}{\partial t^2} = \frac{2qa}{m}z \tag{4.2.3}$$

which frequency (ν_z) is determined by

$$\nu_z = \frac{1}{2\pi}\sqrt{\frac{2qa}{m}} \tag{4.2.4}$$

The axial frequencies in terms of the species mass are obtained by com-

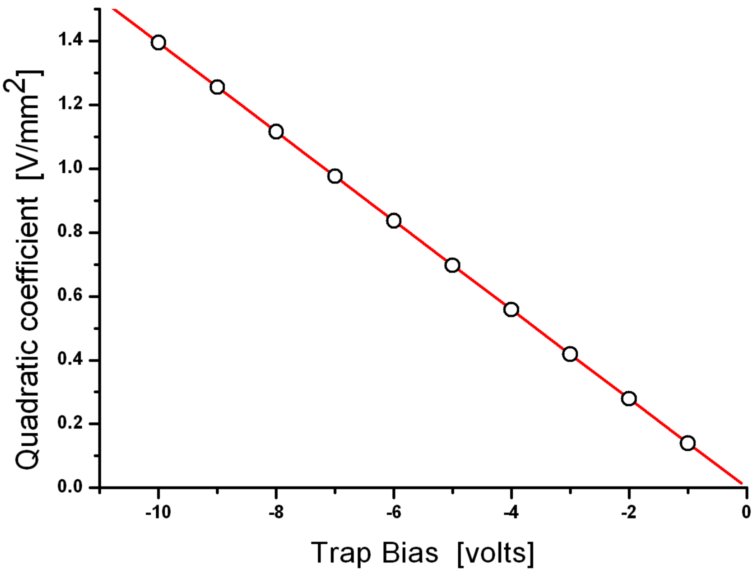

Figure 4.9: Quadratic coefficient for different trap biases. Each coefficient was individually calculated by fitting a quadratic curve to the axial potential generated by the corresponding bias in SIMION.

bining this relationship with the results shown in Fig. 4.9 and with the physical properties (charge and mass) of the ionized species (Ca and N_2 in this case). The results are shown in Fig. 4.10. During the experiments, these results were use to find the operating range of the prototype, as they show that for $^{40}Ca^+$ the 145.5 kHz resonance is expected at approximately -1.3 V and for N_2^+ at -0.9 V. In addition, according to the condition of stability ($\omega_c^2 > 2\omega_z^2$), the trap bias scan could be narrowed to operate between 0 and -4 volts for $^{40}Ca^+$ and to 0 to -6 volts to N_2^+. The stability region condition is determined by the magnetic field applied to the trap (1 Tesla in this case, $\omega_c = qB/m$): for $^{40}Ca^+$ the critical axial frequency is at 281 kHz and for $^{28}N_2^+$ is at 401 kHz.

After all the previous calculations and simulations were carried out, the prototype was fully characterized; the scanning range was determined, the stability region was known and the axial and magnetron frequencies were established. With this information and the prototype construction finished, the experiments were performed in the Ion Trapping Laboratory at Imperial College during 2006.

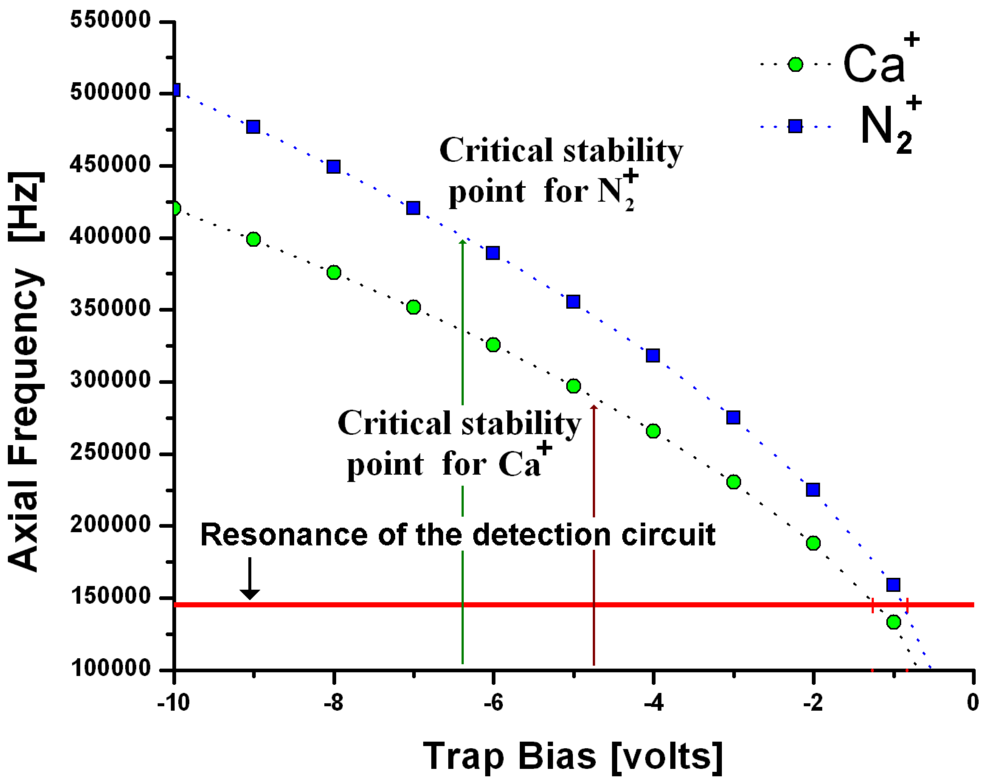

Figure 4.10: Axial frequency in terms of the trap bias for two different ion species. In red, the resonant frequency of the electronic detection setup. Axial frequencies higher than the critical frequency produce unstable ion motions.

The operation of the prototype trap can be summarized in three steps: the activation of the magnetic field, the firing of the filament and the heating of the atomic oven. Every step is easily identified in the output of the electronic detection setup. The first step takes approximatively 45 mins as the electromagnet used during the experiments has a warm-up time of 30 minutes. This warming up time was usually used to prepare the detection circuitry. In this process the amplifiers that are part of the electronic detection setup were turned on and their output was connected to a computer interface for the data acquisition. As no charges are present in the trap during this process, a flat response on the output of the detection setup is observed all the time.

During the second step (the firing of the filament), as electrons are being produced, a drop in the signal is observed. This drop is produced by the collision of electrons onto the central wires (or onto the endcaps in the hyperbolic trap). This process is very important because it can be used to verify a good alignment of the filament and also to check the presence of the scanning potential in the external electrodes (or the ring in the hyperbolic trap). An aligned filament made of the right material produces a large number of electrons and, as a result, a larger drop of the signal. In the prototype, two filament materials were tested: tungsten and thoriated tungsten. Under the same operating conditions, the thoriated tungsten filaments produced signal drops four times larger than the ones obtained with tungsten wires. As a consequence, only thoriated tungsten filaments were used during the test of the prototype. In some experiments, usually after running the filament with a current above 4.5 A, the signal drop faded away without an apparent explanation. When the trap was opened and analyzed, it was discovered that the filament was deformed by heating effects due to the high temperatures created by the high electric current. In the prototype, the filament was fixed in such a way it was located behind a plate with a 2 mm hole to protect the trap from the electric field generated by it (this was explained in Section 4.1). The hole in the plate was aligned with the centre of the trap to permit the transit of electrons from the filament to the trapping region. A deformed filament usually suffered a displacement from its original position missing its original alignment and blocking the flow of electrons towards the central wires. This problem was solved by tightening the coils during the production of the filaments and by limiting the current in the filament up to 4.5 A (the filaments were made by coiling a 0.25 mm thoriated tungsten wire, this was explained in Section 4.1). While the filament was operating, the shape of the electronic detection output signal was also used to indicate whether or not the potential in the external electrodes (or the ring) was being scanned. When the potential on the wires was being scanned from zero to negative voltages, the electrons were repelled outside the trapping region and consequently less electrons were detected on the central wires. On the other hand, when the scanning potential took the value of zero volts, the electrons were not forced outside the trap and as a result more electrons were detected on the central wires. This phenomenon produced the arched shape of the signal observed in the experimental results. Finally, the production and ionization of neutral ions was carried out in the last step of the operation of the prototype. There were two ways to inject neutral ions in the trapping region: by the use of atomic ovens or by the injection of gas through a leak valve. The first method was used for calcium atoms and the second one for molecular nitrogen. The injection/production of atoms is also reflected in the signal output of the detection scheme. While atoms were created or injected into the trap, electrons were absorbed and consequently less electrons were detected on the central wires producing a rise in the signal. The exception to this rule is when the scanning voltage on the external electrodes matched the electric potential required to produce the axial frequency of the ions that resonates with the electronic detection circuitry. In that point, a dip was observed demonstrating the presence of trapped ions. The production of calcium atoms from the atomic oven was not immediate, usually 20 seconds were needed to observed the dip in the signal. A simple vacuum chamber with an atomic oven fitted inside was built to study this phenomenon. The oven had a metallic plate placed in front of its output to observe the ejection of calcium atoms in a form of coating. The oven was operated under the same conditions as in the prototype (≈ 1.5 amperes) until a coating was observed in the plate. After these experiments were carried out, it was confirmed that a time of around 20 to 25 seconds is required to heat the oven until the calcium atoms were evaporated and observed as coating.

The experimental results of the operating prototype are shown in Fig. 4.11 for Ca^+ and in Fig. 4.12 for N_2^+. In Fig. 4.11, the circles represent the signal from the electronic detection system when the filament that produces ionizing electrons and the oven producing calcium atoms are switched off. The triangles are the result when the electron filament is on but the oven is switched off. The stars result when both electrons and calcium atoms are present. As previously mentioned, the calcium feature was predicted from simulations to occur at -1.35 V and is observed within the range of -1.5 to -1.1 V. On the other hand, for molecular nitrogen, Fig. 4.12, the resonance was expected to appear at -0.9 V and is observed within the range of -1.5

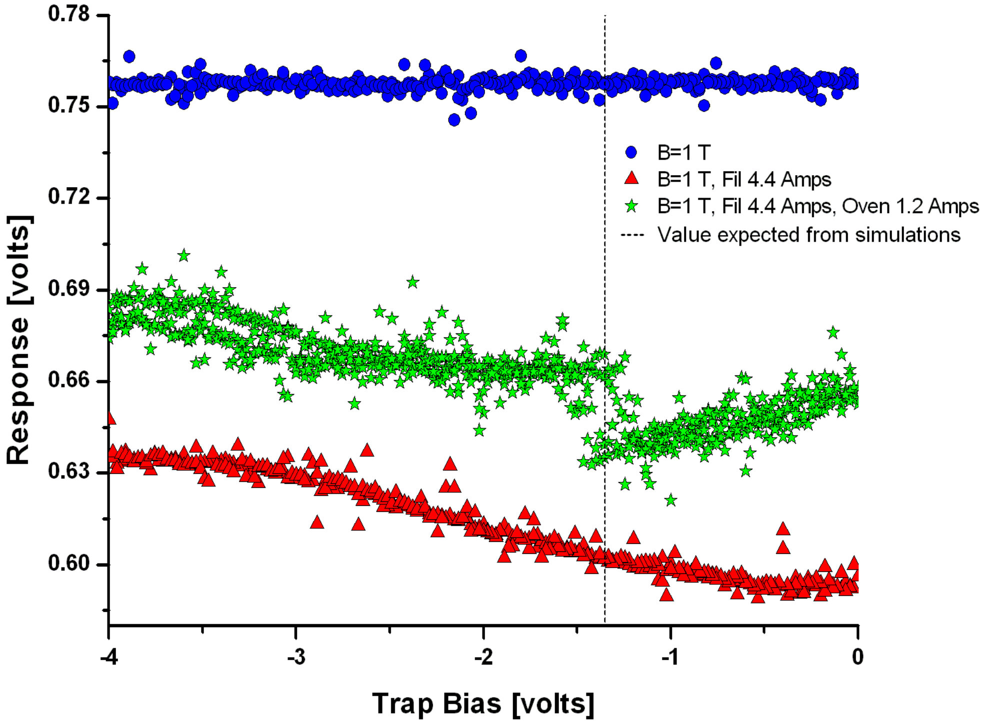

Figure 4.11: Experimental results of the electronic detection scheme for Ca^+.

to -0.5 volts.

From the experimental results of the wire trap prototype, one can observe that the response of the detection is not as clear as in the hyperbolic trap used to test the electronic detection. This is not surprising because the prototype is significantly smaller than the hyperbolic trap. A smaller trap size implies that less ions can be trapped and consequently the electronic signal generated by the image charges on the endcaps is smaller than in a trap with a larger size. The number of ions inside a trap can be estimated by making some simple approximations; in the exact case the number of trapped ions depends on all the ion-ion and ion-potential interactions, and the relative position of the ions (which is not homogenous). In the simple picture, one can assume that the trapped ions are homogenously arranged in a sphere at the centre of the trap. The electric potential produced by this sphere of charges, at a distance z (axial case), is given by

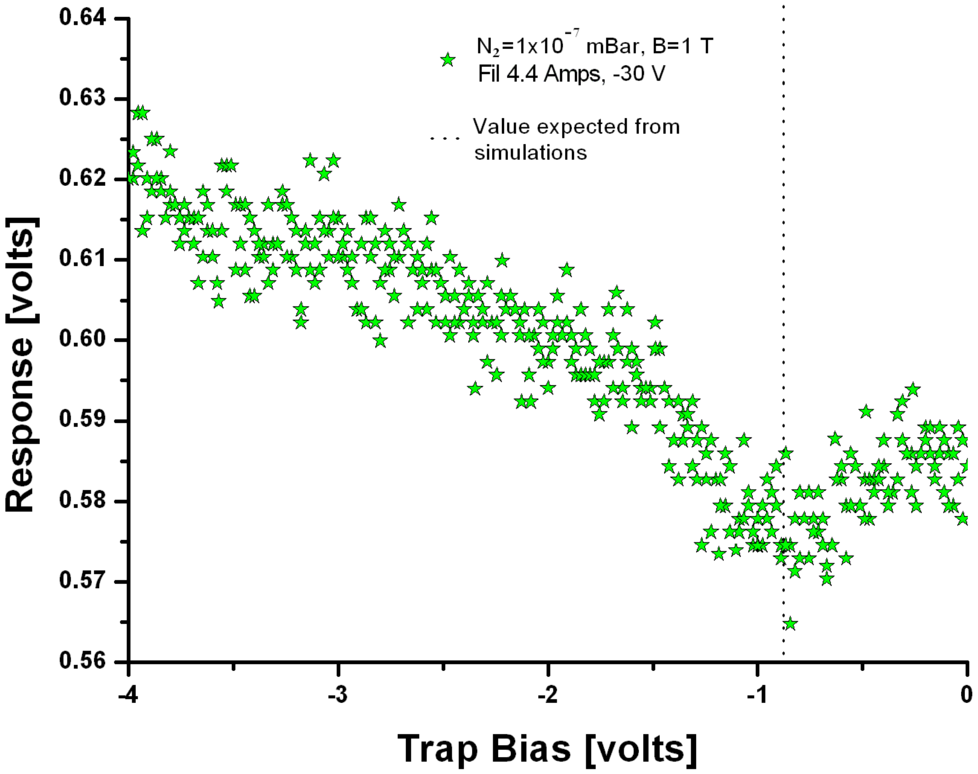

Figure 4.12: Experimental results of the electronic detection scheme for N_2^+.

$$\phi_{ions} = \frac{Nq}{4\pi\epsilon_0 z} \tag{4.2.5}$$

where N is the number of trapped ions and q their individual charge. In a stable trap, these ions would be confined by the quadrupole electric potential produced by the trap electrodes. This potential (ϕ_{trap}), around the centre of the trap, is

$$\phi_{trap}(z) = A_0 z^2 \tag{4.2.6}$$

where A_0 is a constant and depends on the electrode voltages and the trap dimensions; to be precise $A_0 = -2U_0/R_0 2$ in a hyperbolic trap. In a stable trap, a charged particle feels a force coming from the electrodes and a force from the other ions. As all the particles are confined, all the forces acting over the particle must cancel out. If the gross force exerted by the ions is approximated by that of a sphere of charges, in equilibrium it is possible to write

$$\frac{Nq}{4\pi\epsilon_0 z^2} = 2A_0 z \tag{4.2.7}$$

Consequently, the number of ions is approximately

$$N = 8\pi\epsilon_0 A_0 z^3 \tag{4.2.8}$$

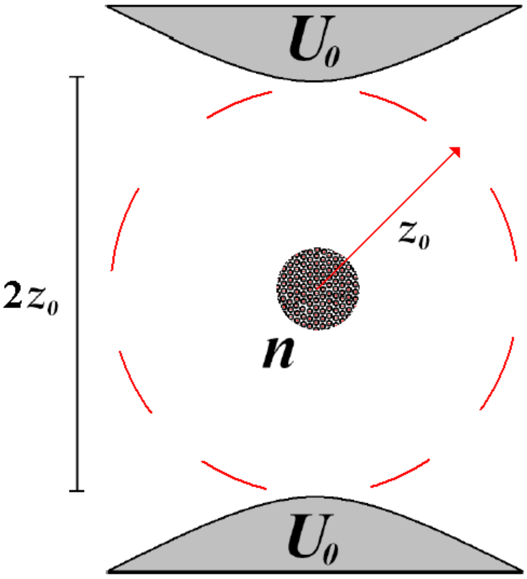

Figure 4.13: In a simple approximation, the confined ions in an ion trap can be described by a perfect sphere with a homogeneous density. In this approximation, the electric field at a distance z_0 would be given by that of a single point with charge Nq, where q is the charge of a individual ion.

This result is a only a very rough treatment as it is not expected that the ion cloud would extend all the way to the electrodes; however it gives a useful indication of the scaling of the number of trapped ions with z_0 (and consequently the amplitude of the electric signal in the trap electrodes). Eq. 4.2.8 shows that the number of ions grows to the power of three with the size of the trap. This is, at a distance z_0 from the trap centre $N \propto z_0^3$. For example, in the hyperbolic trap, the endcap electrodes are separated by 7 mm, in contrast in the wire trap prototype, the central wire electrodes are separated by 4 mm. According to these values, under this approximation, it is possible to determine that the wire trap prototype confined around five times fewer ions than the hyperbolic trap. This result is in agreement with the difference of signal amplitudes between the two traps; the signal dip shown by the hyperbolic trap has a depth of 0.13 volts whereas the dip depth in the wire trap prototype is 0.025 (0.13/0.025 =5.2).

The experimental results obtained with the prototype, like the examples shown in Figs. 4.11 and 4.12, demonstrate that the wire trap geometry operates successfully as a Penning trap. As a consequence, some new experiments have been proposed to explore some other applications that this trap design offers. The first of these experiments to be carried out in the future is the optical detection of calcium ions in the prototype running as a Penning trap. The next experiment is to run the prototype with a RF driver, as the experimental setup for these two experiments is very similar. On the other hand, middle and long term goals include the design of a scalable prototype to trap and transport ions between different trapping points. Some of these experiments are explained in the next section.

4.3 Future work with the wire trap.

As explained in previous sections, wire traps offer many advantages over traditional designs. Future applications of the wire traps are many, and some of them are already under development in the Ion Trapping Group at Imperial College. Modifications made to the prototype have opened the possibility of performing optical detection experiments with $^{40}\mathrm{Ca}^{+}$ ions. Furthermore, this new setup would be suitable for performing experiments with the prototype being run with a radio frequency (RF) drive; this will allow a direct experimental proof of the viability of the RF design. In addition to these experiments, the construction of scalable traps is being planned, having as a starting point the wire trap prototype. In this section some of the modifications carried out to the prototype to permit the optical detection experiments are discussed. In addition, some ideas for a scalable design are presented.

4.3.1 Optical Detection Experimental setup

Although the wire trap prototype was mainly designed and constructed with the electronic detection system in mind, the design also incorporated some features to facilitate experiments for future optical detection experiments. As mentioned previously, the prototype was constructed in such a way that allows optical access to the trapped ions. In addition, the prototype contains a support for a 40 mm focal length lens to collect fluorescence from the trapped ions. The setup for optical detection experiments is schematically presented in Fig. 4.14. In this modified setup, the upper atomic oven was replaced by the lens holder but everything else in the trap was essentially unchanged. The vacuum chamber was also modified to allow the optical access of lasers and the collection of fluorescence. This setup is shown in Fig. 4.15. As well as in the previous experiments, the atomic oven was filled with granular calcium for the production of calcium atoms. The main difference between the new vacuum chamber and the one used for electronic detection is the addition of two viewports. In the new setup, the leak valve used to inject molecular nitrogen in the original setup was replaced by an UHV compatible optical window to permit the collection of fluorescence. In

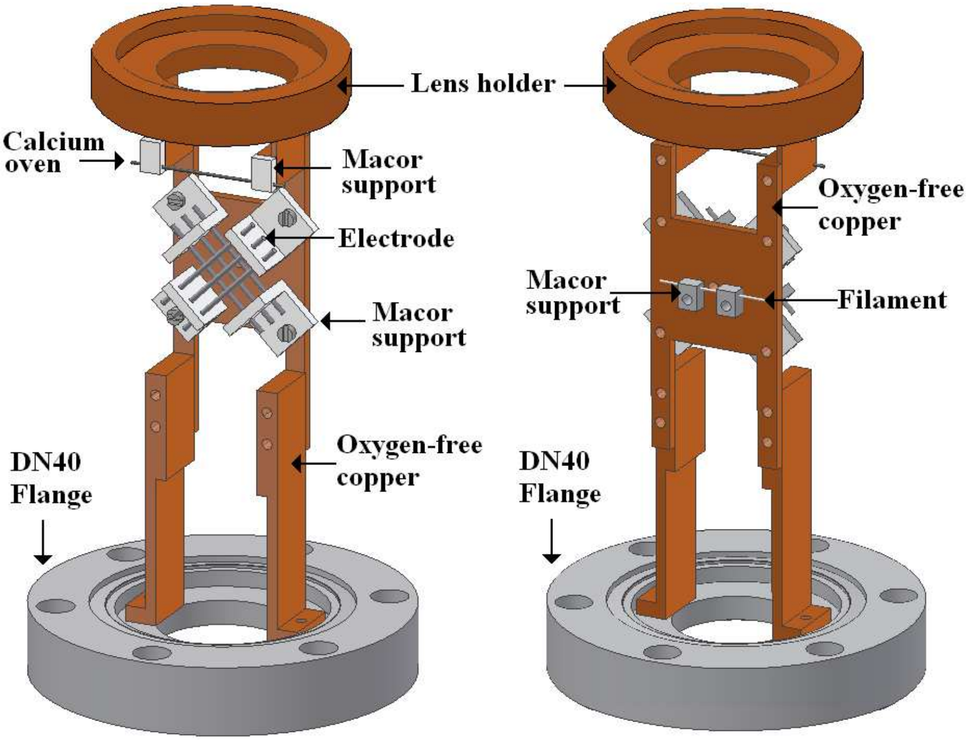

Figure 4.14: Experimental setup for optical detection.

addition, an angled optical viewport was incorporated into the setup to let the laser beams exit the chamber. An angled optical window was used to avoid the presence of laser reflections in the trapping region. The angled window and the 4-way cross that holds the trap were connected by a DN40 CF T-connector, the configuration is shown in Fig. 4.15. A 4-way cross with connections to the ion-gauge, the ion pump and a leak valve was connected to the rest of the system by a DN40 CF elbow. The whole system was placed inside a bake-out oven and then connected to the chain of vacuum pumps (a turbomolecular pump and a rotary pump).

Following the cleaning procedure and the evacuation method mentioned in Section 4.1, the trap was pumped out to a pressure of 8.0×10^{-7} mbar in 24 hours by turbomolecular and rotary pumps. At this pressure, the temperature of the baking system was increased from 25 ^{o}C to 90 ^{o}C, at a rate of 1 ^{o}C per minute. After this change of temperature, the system

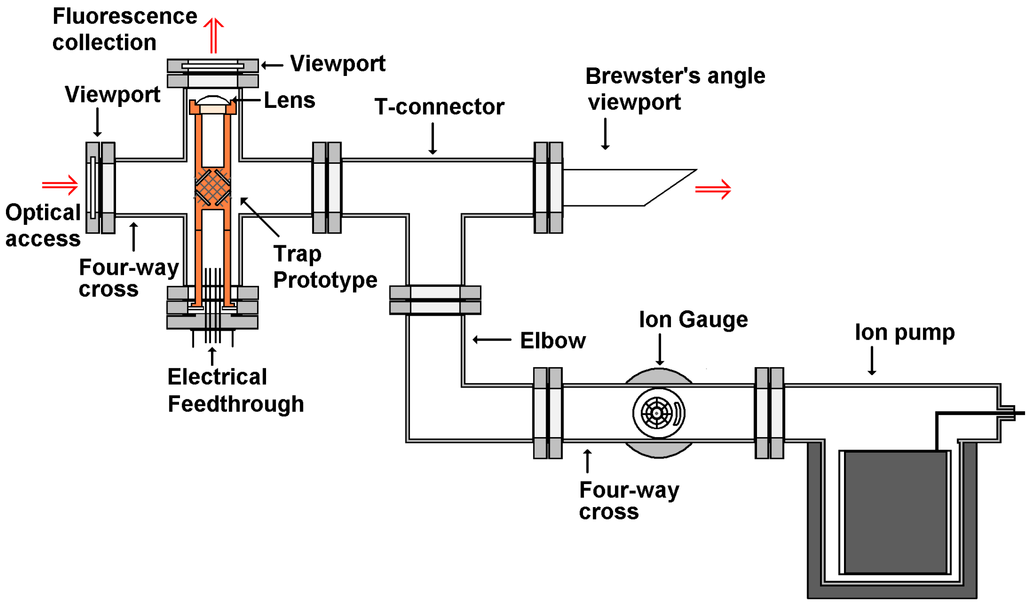

Figure 4.15: Schematic view of the vacuum chamber. The second four-way cross has a line perpendicular to the plane of the page, rotary and turbomolecular pumps were connected there.

pressure increased to 1.9×10^{-5} mbar. At this point, and to prevent damaging the turbomolecular pump, the system was left to pump out for 12 hours, achieving a pressure of 1.4 $\times10^{-6}$ mbar. From this point, the temperature of the chamber was increased constantly up to 200 ^{o}C in 4 hours but the pressure inside the chamber never exceeded 2.5×10^{-5} mbar. 12 hours later the vacuum system had pumped out the chamber to 2.9×10^{-6} mbar. The temperature was then increased again up to 240 ^{o}C resulting a pressure of 8.6×10^-6 mbar. At 240 ^{o}C the system continued pumping out for 48 hours. The final pressure of the chamber at 240 ^{o}C was 1.1×10^{-8} mbar. Then, the temperature was decreased at a rate of 1 ^{o}C/min and then left to pump out for another 48 hours. At a temperature of 80 ^{o}C the UHV valve that separates the trap setup from the baking system was closed and the ion pump was turned on. At 25 ^{o}C, with the ion pump pumping the trap, the setup was placed in its position between the poles of the magnet on the top of an optical table and left for 48 hours. The final pressure in the chamber after the baking and the pumping period was 6.0×10^{-10} mbar. All these steps verified that all the components in the setup were bakeable and UHV compatible at the 10^{-10} mbar level. Unfortunately, the operation of the trap did not have the same results.

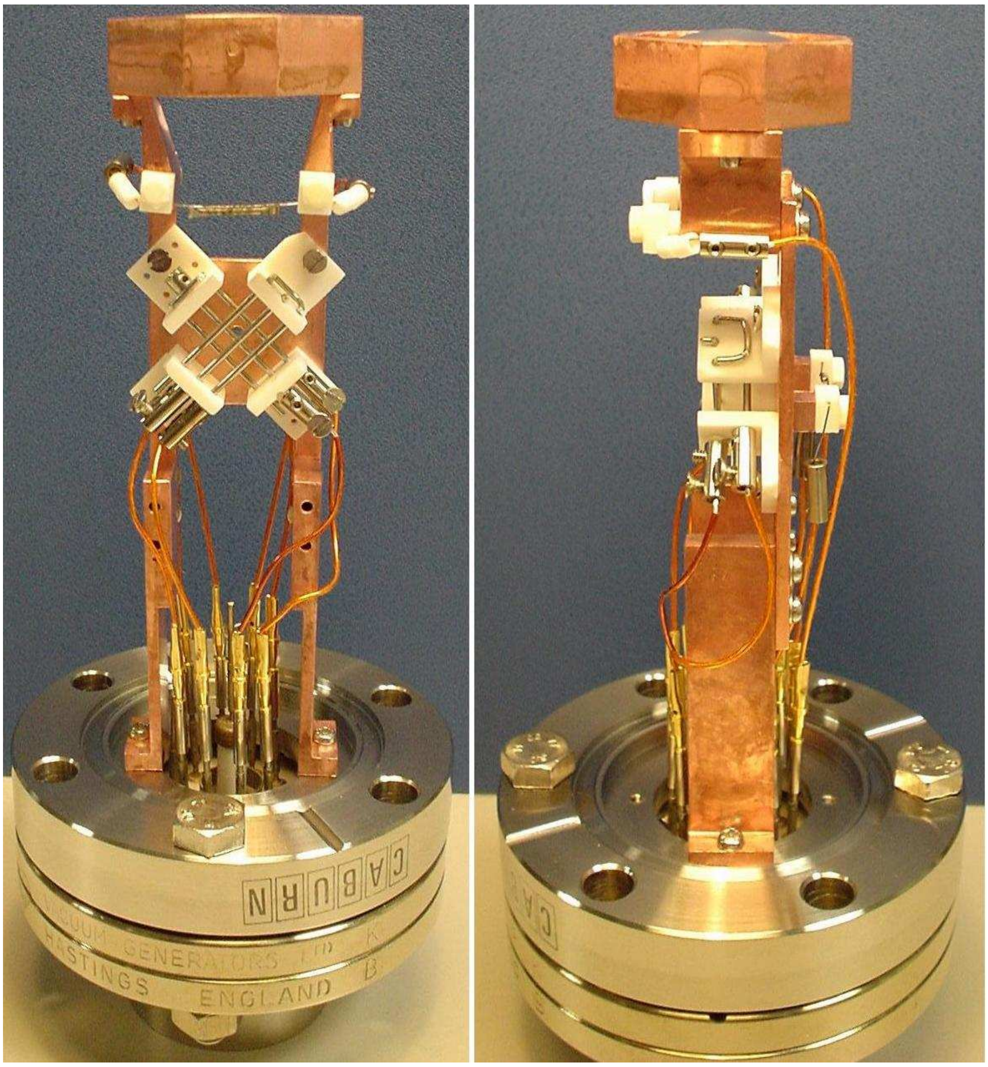

Figure 4.16: Photograph of the wire trap prototype for optical detection experiments.

The optical detection (laser cooling) technique was previously explained in Section 1.4.1, but briefly consists on the detection of the fluorescence emitted by trapped ions that are being excited by a laser (preferably in a fast transition). In the case of $^{40}\mathrm{Ca}^{+}$, laser cooling is achieved by exciting the transition $\mathrm{S}_{1/2} \longleftrightarrow \mathrm{P}_{3/2}$ (397 nm) and by repumping the transition

$P_{1/2} \longleftrightarrow D_{3/2}$ (866 nm). At Imperial College, an experimental setup with these characteristics is constantly used to detect trapped calcium ions in a hyperbolic trap. This setup is very often used as part of other projects aiming for applications of ions traps in QIP and/or towards the trapping and cooling of single Ca ions. As a result, this laser cooling setup is most of the time not available for other experiments. However, while the prototype was being tested, such a setup became available for a very short period of time (4 days). After all the considerations previously explained were taken, the prototype was tried for optical detection. The prototype was tried only once with the optical detection setup since it was clear that not all the requirements had not been taken into account. It was found that the separation of the macor L-shape mounts were not wide enough to permit the free access of the laser beams required for laser cooling. As the lasers hit the corners of the macor mounts, scattered light was sent towards all directions, including towards the photomultiplier. Later experiments also showed that macor is a translucent material that not only allows some light to pass through but it also diffuses the laser light. The scattered light diffused by the macor was detected in the photomultiplier, at the order of ≈ 400 counts/ms. This value is extremely high for background noise. The optical detection setup is commonly used in a hyperbolic trap that has similar dimensions than the one used in the electronic detection setup ($z_0 = 9$ mm). In this trap, the background noise is usually less than 5 counts/ms, as can be seen in the experimental results presented in Fig. 1.22. In addition, when the experiments with this hyperbolic trap are just started, non-optimized detection rates are in the range of 50 to 100 counts/ms. Based on these facts, optical detection experiments in the prototype were tried a few times (in a period of two days) but canceled and postponed until the trap was modified.

The prototype has been recently modified by members of the Ion Trapping Group. Until now, the separation of the macor mounts has been modified by removing some of the material of the mount. In addition, the macor components have been painted in black with Aquadaq (a carbon base paint that is UHV compatible) to avoid the glow of such parts. The prototype is currently being prepared for more optical detection experiments.

4.4 The transport of charged particles

The idea of moving ions around different trapping regions is, from the point of view of some authors, a necessity in quantum computation [48]. This requirement creates a scheme where ions can be loaded into an ion trap, cooled, and then shuttled into different single traps for storage. In addition, a design with such capabilities would benefit applications where the transportation of charged particles are required. Under this scenario, some scalable designs for ion traps have been presented that permit the transport of ions between traps in a scalable configuration [21] [44]. Following this idea, this section presents a scalable configuration of wire traps that can produce a scheme where trapped ions can be produced in one trap and then shuttled to another different trap. This design is also capable of producing conditions to transport ions around a corner.

The scheme presented to transport ions is basically the combination of the trap geometries of the planar guide and the wire trap. As mentioned before, the planar guide is able to generate conditions to transport ions [41] and, in contrast, the wire trap generates conditions for trapping. These two properties can be combined to present a scheme to transport ions, [44]. The layout of this proposal is illustrated in Fig. 4.17.

The setup presented in Fig. 4.17 consists of three concentric circular wires that are placed above three straight parallel wires that in combination create the desired setup. In the simulations presented in Fig. 4.17, the circles formed by the upper wires have diameters of 60, 70 and 80 mm respectively, whereas their individual diameters are of 2 mm. On the other hand, the straight wires are separated by 10 mm, and their individual diameters are also 2 mm. The position of the straight wires is such that the central wire is aligned to the common center of the circular wires. In addition, a magnetic field of 1 tesla and perpendicular to the plane of the wires is incorporated into the simulations. In this example, two trapping regions are formed at the crossing points of the two sets of wires. In the spaces between the crossings, the parallel wires are used as guide traps to transport the ions. A trapped ion stored in a trapping region can be forced to leave it by generating a potential

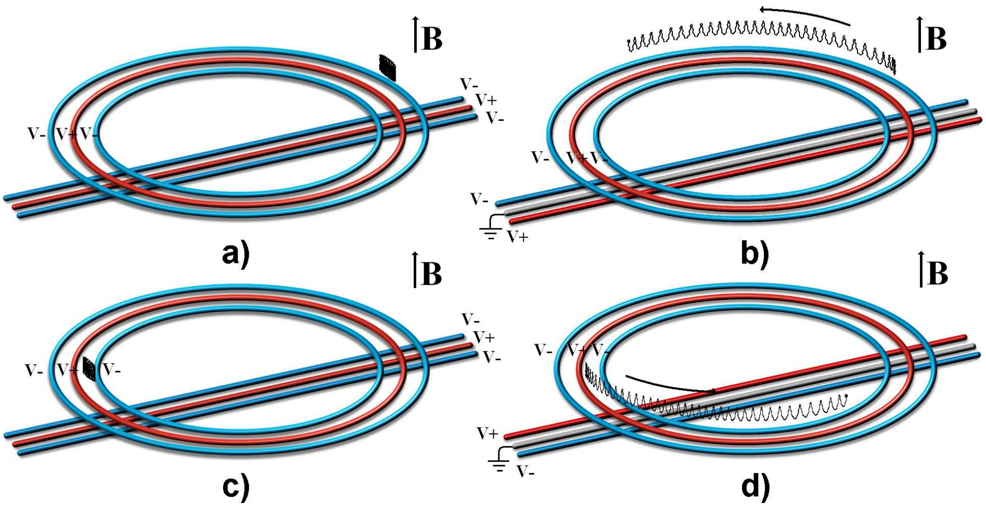

Figure 4.17: Simulations of a trap design to transport ions. In *a*) external wires are connected to $-5V$, and central wires to +5 V. In *b*) upper set as in *a*), lower set connected to −3 V, 0 V, +5 V respectively. In *c*) all potential levels as in *a*). In *d*) upper set as in *a*), lower set connected to +5 V, 0 V, −3 V. Simulations for Ca^+ at 1×10^{-1} eV using SIMION.

gradient in the desired direction using the electrodes that are perpendicular to that direction. This is illustrated in Fig. 4.17. In this figure, a simulation of a trapped Ca^+ ion is observed in the right crossing, where both sets of wires are connected to a potential difference of -10 V. In Fig. 4.17b, the upper set of wires remains at the original potentials creating an ion guide along its path but the lower straight set of wires has been connected in such a way that they produce a potential gradient which pushes the ions away from the old trapping region and around the ring. In Fig. 4.17c the lower set of wires is adjusted to the same levels as in Fig. 4.17a producing the trapping conditions again. In Fig. 4.17d a potential gradient is created again to force the ions to leave the trapping region and follow the path of the ion guide back to the next trapping region.

This scheme for transporting ions is not unique as many other geometries can be proposed. An alternative configuration, that is scalable, is schematically presented in Fig. 4.18.

This design, in a similar way than the circular scheme, can create a three

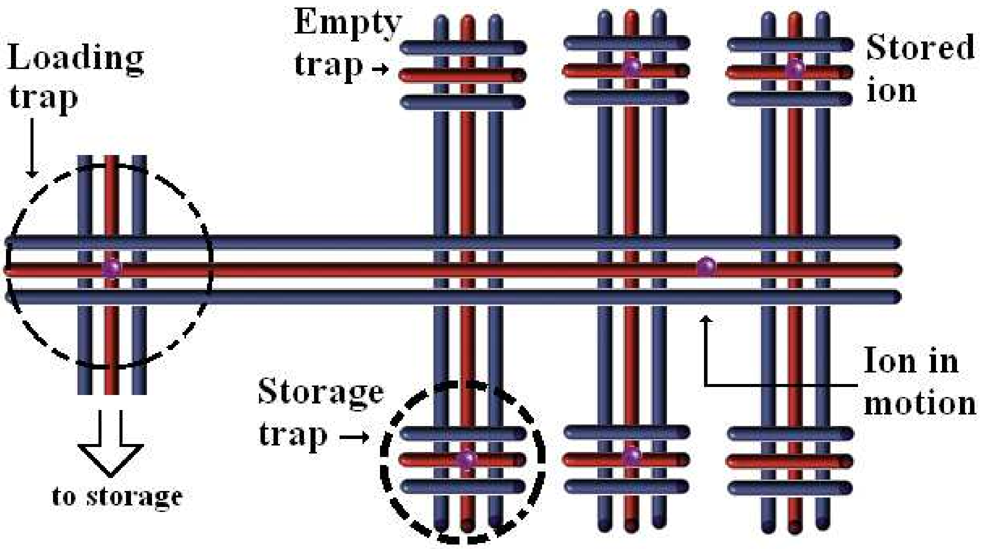

Figure 4.18: Scalable design for ion traps. The tracks formed by the long straight wires can be used as planar guide traps to transport ions from one trap to another one. The motion is generated by creating an electric potential gradient.

dimensional trapping region in the junctions and an electric potential to produce the shuttling of ions to other trapping points. This scheme also has the ability to transport charged particles around a corner in the array of wires. The shutting conditions are achieved by replacing the quadrupole potential of both set of wires by a potential gradient in the desired direction of motion. Fig. 4.19a shows a snapshot of the axial electric potential when trapping conditions are established in the surroundings of a junction. This simulation was produced in SIMION, with the following conditions: wires are separated by 10 mm in a set and sets are 20 mm apart, wires are connected to +5 V, - 5 V and +5 V respectively in both set of wires. On the other hand, Fig. 4.19b presents the axial electric potential when a potential gradient is created in both sets of wires by connecting the wires to +5 V, 0 V and -5V. Under these conditions, an electric potential track is created that would allow the controlled transport of ions through the corner.

This section has presented a scheme to trap and transport charged particles in a controlled way in an array of wires. These properties lead to more

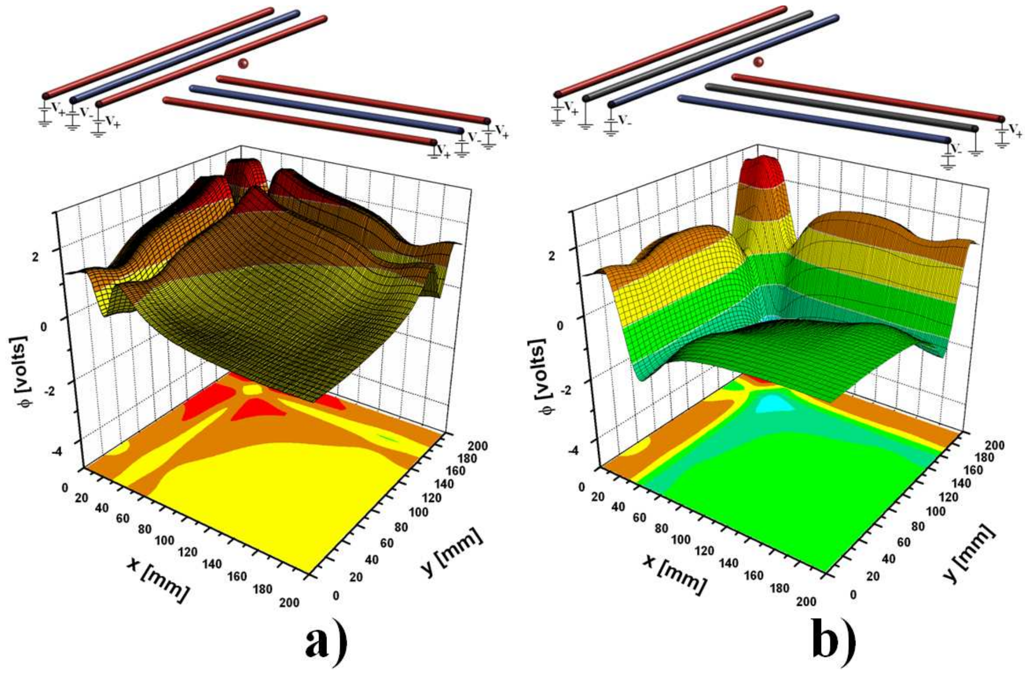

Figure 4.19: The figures on the top present the conditions of the wires; the colour blue indicates that the wire is connected to +5 V, colour red indicates -5 V, and gray denotes a grounded wire. In the left (a) images the scheme is being operated as a trap. In the left (b) images the scheme is being operated in such a way to shuttle charged particles around the corner.

complex systems where ions are trapped in a particular space and then sent to other regions where they can be used for other purposes. In the next section, the analysis of this scalable array of wire traps is continued but in a different way.

4.5 Trap-trap interaction

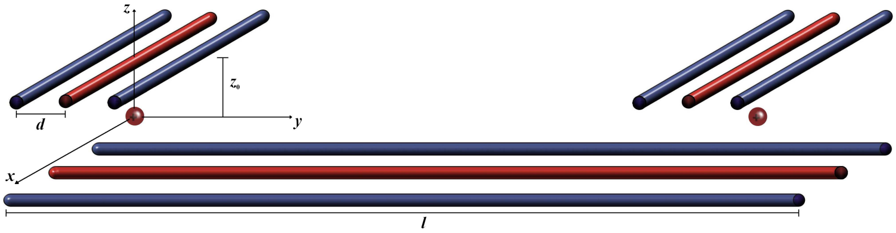

Figure 4.20: Two-trap configuration. By design, both traps share the lower set of electrodes, consequently this configuration allows the exchange of the motion information between trapped particles. If desired, switches can be placed along the electrodes to turn on and off the interaction.

The last sections have presented scalable designs of wire traps that allow the confinement of charged particles in different trapping points in a array of wires. These arrays present an interesting setup as two or more traps are connected together by means of a mutual set of three wire electrodes. An example of this geometry is presented in Fig. 4.20. In this setup, the scalable design is simply created by the addition of perpendicular electrodes along the path of three electrodes. This scheme allows the study of interaction effects between two ions trapped in the center of two different traps. The interaction is produced by means of induced charges on the common lower electrodes. This approach has been discussed before for planar traps in [19], and in this section a similar analysis is presented but applied into a system consisting of two wire traps with a single ion each.

The interaction between the particles in Fig. 4.20 is produced because each particle generates an oscillating image charge in the lower electrodes. In practice, the trap electrodes are connected to power supplies, or to earth, to produce the trapping conditions. These power supplies will cancel out the induced charge on the wire electrodes unless a large inductor (a low pass filter) is connected between the supplies and the electrodes. By using this current choke, the induced charge on the electrodes will be isolated from the power supplies. The amount of induced charge is different between the central and the exterior wires as they are placed at different distances. For simplicity, in our analysis all wires have a common radius a and a length l. The induced charges are Q_1 and Q_2 for the central and external lower wires respectively and R is an arbitrary distance at which the potential is set to be zero. The classical Hamiltonian of the system presented in Fig. 4.20 can be written as

$$H(z_1, z_2) = H_1(z_1) + H_2(z_2) + H_{int}(z_1, z_2) \tag{4.5.1}$$

where H_1 and H_2 are the harmonic oscillator Hamiltonians of the trapping ions, z_1 and z_2 are the axial positions of the left and right particles respectively, and H_{int} is the Hamiltonian of the interaction. As the interaction is due to the induced charges (Q_1 and Q_2), H_{int} takes the form

$$H(z_1, z_2) = H_1(z_1) + H_2(z_2) + q\phi_1(z_1) + q\phi_2(z_2) + \frac{Q_1^2}{2C} + \frac{Q_2^2}{C} \tag{4.5.2}$$

where q is the charge of the trapped particles, Q_1 is the induced charge on the central electrode, Q_2 is the induced charge on the external electrodes, ϕ_1 is the electric potential generated by Q_1 and Q_2 at z_1, ϕ_2 is the electric potential generated by Q_1 and Q_2 at z_2, and C is the capacitance of the wires. The electric potential generated by three parallel wires with linear charge densities Q_2/l, Q_1/l and Q_2/l is given by

$$\phi = -\frac{1}{4\pi\epsilon_0 l}\left(Q_2 \ln\frac{R^2}{(y+d)^2 + (z+z_0)^2} + Q_1 \ln\frac{R^2}{y^2 + (z+z_0)^2} + \right.$$
$$\left. + Q_2 \ln\frac{R^2}{(y-d)^2 + (z+z_0)^2}\right)$$

where l is the length of the wires. In the center of the trap, $y = 0$, the potential is given by

$$\phi = -\frac{1}{4\pi\epsilon_0 l}\left(2Q_2 \ln\frac{R^2}{d^2 + (z+z_0)^2} + Q_1 \ln\frac{R^2}{y^2 + (z+z_0)^2}\right)$$

By replacing this expression into Eq. 4.5.2, the detailed hamiltonian of the interaction can be written as

$$H_{int}(z_1,z_2) = \\ +q\frac{Q_1}{4\pi\epsilon_0 l}\ln\frac{R^2}{d^2+(z_1+z_0)^2}+q\frac{Q_2}{2\pi\epsilon_0 l}\ln\frac{R^2}{d^2+(z_1+z_0)^2}+ \\ +q\frac{Q_1}{4\pi\epsilon_0 l}\ln\frac{R^2}{d^2+(z_2+z_0)^2}+q\frac{Q_2}{2\pi\epsilon_0 l}\ln\frac{R^2}{d^2+(z_2+z_0)^2}+\frac{Q_1^2}{2C}+\frac{Q_2^2}{C} \tag{4.5.3}$$

where d is the separation of the wires and $2z_0$ the separation of the two sets of wires. If Q_1 and Q_2 are adiabatically driven, [19], it is possible to write

$$\frac{dH_{int}}{dQ_1}=0 \text{ and } \frac{dH_{int}}{dQ_2}=0 \tag{4.5.4}$$

where each of these equations gives a relationship for Q_1 and Q_2 in terms of z_1 and z_2 respectively. Consequently, by substituting and simplifying these expressions into Eq. 4.5.3, the expression for the interaction Hamiltonian is

$$H_{int}(z_1,z_2) = -\frac{5q^2\left(\ln\frac{R^2}{d^2+(z_1+z_0)^2}+\ln\frac{R^2}{d^2+(z_2+z_0)^2}\right)^2 C}{32l^2\pi^2\epsilon_0^2} \tag{4.5.5}$$

From this equation, to estimate the first order interaction, Taylor expansions around the potential minima ($z_1=\widetilde{z}_1+z_{min}$ and $z_2=\widetilde{z}_2+z_{min}$) are calculated. In this case, both particles are oscillating around the center of the trap, this is at $z_{min}=0$. As only the crossed linear terms are needed (terms with the factor $\widetilde{z}_1\widetilde{z}_2$), the Taylor expansions are only calculated from the constant up to the linear term. So, the linear interaction Hamiltonian ($\widetilde{H}_{int}$) is:

$$\widetilde{H}_{int}=\frac{5q^2z_0^2C}{4\pi^2\epsilon_0^2l^2(d^2+z_0^2)^2}\widetilde{z}_1\widetilde{z}_2 \tag{4.5.6}$$

where $\widetilde{z}_1$ and $\widetilde{z}_2$ can be expressed with ladder operators as follows

$$\widetilde{z}=\sqrt{\frac{\hbar}{2m\omega}}(\hat{a}+\hat{a}^\dagger) \tag{4.5.7}$$

using this expression, the well-known quantised Hamiltonian is

$$\widetilde{H}_{int} = \hbar\omega_{int}(\hat{a}_1^\dagger \hat{a}_2 + \hat{a}_1 \hat{a}_2^\dagger) \tag{4.5.8}$$

where ω_{int} is then

$$\omega_{int} = \frac{5q^2 z_0^2}{8\pi^2 \epsilon_0^2 l^2 m\omega_0 (d^2 + z_0^2)^2} C \tag{4.5.9}$$

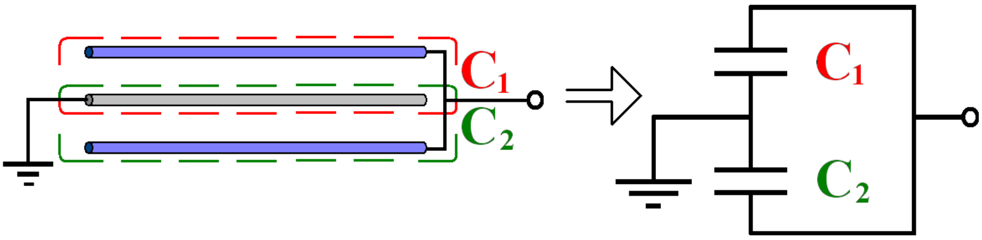

Figure 4.21: The overall capacitance of three wires, when connected in the way presented in the figure, is equivalent to two capacitors connected in parallel.

The capacitance of the three wires is easily calculated by analyzing the electronic diagram of the trap, this is presented in Fig. 4.21. As the circuit is equivalent to a circuit where two equal capacitors are connected in parallel, the total capacitance of the system is two times the capacitance of two parallel wires, which is a well-known value. The capacitance of two charged parallel wires is

$$C_{two-wires} = \frac{\pi\epsilon_0}{\ln d/a} l \tag{4.5.10}$$

where a is the radius of the wires. Consequently, the final expression for the interaction frequency is

$$\omega_{int} = \frac{5q^2 z_0^2}{4\pi\epsilon_0 l m\omega_0 \ln{(d/a)}(d^2 + z_0^2)^2} \tag{4.5.11}$$

For calcium, $m = 40$ amu, the interaction frequency is given by

$$\omega_{int} = 1.73 \left[\frac{\mathrm{rad}^2 m^3}{s^2}\right] \frac{z_0^2}{l\omega_0 \ln{(d/a)}(d^2 + z_0^2)^2} \tag{4.5.12}$$

In a two-trap system with traps of similar characteristics (milliliter scale) than the prototype presented in the last section ($z_0 = 2$ mm, $d = 3$ mm and $a = 0.5$ mm),

$$\omega_{int} = 2.3 \times 10^4 \left[\frac{\mathrm{rad}^2 m}{s^2}\right] \frac{1}{l\omega_0} \tag{4.5.13}$$

If this system is used under the same conditions as the prototype, $\omega_z = 145$ kHz, and the traps are separated by 10 mm, the interaction frequency is $\omega_{int} = 25$ Hz. If required, the dimensions of the traps or the operational parameters can be changed to tune the interaction frequency to a desired range. In addition, switches can be installed on the wires between the traps to turn on and off the interaction. In fact, it is possible to carry out a similar analysis like the one presented above, to obtain the interaction frequency of two ions trapped in the outer positions of the traps. In such conditions, the position of the trapped particles can be modified by tuning the voltages on the wires (this was presented in Section 2.1). This implies that even for a fixed setup, the interaction can be effectively control by attracting the particle to the wires. There are other proposals to produce a scheme with interacting particles; the most simple one is to consider only the Coulomb interaction of two ions. However, this scheme does not attract much attention because the interaction cannot be controlled or switched off, a requirement desired in quantum computation, [19].

5 The two-plate trap

Ever since the work of W. Paul was published in 1950, ion traps have been constantly used in all sort of experiments. The trap geometries are often changed as a response to the requirements of the new applications and, as a consequence, the number of ion trap geometries has been increased in recent years. Commonly, these novel geometries are modifications or upgrades of other designs that, in one way or another, present an improvement to a particular application. In some other cases, the modifications done to a trap geometry are so extensive that the design has to be classified as novel. The latter case can be applied to planar and wire traps because their geometries are too different from hyperbolic, linear, or cylindrical traps to be classified as modifications of one of them. The trap presented in this section could be classified as a modification of the planar trap but this should not undermine the contribution of this proposal as it can be advantageous in applications where a simpler geometry is required. The trap is explained in the following section.

5.1 The proposal

The trap presented in this section is inspired by the geometry of the planar trap, [19]. As mentioned previously, the planar trap consists of a central disk connected to a positive voltage surrounded by a planar ring connected to a negative voltage (to trap positive ions). These two electrodes (disk and ring) are surrounded by a grounded planar electrode and consequently, the whole geometry is embedded in a planar substrate. When considering the construction of such device, the problems emerge when the electrodes and connectors are included in the design. In [19], connectors coming through the substrate are proposed to solve this problem. This scheme allows the independent manipulation of traps but, because the number of connectors increases with the number of traps, the micro-construction or the mass construction of this trap could be difficult. The geometry presented in Fig. 5.1 proposes a solution for such a problem by sending one of the electrodes to another plane. The design by itself does not allow the independent manipulation of traps, but

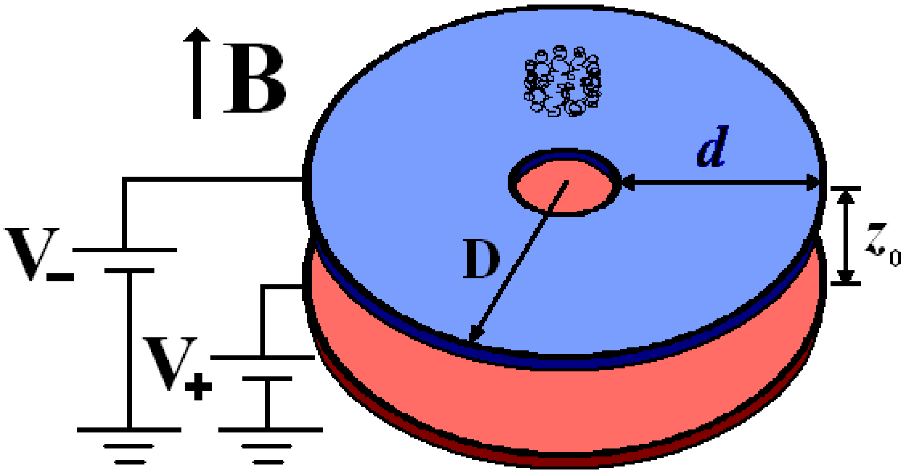

Figure 5.1: Sketch of the trap and geometric parameters. The simulated trapped ion trajectory shown in the figure corresponds to a molecular ion with a mass of 100 amu and with an initial kinetic energy of 100 meV in an applied magnetic field of B=1 T as shown. The upper electrode is connected to −5 V and the lower one to +5 V. The axial potential of this configuration is shown in Fig. 5.2. The simulation was performed using SIMION.

the simplicity of the geometry may be advantageous in applications of spectroscopy. In addition, the design presents a straight-forward scalability and an interaction scheme by induced charges can be proposed because the traps share the electrode configuration.

Essentially the trap is made of two planar electrodes positioned at different planes ($z = 0$ and $z = z_0$). The upper electrode is a planar ring with a width d in the plane $z = z_0$. The lower electrode is a disk of radius D in the plane $z = 0$. This type of configuration is able to produce an axial trapping potential above the electrodes when they are oppositely charged; confinement in the radial plane is produced by the addition of a magnetic field perpendicular to the electrode planes. A simulated trajectory for a trapped ion in this trap is shown in Fig. 5.1. In addition, two axial electrostatic potentials for positively charged ions are presented in Fig. 5.2; in one case the upper electrode is connected to −5 V and the lower to +5 V and in the second case the upper electrode is connected to −5 V and the the other is grounded (in

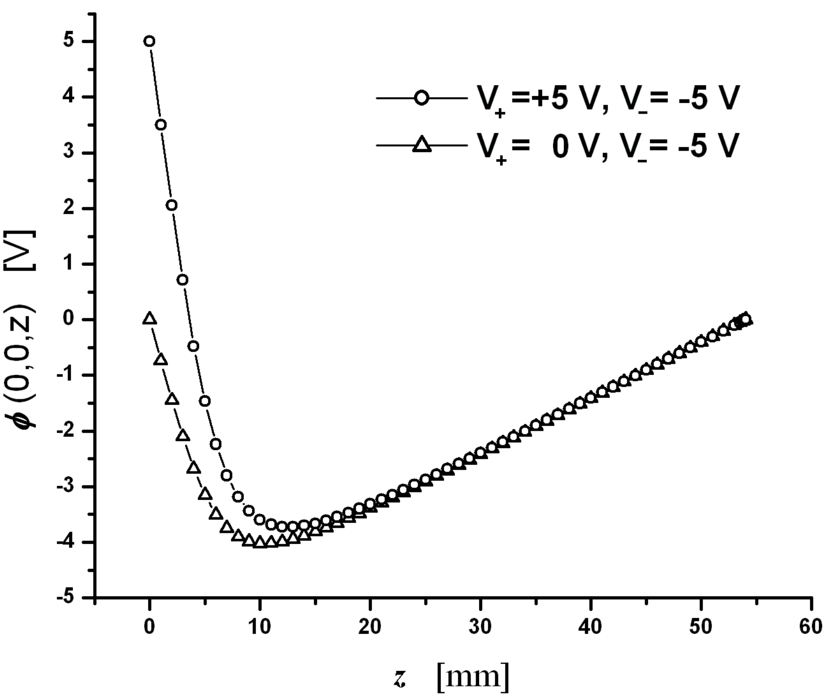

Figure 5.2: Axial electric potential generated by the two-plate trap shown in Fig. 5.1 for $z_0 = 5$ mm, and $D - d = 10$ mm and with the electrodes connected to ± 5 volts as shown. In this simulation, the ground is a disk plate placed at z=55 mm. The simulation was performed using SIMION.

both cases $z_0 = 5$ mm and $D - d = 10$ mm). In addition, three dimensional equipotential surfaces are presented in Fig. 5.4.

Like some of the other designs presented here, this trap exhibits great scalability with an easy construction and a good optical access due to the open structure. In fact, this trap is one of the most simplest designs of an ion trap as it consists only of two parallel plates with a hole in one of them. By design, the alignment of this trap is also simple as it would only consists of fixing two parallel planes. Another interesting characteristic of this design is its straightforward scalability. An array of traps can be created by only increasing the number of holes in the two-plate configuration. Using this idea, a scalable design is presented in Fig. 5.4.

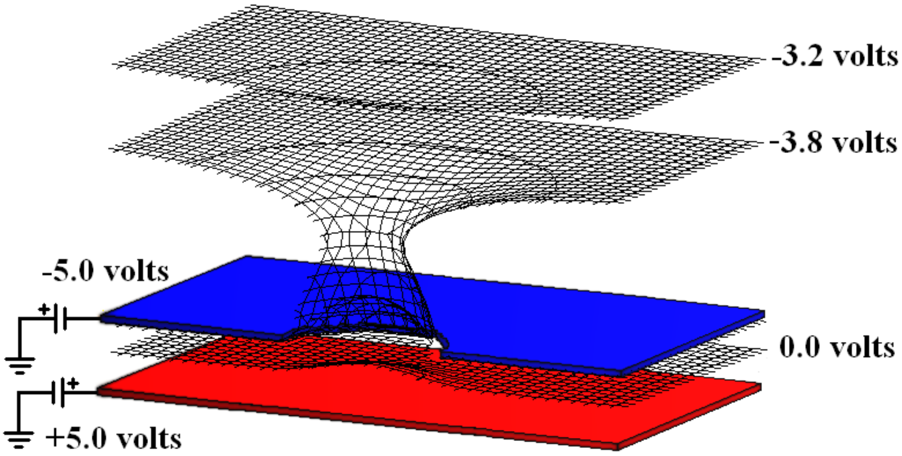

Figure 5.3: Three-dimensional equipotential surfaces for the two-plate ion trap. The surfaces correspond to -3.8 V, -3.2 V and 0.0 V. The upper electrode is connected to -5 V (red electrode) and the lower one to $+5$ V (blue electrode), $z_0 = 5$ mm, $r = 5$ mm $R = 55$ mm. Simulations performed using SIMION.

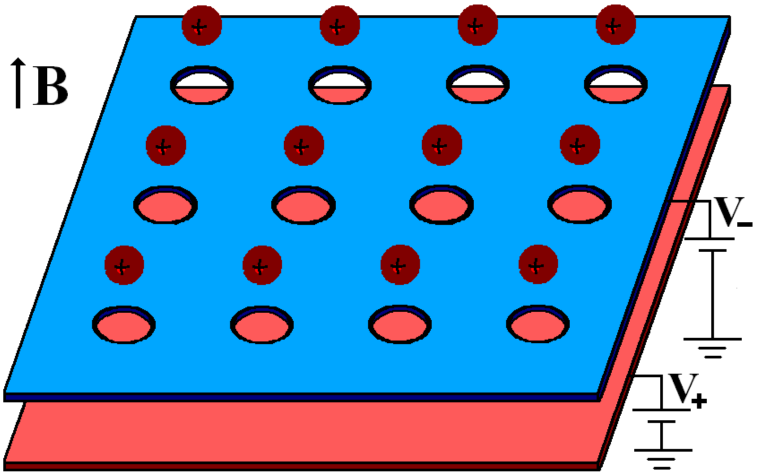

Figure 5.4: Schematic view of a multiple trap design.

The potential depth and the position of the potential minima in the scalable design depend on the separation of the plates and on the separation of the traps. In the extreme scenario, a scalable design of a two-plate trap with small holes would create a parallel-plate capacitor-like potential and thus the potential minima would be located in the plane of the holed plate. Despite its interesting qualities, the two-plate trap does not have an analytical expression for its electric potential. This, however, has not been a limitation in other designs of ion traps [21] where the characterization of the traps is done either empirically or by computer simulations (the second being the most common).

At this point, five novel designs for ion traps have been presented: two Penning traps, two RF traps and an the two-plate trap (which is a Penning trap). These traps are original contributions that were proposed by the author of this thesis at Imperial College during the period 2003 to 2006. In addition, during this time, a cylindrical trap was designed to fulfill the requirements of harmonicity and orthogonality (both characteristics are explained in the next section). This cylindrical trap is still under construction but it is planned that the trap will be used in experiments with highly charged ions in the close future. The trap and its attributes are explained in the next section.

6 The HITRAP trap

In this thesis, several designs for ion traps have been presented. Some of them are novel proposals which are still under development and testing, and others are traditional designs that have been used in different applications since their development around twenty years ago. Among the traditional designs, the cylindrical trap is one of the geometries that has been repeatedly and reliably used since its development in 1989. The cylindrical trap is a successful design because it provides a good optical access together with a harmonic potential (in a design with compensation electrodes), is easy to machine and assemble and is ideal for loading ions from an external source. In 2002, when the HITRAP network was created to carry out experiments with highly charged ions in Penning traps, cylindrical traps were already being used in a large number of successful experiments and consequently its design was chosen for HITRAP. This section reports the design and characteristics of the cylindrical trap that will be used for the study of highly charged ions within the HITRAP project. The calculations and simulations presented in the following text were performed to support the technical design proposed by Dr. Manuel Vogel and Prof. Richard Thompson in 2005.

6.1 The design

The HITRAP spectroscopy trap has been under design since 2003 and its construction began in 2006. Its design and construction was delayed several times due to changes in the project specifications. In the original proposal, the injection of the highly charged ions would have been from below the trap, implying the use of a superconductor magnet with a vertical bore. During the HITRAP meetings held between the years 2004 to 2005, the design evolved mostly due to the lack of an available magnet with appropriate specifications.

In January 2005 a magnet inside the HITRAP network became available and the dimensions of the trap were finally agreed. The first technical drawing of the trap was presented in April 2005, based on the dimensions of the magnet bore. Because the magnet has not been shipped to GSI (home of the HITRAP project) and its availability was not absolutely confirmed, the spectroscopy trap was designed to fit in different magnet bores in case the magnet mentioned were not to be available by the proposed date of operation (end of 2008). At this moment (January 2007), the spectroscopy trap is still under construction as well as most of the HITRAP setup. Although many of the final parameters are still unknown, like the final energy of the ions or the ion species to be used, the design of the trap is only dependent on a few parameters that are already known (including some dimensions of the magnet bore). Plans for testing the trap at Imperial College with singly ionized ion species like $^{40}\mathrm{Ca}^{+}$ or N_2^{+} are being planned prior to the measurements with HCI at GSI.

Briefly, the HITRAP trap design had to fulfill these requirements:

1) As this is a trap that is going to be used in spectroscopy studies, its design must allow good optical access to the trapped ions.

2) The trap geometry must provide a good solid angle to collect the fluorescence emitted by the trapped ions.

3) The trap must allow the loading of ions from the other components of the HITRAP setup.

4) Preferably, the trap should be harmonic to obtain a simple ion motion.

5) It must be Ultra High Vacuum and cryogenic compatible, at a pressure comparable to the rest of the HITRAP setup (proposed to operate at $\approx 10^{-11}$ mbar).

6) The trap needs to produce a strong confinement; consequently high magnetic fields and a mechanism to compress the ion cloud are required (rotating wall technique).

7) The trap must allow the cooling of the trapped ions; the design has to include a cooling mechanism.

After all these considerations were analyzed, the cylindrical design arose as the trap geometry that fulfills most of these requirements. A cylindrical design with compensation electrodes is able to produce the desired harmonic potential. The optical access of this design provides an excellent setup to allow the laser excitation as well as the ion injection. The requirement of UHV compatibility is simple to fulfill as the cylindrical design is easy to machine and facilitates the use of UHV materials in the construction of the trap (some materials like Macor can only be machined in simple shapes). To fulfill the requirement of a good solid angle, a trap with an expanded ring electrode with its walls made of a fine metallic mesh was designed. As a consequence, the dimensions of the trap prototype were chosen, first of all, to produce good optical access and a large solid angle for the fluorescence collection and secondly to produce a harmonic trapping potential. In addition, extra cylindrical electrodes (capture electrodes) were included in the design to facilitate the injection of the ions at both ends of the trap, and the ring electrode was segmented to implement ion cloud compression techniques such as the rotating wall [49]. The technique of rotating wall uses phased AC signals that rotate about the trap axis. The interaction of this field with the ion cloud generates a torque that can be use to modify the shape of the cloud and consequently the density of the cloud. Each segment of the ring electrode carries the AC field but with a specific phase. Typically, the phase of the voltages is fixed and depends on the number of ring segments. The dynamics of large coupled ion cloud cannot be described by the dynamics of individual charged particles; in this systems, the density of the could depends on a global rotation [50]. To achieve a maximum cloud density, the frequency of the AC voltages is set to half the cyclotron frequency [49]. The proposed operation of the HITRAP trap can be summarized as follows: the highly charged ions enter from below the trap, are reflected by the upper capture electrode, enclosed by the lower capture electrode, confined by the trap electrodes, cooled by a resonant resistive circuit and finally compressed by the rotating wall technique [30].

The harmonicity of the trap can be calculated by the expansion coefficient method explained in Section 1.3.1. There, it was shown that the electric potential generated by a cylindrical trap with compensation electrodes can be expressed as

$$V = V_0\phi_0 + V_c\phi_c \tag{6.1.1}$$

where V_0 and V_c are the magnitudes of the voltages applied to the endcaps and the compensation electrodes respectively. On the other hand, in spherical coordinates, ϕ_0 and ϕ_c are written as

$$\phi_0 = \frac{1}{2}\sum_{n=0}^{\infty} C_k^{(0)} \left(\frac{r}{d}\right)^k \mathbf{P}_k(\cos\theta) \tag{6.1.2}$$

and

$$\phi_c = \frac{1}{2}\sum_{n=0}^{\infty} D_k \left(\frac{r}{d}\right)^k \mathbf{P}_k(\cos\theta) \tag{6.1.3}$$

Combining, Eqns. 6.1.2, 6.1.3 and 6.1.1 one obtains

$$C_k = C_k^{(0)} + D_k \frac{V_c}{V_0} \tag{6.1.4}$$

which provides the relationship to cancel out a desired term (C_k). In the case of cylindrical traps, Eqns. 6.1.2 and 6.1.3 can be simplified due to the cylindrical and azimuthal symmetry of the trap geometry, [15]. The simplified potentials can be written as

$$\phi_0 = \frac{1}{2}\sum_{n=0}^{\infty} A_n^{(0)} J_0(ik_n r)\cos(k_n z) \tag{6.1.5}$$

and

$$\phi_c = \frac{1}{2}\sum_{n=0}^{\infty} A_n^{(c)} J_0(ik_n r)\cos(k_n z) \tag{6.1.6}$$

where $k_n = \frac{(n+1/2)\pi}{z_0+z_e}$, z_e and z_c are the length of the endcaps and the length of the compensation electrodes respectively, and z_0 is the distance along the axis from the center of the trap to the end of the compensation electrode. As Eqns. 6.1.2 and 6.1.3, and 6.1.5 and 6.1.6, are solutions to the same hypergeometric equation (Laplace equation) they are equivalent and are related by the expressions

$$C_k^{(0)} = \frac{(-1)^{k/2}}{k!} \frac{\pi^{k-1}}{2^{k-3}} \left(\frac{d}{z_0 + z_e}\right)^k \sum_{n=0}^{\infty} (2n+1)^{k-1} \frac{A_n^{(0)}}{J_0(ik_n r_0)} \tag{6.1.7}$$

where

$$A_n^{(0)} = \frac{1}{2}\left\{(-1)^n - \sin\left(k_n z_0\right) - \sin[k_n(z_0 - z_c)]\right\} \tag{6.1.8}$$

and for coefficients D_k

$$D_k = \frac{(-1)^{k/2}}{k!} \frac{\pi^{k-1}}{2^{k-3}} \left(\frac{d}{z_0 + z_e} \right)^k \sum_{n=0}^{\infty} (2n+1)^{k-1} \frac{A_n^{(c)}}{J_0(ik_n r_0)} \tag{6.1.9}$$

where

$$A_n^{(c)} = \sin(k_n z_0) - \sin[k_n(z_0 - z_c)] \tag{6.1.10}$$

Using these relationships, the properties of a cylindrical trap can be determined in terms of the trap dimensions and the voltages applied to the electrodes. Consequently, the voltages on the trap electrodes can be chosen to, for example, adjust a certain term of the electric potential. As the HITRAP trap requires a harmonic potential, the voltages on the electrodes of the prototype trap were calculated to cancel out the term C_4 ($C_4 = 0$) or, in other words, to null the quartic terms of the potential. In practice, the dimensions of the HITRAP trap electrodes were mainly determined by the superconductor magnet characteristics. The total length of the prototype HITRAP trap was influenced by the length of the magnet's field homogeneity region, reported to be in the range of 130 to 150 mm at the center of the magnet bore. In addition, the diameter of the trap prototype was influenced by the inner diameter of the magnet bore, reported and measured to be 85.5 mm. The final total length of the trap was chosen to be compatible with the magnet's specifications but also to fit inside the vacuum chamber specifically designed to fit inside the magnet's bore. Although the latter considerations fixed the total length and the diameter of the trap, the relative sizes of the electrodes were chosen to improve the performance of the trap.

Table 2: Expansion coefficients for the original cylindrical trap design (1989).

Expansion coefficients for the Gabrielse trap $r_0 = 0.6$ cm, $z_0 = 0.585$ cm, $z_c = 0.488$ cm and $z_e = 2.531$ cm		
$C_2^{(0)} = +0.544$	$D_2 = 0.000$	$C_2 = +0.544$
$C_4^{(0)} = -0.211$	$D_4 = -0.556$	$C_4 = 0.000$
$C_6^{(0)} = +0.163$	$D_6 = +0.430$	$C_6 = 0.000$
To cancel out quartic anharmonicities: $V_c = -0.3806\ V_0$		

Since the dimensions of the trap electrodes are important parameters in Eqns. 6.1.7, 6.1.8, 6.1.9 and 6.1.10, they can be chosen to impose a particular condition to the electric potential generated in the trap. An interesting case arises when the electrode sizes are chosen in such a way that term $D_2 = 0$. This action causes the quadratic term of the potential to be independent of the voltage applied to the compensation electrodes. This particular case is very useful during the operation of an ion trap because a change in the voltage on the compensation electrodes will not change the axial frequency of the trapped ions, facilitating the optimization of the trap parameters. The first trap that fulfilled the latter requirements was the trap proposed by Gabrielse in 1989. He called this trap an "orthogonal trap" and its dimensions and expansion coefficients are presented in Table 2. The Maple code used to generate the expansion coefficients is presented in the Appendix; Fig. 8.1.

Based on the design proposed by Gabrielse [15], the electrode dimensions of the HITRAP trap were selected in such a way that the trap fulfills the conditions of a harmonic and an orthogonal trap. These dimensions also fulfill the conditions determined by the magnet and the vacuum chamber. The electrode dimensions and the expansion coefficients for the HITRAP trap are presented in Table 3.

Table 3: Expansion coefficients for the HITRAP design, (2005).

Expansion coefficients for the HITRAP trap $r_0 = 10.6$ mm, $z_0 = 5.90$ mm, $z_c = 1.75$ mm and $z_e = 25.00$ mm		
$C_2^{(0)} = +0.534$	$D_2 = -0.001$	$C_2 = +0.532$
$C_4^{(0)} = -0.137$	$D_4 = -0.077$	$C_4 = 0.000$
$C_6^{(0)} = +0.137$	$D_6 = +0.039$	$C_6 = +0.067$
To cancel out quartic anharmonicities: $V_c = -1.768\ V_0$		

A sketch of the trap dimensions is presented in Fig. 6.1. As one can observe, the length of the ring electrode in the HITRAP trap was chosen to be bigger than the compensation electrodes to produce a better collection of light from the trapped ions, a feature that is different from the Gabrielse trap. According to calculations done with the expansion coefficients method, this

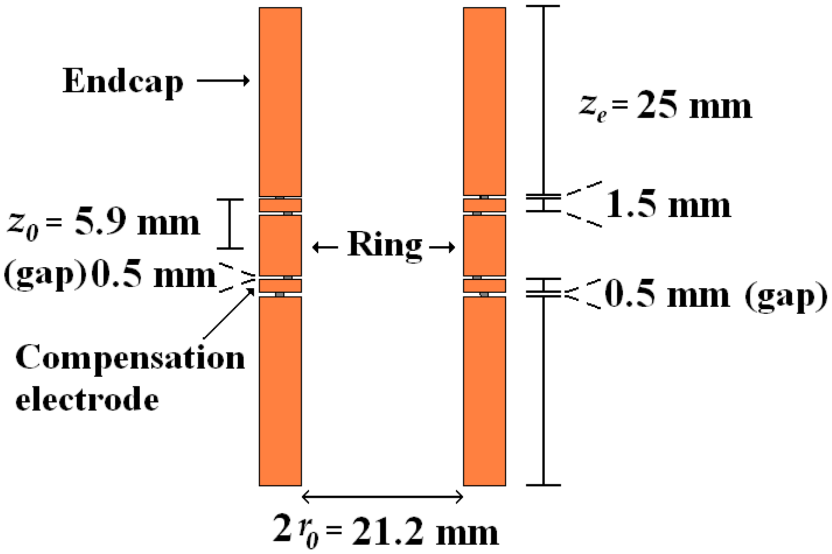

Figure 6.1: Harmonic and Orthogonal dimensions for the HITRAP trap.

modification is capable of producing a harmonic and an orthogonal potential.

In practice, the design of the HITRAP trap has some elements that can not be considered in the calculations, probably the most important one being the assumption of negligible gaps between the electrodes. In the HITRAP prototype, the gaps were reduced to the minimum practical value but were still too large to be negligible. The trap was designed to have gaps of 0.5 mm, a separation that is only three times smaller than the length of the compensation electrodes. In addition, the ring electrode of the HITRAP prototype was designed to be radially segmented in four parts for the application of the rotating wall technique to the trapped ions, a characteristic that is also not considered in the calculations. According to [15], z_e is formally defined as the length of the endcap electrode, z_0 is the distance from the centre of the trap to the endcap and z_c is the distance from the beginning of the compensation electrode to the beginning of the endcap. The dimensions of the prototype electrodes are $z_0 = 5.90$ mm, $z_c = 1.50$ mm and $z_e = 25.00$ mm, and these electrodes are separated by gaps of 0.5 mm. The values of z_0 and z_e were not modified for the calculations but 0.25 mm (half of a gap separation) were added to z_c in an effort to include the size of the gap in the calculations. To verify that a harmonic potential is generated by using these electrode dimensions and the voltages specified by the calculations, simulations were carried out in SIMION.

A SIMION project was created following the electrode voltages and the electrode dimensions obtained by the model but with 0.5 mm gaps between the electrodes. The SIMION project was progressively modified until the final design included all the electrodes, supports, the vacuum chamber, a segmented ring and an extra pair of electrodes that will be used during the injection of ions into the trap. Two views of the SIMION project are shown in Fig. 6.2.

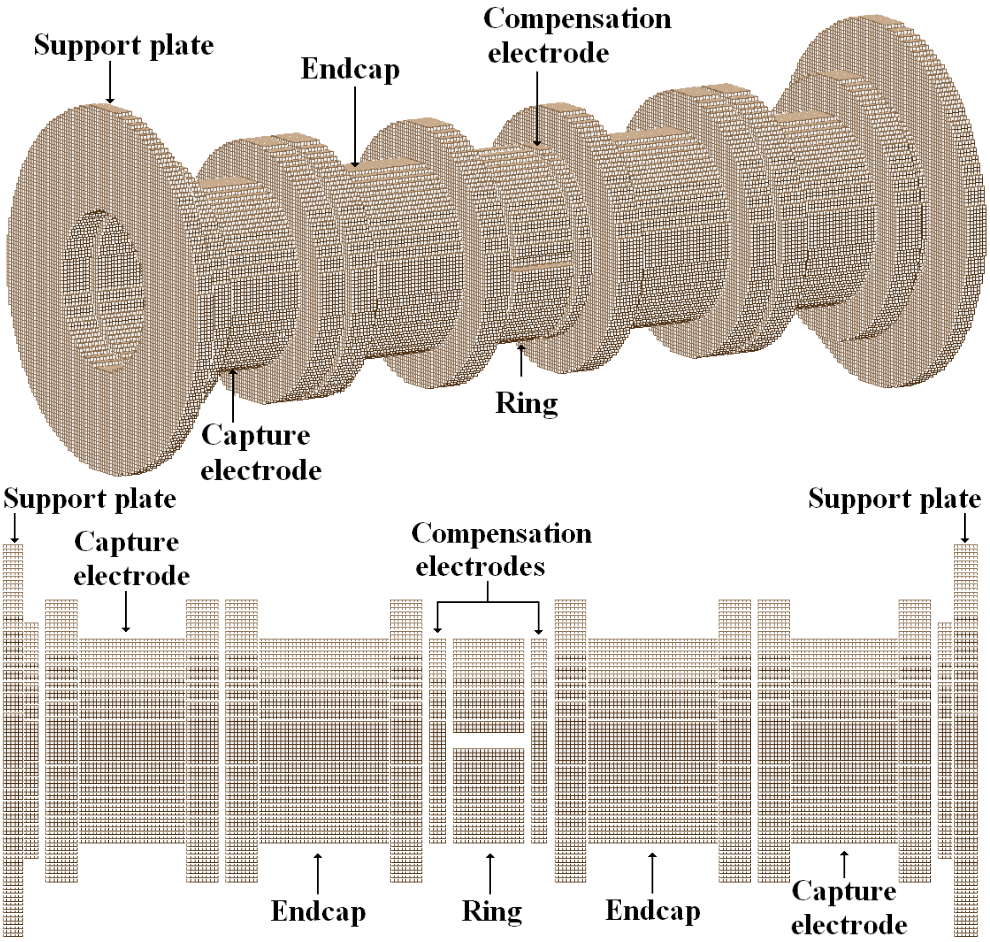

Figure 6.2: SIMION project for the HITRAP trap. The simulation corresponds to the prototype trap that is being constructed in the Ion Trapping Group at the Imperial College (2007).

Using this project, the axial potential along the entire trap length was obtained to verify the harmonicity of the electric potential in the centre of the trap. Voltages on the electrodes are in the proportion dictated by the calculations, this is $V_c/V_0 = -1.768$, with $V_0 = 1$ volt. The results from the simulations are presented in Fig. 6.3.

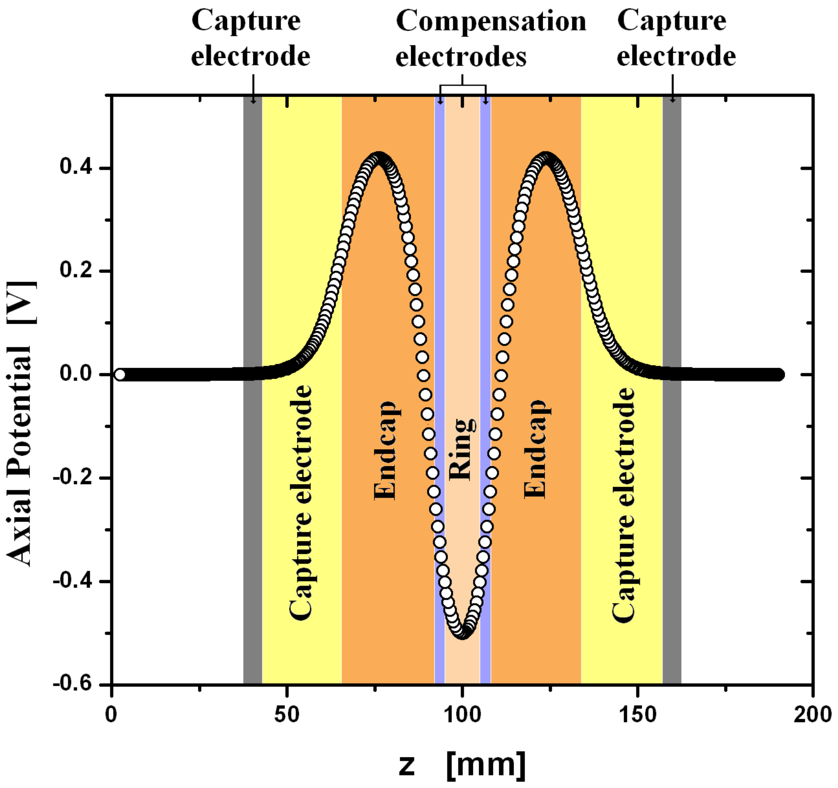

Figure 6.3: Axial potential along the trap configuration. In colours, the respective electrode position. $V_c/V_0 = -1.768$, with $V_0 = 1$ volt

To confirm a good harmonic potential at the center of the trap, the numerical data of the axial potential at the center of the trap were fitted with a sixth-order polynomial curve. The fitting only considered the data between -5 mm to 5 mm, centred at the middle of the trap. The results are presented graphically in Fig. 6.4.

The potential around the centre is given by

$$\begin{aligned}\phi(z) = -0.5 + 3.26\times10^{-3}[\mathrm{V/mm^2}]z^2 - 3.3\times10^{-5}[\mathrm{V/mm^4}]z^4 + \\ +1.71\times10^{-7}[\mathrm{V/mm^6}]z^6\end{aligned}$$

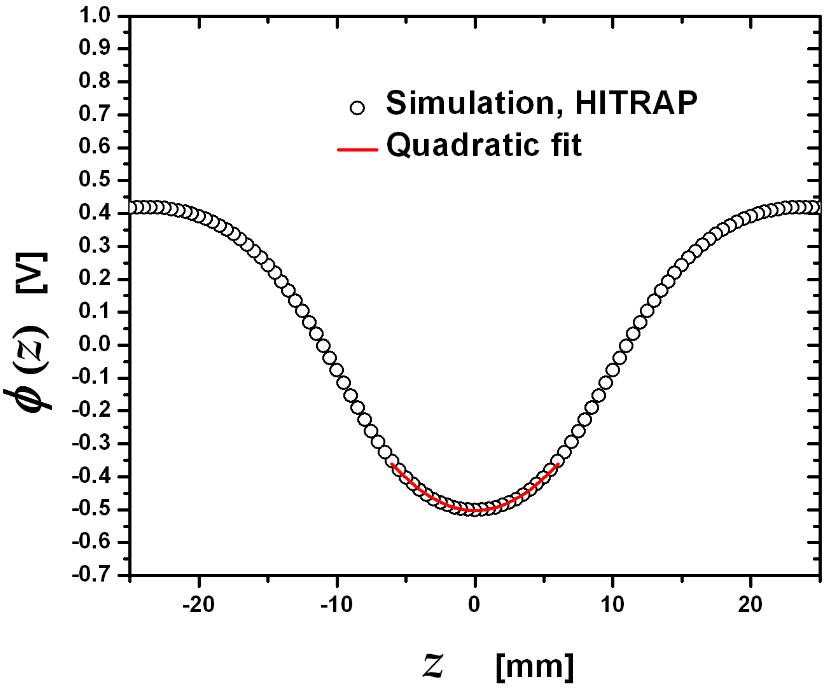

Figure 6.4: Axial potential around the centre of the trap. The red line shows a sixth-order polynomial fitting.

where it can be seen that only the harmonic and the constant terms are significant near the centre of the trap. At $z = 2$ mm the contribution of the quartic term is around 30 times smaller than the quadratic one, and at $z = 5$ mm the quartic term is around 5 times smaller than the quadratic one.

The trap electrodes and all the trap supports are currently being manufactured out of oxygen free copper. All the parts of the support must be manufactured using the same material because the whole setup will be used at temperatures ranging from room to cryogenic temperatures. The use of a single material for all the trap parts brings a perfect expansion/constraction coefficient matching, and consequently the expansion/contraction of individual components is not an issue. The mesh that forms the walls of the ring electrode is also of oxygen free copper with a mesh size of 0.2 μm. In principle, the mesh and its supports are going to be bonded by an aluminium alloy, by a soft-soldering technique, but the response of this technique to cryogenic temperatures is still unknown.

Tests, using the HITRAP trap prototype, with singly ionized species are being planned to be carried out at Imperial College in mid-2007. The HITRAP facility will be ready at the end of 2007, when the first experiments are planned to be performed. The final technical drawings of the HITRAP trap is shown in Fig. 6.5.

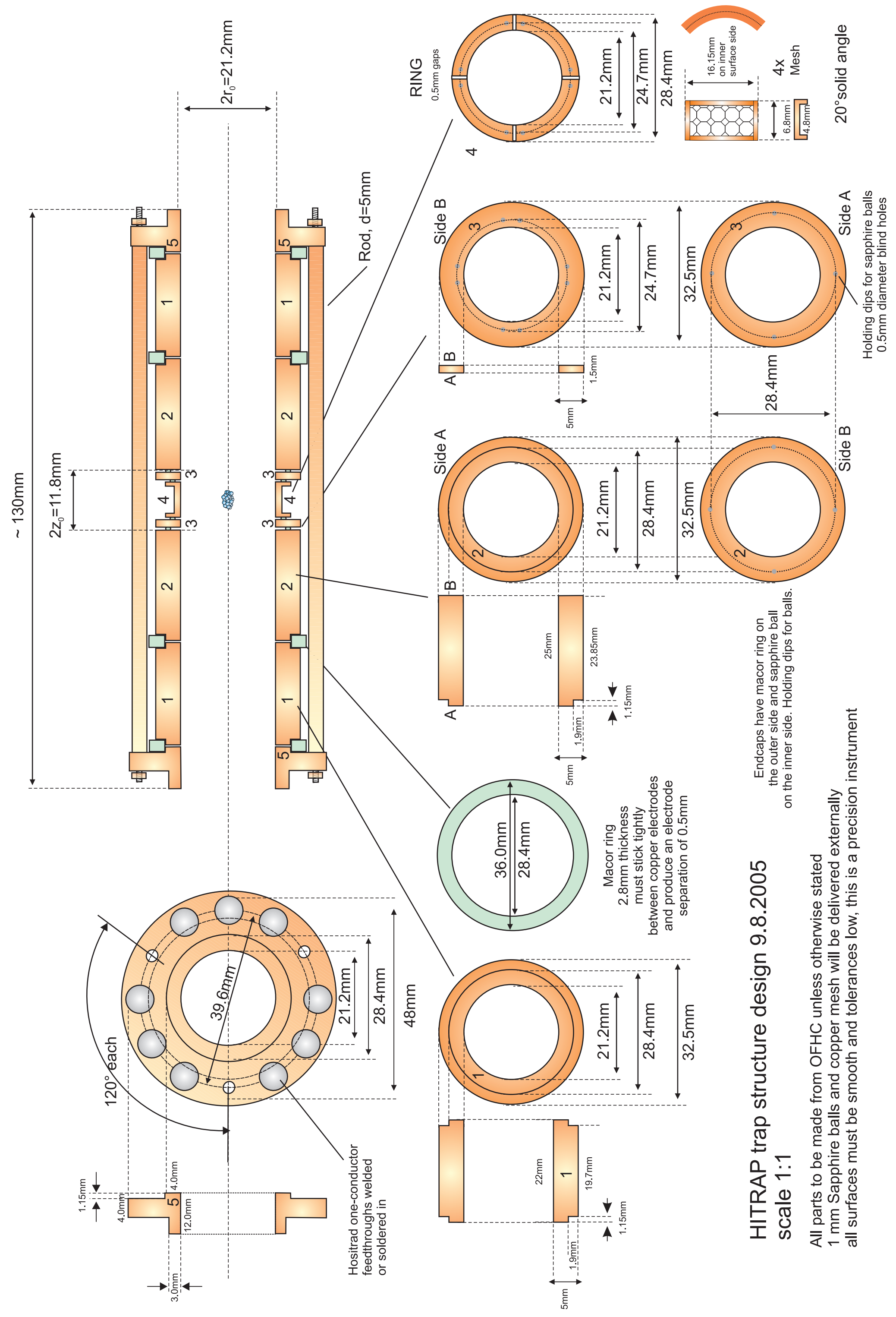

Figure 6.5: HITRAP trap technical drawings, produced by Dr. Manuel Vogel (2005) and reproduced with permission of the author.

7 Conclusions

This thesis has presented novel designs for Penning and RF traps. All these proposals were supported by calculations, simulations and, in the case of the wire Penning trap, experiments.

Wire traps, Penning or RF, present many advantages over the traditional ion trap designs. They can be used in experiments where *i*) the optical access to the trapped ions is critical, *ii*) an array of many independent traps is required, *iii*) the controlled interaction of particles is needed, *iv*) the transport of charged particles is needed.

In this thesis, particular attention was given to the six-wire Penning trap as a prototype was constructed and successfully tested. This prototype confirmed some of the advantages suggested by the proposal: it is easy to design, construct, align and operate. Experiments carried out in this prototype demonstrated that an ion trap can be created by an array of six cylindrical electrodes connected to DC power supplies and in the presence of a magnetic field. From the theoretical point of view, the design of the wire Penning trap offers a three-dimensional scalable design that is analytically described. In addition, the geometry of the trap can be miniaturized as it only consists of an array of wires. In a single array of six wire electrodes, up to four trapping points can be created; one over, one above and two between the electrodes. It was also shown that the axial position of the trapping points can be changed by modifying the voltage on the electrodes; in this way the two trapping points in the middle can be mixed into one and the outer trapping points can be pulled or pushed from the electrodes. The geometry of the wire Penning trap is also scalable, as an array of these traps can be created by increasing the number of electrodes. Some strategies for moving ions around in an array of wire traps were also discussed. Finally, a scheme to study two interacting particles in two different wire traps was presented.

Together with the wire Penning trap, this thesis also presented the novel designs of an ion guide, two RF traps and a two-plate Penning trap. The ion guide is basically an array of three wire electrodes that creates trapping conditions along the axis of the wires. This setup presents a novel approach to transport ions in a controlled way, and when combined with the six wire Penning trap it can create a scheme to shuttle ions in a scalable design.

As mentioned, this thesis also presented two novel designs for RF traps. The first design, the linear wire trap, exhibits the same properties as ordinary linear Paul traps but with a more open and simple geometry. The second design, the six wire RF trap, stands as a RF trap with open geometry and a two-dimensional scalability.

In addition to the later designs, another simple design for an ion trap was presented. This trap was called the two-plate trap as it is made of two parallel conductor plates; the upper electrode is a planar ring and the lower electrode is a disk. If the electrodes are connected to opposite voltages, a trapping point is created above the electrode structure. Consequently, this design offers a simple geometry that can be easy constructed and miniaturized. A simple scalable design of this trap was also presented in the text.

This thesis concludes with the design of a cylindrical trap for the study of highly charged ions. Although this is a traditional geometry for an ion trap, its design required specific calculations and simulations as the geometry was modified to fulfill the requirements established by the experiment. This trap is currently under construction and testing. Experiments in the HITRAP facility will begin on 2008.

The trap designs presented in this thesis have opened the possibility of performing different experiments. Currently, the wire trap prototype is being modified for optical detection experiments with singly ionized calcium atoms. Once these experiments are carried out, the prototype will be run with RF drives to demonstrate that this trap geometry can run as a Paul trap. Middle term plans include the modification of the prototype to allow the optical detection of Ca^+ in the trapping points above and below the wire electrodes. In the long term, the construction of a scalable setup with wire traps is being planned. This will allow the study of ion-ion interactions and also the transport of ions between traps. The two-plate trap also offers an attractive setup for experimentally studies. Plans to construct and test a two-plate trap are also under consideration. Finally, the construction of a miniaturized version of any of the novel designs is also being prepared.

8 Appendix

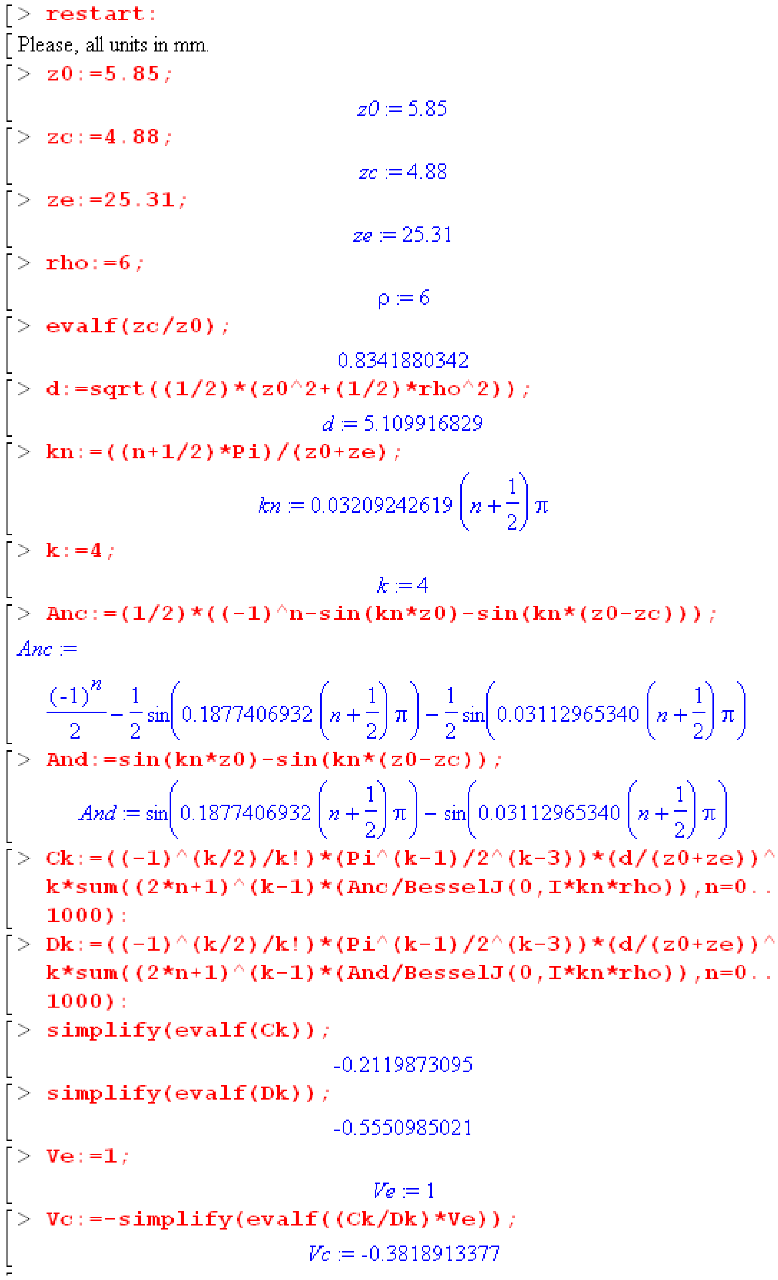

```
> restart:
```

Please, all units in mm.

```
> z0:=5.85;
```

$$z0 := 5.85$$

```
> zc:=4.88;
```

$$zc := 4.88$$

```
> ze:=25.31;
```

$$ze := 25.31$$

```
> rho:=6;
```

$$\rho := 6$$

```
> evalf(zc/z0);
```

$$0.8341880342$$

```
> d:=sqrt((1/2)*(z0^2+(1/2)*rho^2));
```

$$d := 5.109916829$$

```
> kn:=((n+1/2)*Pi)/(z0+ze);
```

$$kn := 0.03209242619\left(n+\frac{1}{2}\right)\pi$$

```
> k:=4;
```

$$k := 4$$

```
> Anc:=(1/2)*((-1)^n-sin(kn*z0)-sin(kn*(z0-zc)));
```

$$Anc :=$$

$$\frac{(-1)^n}{2}-\frac{1}{2}\sin\left(0.1877406932\left(n+\frac{1}{2}\right)\pi\right)-\frac{1}{2}\sin\left(0.03112965340\left(n+\frac{1}{2}\right)\pi\right)$$

```
> And:=sin(kn*z0)-sin(kn*(z0-zc));
```

$$And := \sin\left(0.1877406932\left(n+\frac{1}{2}\right)\pi\right)-\sin\left(0.03112965340\left(n+\frac{1}{2}\right)\pi\right)$$

```
> Ck:=((-1)^(k/2)/k!)*(Pi^(k-1)/2^(k-3))*(d/(z0+ze))^
  k*sum((2*n+1)^(k-1)*(Anc/BesselJ(0,I*kn*rho)),n=0..
  1000):
> Dk:=((-1)^(k/2)/k!)*(Pi^(k-1)/2^(k-3))*(d/(z0+ze))^
  k*sum((2*n+1)^(k-1)*(And/BesselJ(0,I*kn*rho)),n=0..
  1000):
> simplify(evalf(Ck));
```

$$-0.2119873095$$

```
> simplify(evalf(Dk));
```

$$-0.5550985021$$

```
> Ve:=1;
```

$$Ve := 1$$

```
> Vc:=-simplify(evalf((Ck/Dk)*Ve));
```

$$Vc := -0.3818913377$$

Figure 8.1: Maple9.0 worksheet, expansion coefficients for cylindrical traps.

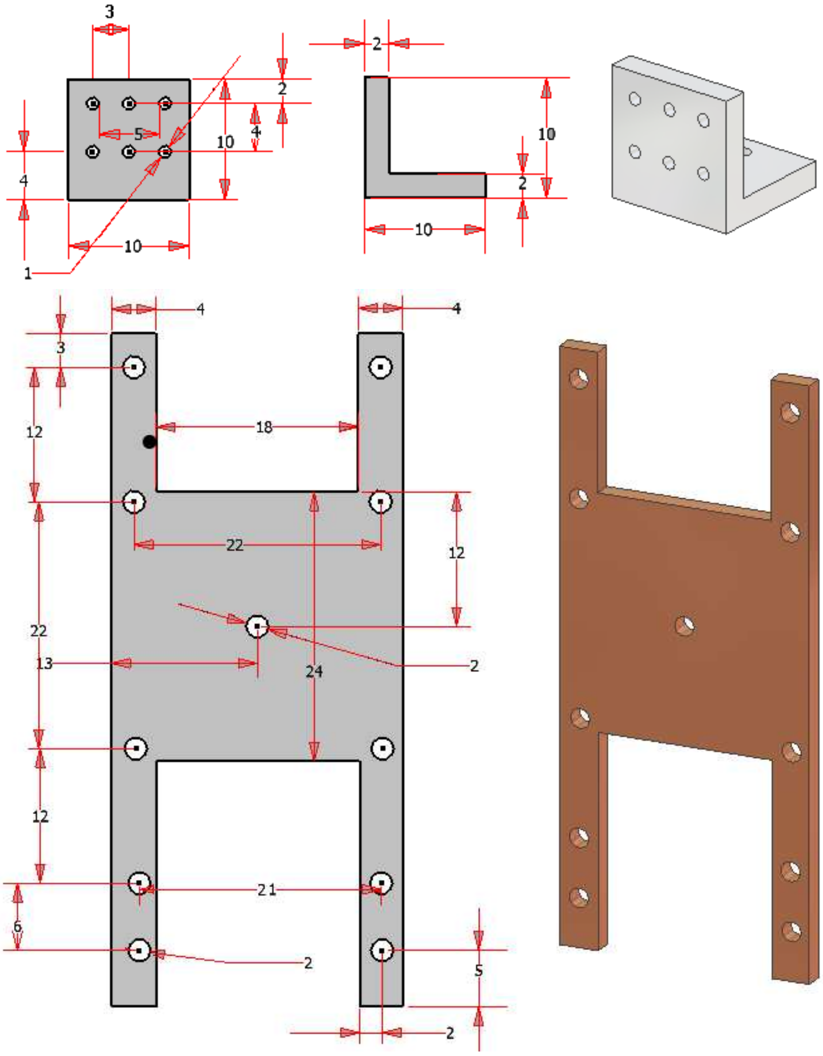

Figure 8.2: Inventor 11.0 technical drawings for the electrode mounts and the trap base. The L-shape mounts were made of Macor and the trap base was made of oxygen-free copper. All dimensions in millimeters.

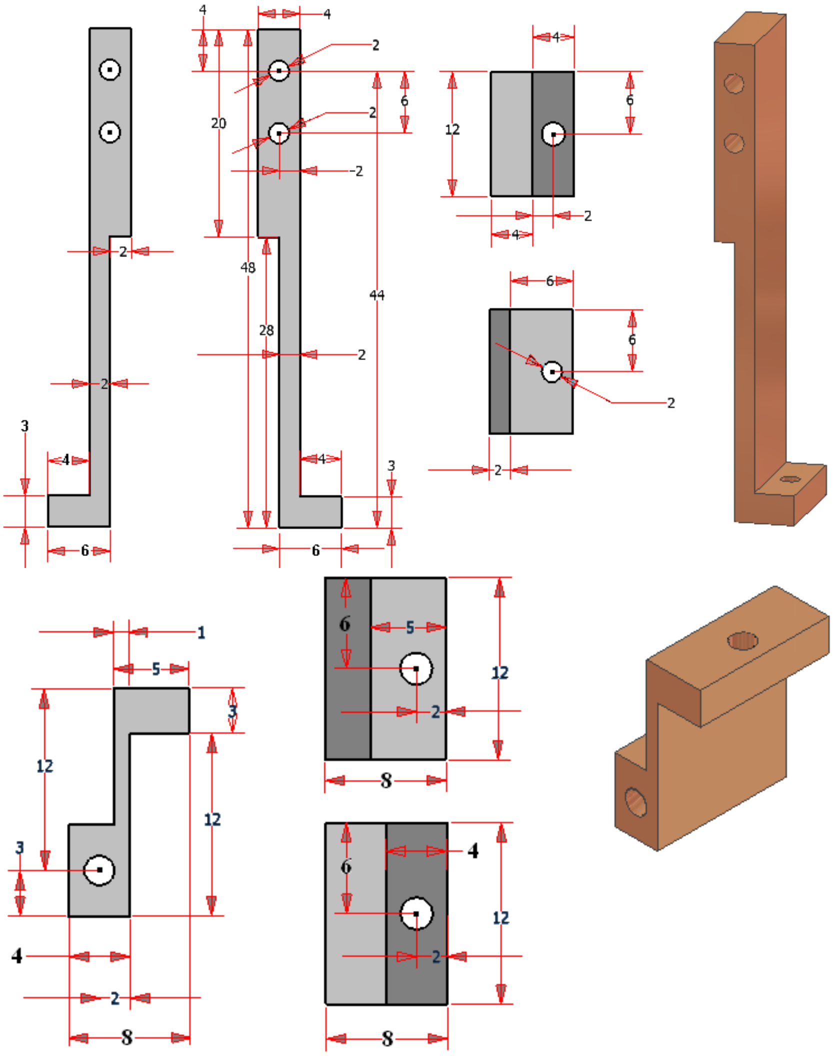

Figure 8.3: Inventor 11.0 technical drawings for the base pedestals and upper supports. These components were made of oxygen-free copper. All dimensions in millimeters.

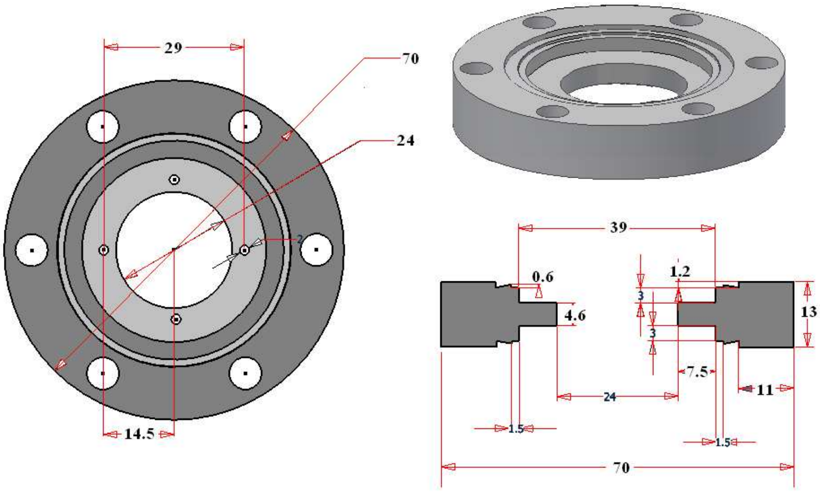

Figure 8.4: Inventor 11.0 technical drawings for the DN40 CF flange support. This component was made of stainless-steel. All dimensions in millimeters.

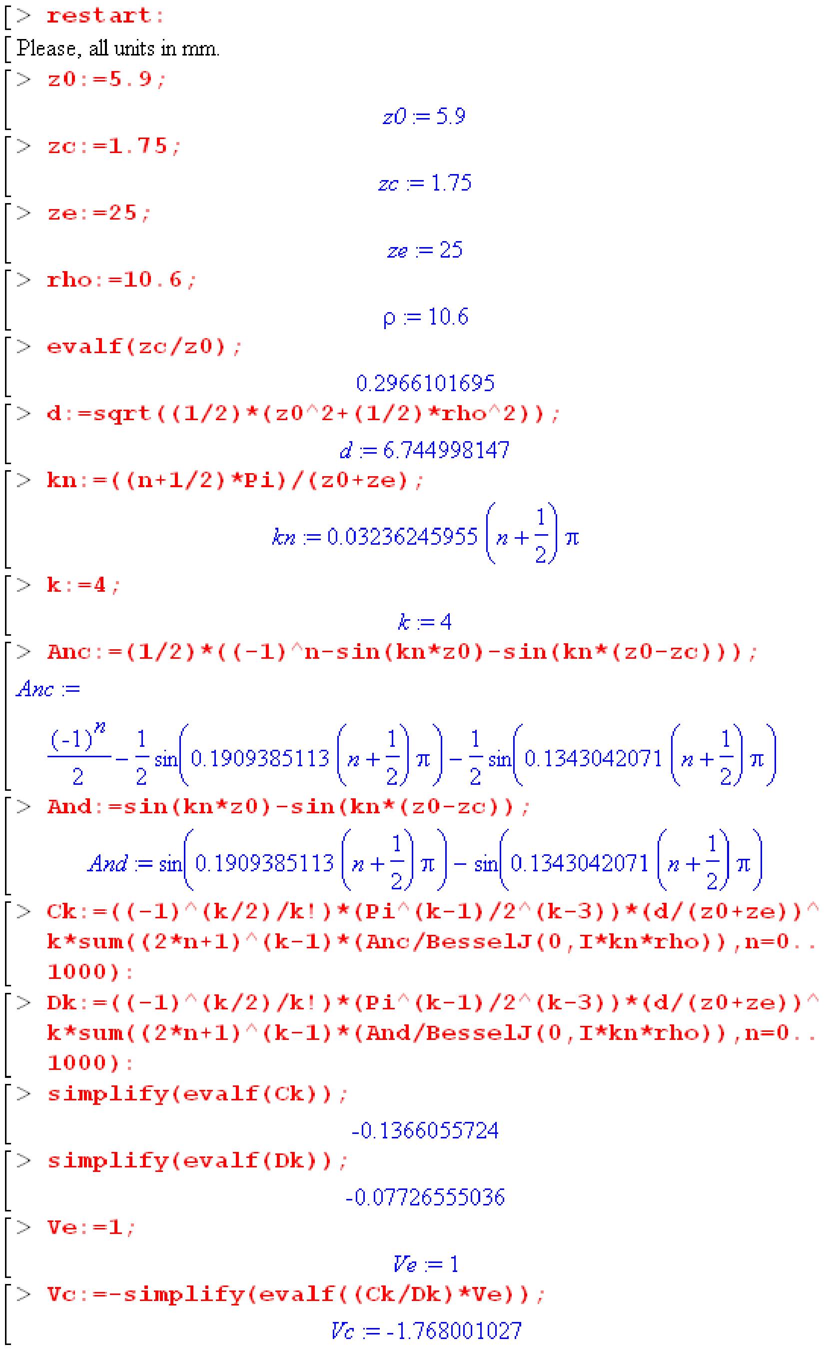

```
> restart:
```

Please, all units in mm.

```
> z0:=5.9;
```

$$z0 := 5.9$$

```
> zc:=1.75;
```

$$zc := 1.75$$

```
> ze:=25;
```

$$ze := 25$$

```
> rho:=10.6;
```

$$\rho := 10.6$$

```
> evalf(zc/z0);
```

$$0.2966101695$$

```
> d:=sqrt((1/2)*(z0^2+(1/2)*rho^2));
```

$$d := 6.744998147$$

```
> kn:=((n+1/2)*Pi)/(z0+ze);
```

$$kn := 0.03236245955 \left(n+\frac{1}{2}\right) \pi$$

```
> k:=4;
```

$$k := 4$$

```
> Anc:=(1/2)*((-1)^n-sin(kn*z0)-sin(kn*(z0-zc)));
```

$$Anc := \frac{(-1)^n}{2} - \frac{1}{2} \sin\left(0.1909385113 \left(n+\frac{1}{2}\right) \pi\right) - \frac{1}{2} \sin\left(0.1343042071 \left(n+\frac{1}{2}\right) \pi\right)$$

```
> And:=sin(kn*z0)-sin(kn*(z0-zc));
```

$$And := \sin\left(0.1909385113 \left(n+\frac{1}{2}\right) \pi\right) - \sin\left(0.1343042071 \left(n+\frac{1}{2}\right) \pi\right)$$

```
> Ck:=((-1)^(k/2)/k!)*(Pi^(k-1)/2^(k-3))*(d/(z0+ze))^
  k*sum((2*n+1)^(k-1)*(Anc/BesselJ(0,I*kn*rho)),n=0..
  1000):
> Dk:=((-1)^(k/2)/k!)*(Pi^(k-1)/2^(k-3))*(d/(z0+ze))^
  k*sum((2*n+1)^(k-1)*(And/BesselJ(0,I*kn*rho)),n=0..
  1000):
> simplify(evalf(Ck));
```

$$-0.1366055724$$

```
> simplify(evalf(Dk));
```

$$-0.07726555036$$

```
> Ve:=1;
```

$$Ve := 1$$

```
> Vc:=-simplify(evalf((Ck/Dk)*Ve));
```

$$Vc := -1.768001027$$

Figure 8.5: Maple9.0 worksheet, expansion coefficients for the HITRAP trap.

9 References

[1] D.J. Wineland and W. M. Itano, *Physics Today*, **34** (June, 1987).

[2] J.J. Bollinger, *et. al.*, *Phys. Rev. Lett.*, **54**, 1000 (1985).

[3] A.J. Scott, C.A. Holmes and G.J. Milburn, *Phys. Rev. A.*, **61**, 013401 (2000).

[4] C. Raab, *et. al.*, *Appl. Phys. B*, **67**, 683 (1998).

[5] P.K. Ghosh, *Ion Traps*, (Oxford University Press, 1995).

[6] R.C. Thompson, *Spectroscopy of Trapped ions*, (Academic Press, 1993).

[7] H.F. Powell, D.M. Segal and R.C. Thompson, *Phys. Rev. Lett.*, **89**, 093003-1 (2002).

[8] H.F. Powell, *et. al.*, *J. Phys. B.*, **35** 205 (2002).

[9] J.E. Sträng, *Acad. Roy. Belg. Bull. Cl. Sci*, in press (2006).

[10] R.C. Thompson, *Adv. At. Mol. Opt. Phys.*, **31**, 63 (1993).

[11] R.C. Thompson, *Spectroscopy and quantum optics with trapped ions, (24th International Nathiagali Summer College on Physics and Contemporary Needs, Pakistan)*, (July 1999).

[12] S.L. Ross, *Introduction to Ordinary Differential Equations* , (Fourth Edition, John Wiley and Sons Inc., 1989).

[13] H.C. Nägerl, *et. al.*, *Fortsch. Phys.*, **48**, 623 (2000).

[14] H.A. Prestage, G.J. Dick, and L. Maleki, *IEEE Trans. Instrum. Maeas.*, **40**, 132 (1991).

[15] G. Gabrielse, L. Haarsma and S.L. Rolston, *Int. J. Mass Spec. and Ion Proc.*, **88**, 319 (1989).

[16] G. Gabrielse and F. Colin MacKintosh, *Int. J. Mass Spec. and Ion Proc.*, **57**, 1 (1984).

[17] M.N. Benilan and C. Audoin, *Int. J. Mass Spectrom. Ion Phys.*, **11**, 421 (1973).

[18] J. Tan, C.H. Tseng and G. Gabrielse, *Bull. Am. Phys. Soc.*, **33**, 931 (1988).

[19] S. Stahl, *et.al. Eur. Phys. J. D.*, **32**, 139 (2005).

[20] F. Galve1 , P. Fernández and G. Werth, *Eur. Phys. J. D*, **40** ,201 (2006).

[21] D. Stick *et. al. Nature Physics*, **2**, 36 (2006).

[22] personal communication Dr. W.K. Hensinger, University of Sussex, United Kingdom (2006).

[23] D.J. Wineland, R.E. Drullinger and F.L. Walls, *Phys. Rev. Lett.*, **40**, 1320 (1978).

[24] W. Neuhauser, M. Hohenstatt, P. Toschek and H. Dehmelt, *Phys. Rev. Lett.*, **41**, 233 (1978).

[25] D. J. Larson *et.al. Phys. Rev. Lett.*, **57**, 70 (1986).

[26] T.M. O'Neil, *Phys. Fluids*, **24**, 1447 (1981).

[27] M. H. Holzscheiter *Physica Scripta*, **T22**, 73 (1988).

[28] T. Beir, *et. al.*, *HITRAP Technical Design report, European RTD network* (GSI Darmstadt, October 2003).

[29] W. Quint, *Hyperfine Interactions*, **132**, 453 (2001).

[30] D.F.A.Winters, *et.al.*, *Nuc. Inst. Meth. Phys. Res.B*, **235**, 201 (2005).

[31] S. Stahl, *Modern Non-Destructive Electronic Detection Techniques*, (Nipnet Conference, Mainz 2005).

[32] M. Diederich, *et. al.*, *Hyperfine Interactions*, **115**, 185 (1998).

[33] D.F.A. Winters, M. Vogel, D.M. Segal, and R.C. Thompson, *J. Phys. B: At. Mol. Opt. Phys.*, **39**, 3131-3143 (2006).

[34] A. Kellerbauer *et.al.*, *Precision Mass Measurements of Argon Isotopes*, (European Organization for Nuclear Research CERN, 2000).

[35] M. Nielsen and I. Chuang, *Quantum Computation and Quantum Information* (Cambridge University Press, First Edition, 2000).

[36] J.I. Cirac and P. Zoller, *Phys. Rev. Lett.*, **74**, 4091 (1995).

[37] J.J. Bollinger, *et.al.*, *IEEE Trans. Instrum. Meas*, **40**, 126 (1991).

[38] F. Schimidt-Kaler, *et. al.*, *Nature*, **422**, 408 (2003).

[39] G. Ciaramicoli, I. Marzoli and P. Tombesi, *Phys. Rev. Lett.*, **91**, 017901-1 (2003).

[40] C. Langer, *et.al.*, *Phys. Rev. Lett.*, **95**, 060502 (2005).

[41] J.R. Castrejón-Pita and R.C. Thompson, *Phys. Rev. A*, **72**, 013405 (2005).

[42] J.D. Jackson, *Classical Electrodynamics* (Third edition, Wiley Press, 1998).

[43] G.Z.K. Horvath, *Dynamics and Laser Cooling of Ions Stored in a Penning Trap* PhD Thesis, Blackett Laboratory, Imperial College London (1995).

[44] J.R. Castrejón-Pita, *et.al. Journal of Modern Optics*, in press (2006).

[45] Oxford Instruments Limited, *Instruction Manual N100* Oxford OX2 0DX, United Kingdom (no date specified).

[46] P. Burnett, *UROP project*, Blackett Laboratory, Imperial College London (1997).

[47] I. Langmuir, *Phys. Rev.*, **22**, 357 (1923).

[48] D. Kielpinski, C. Monroe and D.J. Wineland, *Nature*, **417** 709 (2002).

[49] D.H.E. Dubin and T.M. O'Neil, *Rev. Mod. Phys.*, **71**, 87 (1999).

[50] X.P. Huang, *et.al.*, *Phys. Rev. Lett.*, **78** , 875 (1997).